Influence of Particle Shape on the Global Mechanical Response of Granular Packings: Micromechanical Investigation of the Critical State in Soil Mechanics

Von der Fakultät für Bau– und Umweltingenieurwissenschaften
der Universität Stuttgart
zur Erlangung der Würde eines Doktors der Ingenieurwissenschaften (Dr.-Ing.)
genehmigte Abhandlung,

vorgelegt von

ANDRÉS ALFONSO PEÑA OLARTE

aus Manizales, Kolumbien

Hauptberichter:	Prof. Dr.-Ing. Pieter A. Vermeer
Mitberichter:	Prof. Dr. rer. nat. Hans J. Herrmann

Tag der mündlichen Prüfung: 6. Februar 2008

Institut für Geotechnik der Universität Stuttgart

2008

Mitteilung 59
des Instituts für Geotechnik
Universität Stuttgart, Germany, 2008

Editor:
Prof. Dr.-Ing. P. A. Vermeer

Institut für Geotechnik
Universität Stuttgart
Pfaffenwaldring 35
70569 Stuttgart

Keywords: Discrete element method, critical state, particle shape anisotropy

Printed by e.kurz + co, Stuttgart, Germany, 2008

ISBN 978-3-921837-59-7
(D93 - Dissertation, Universität Stuttgart)

Preface

In 1936 Casagrande subjected sand samples to continuous shearing and found that all samples would asymptotically reach a so-called critical porosity independent of the initial porosity of the samples. Since then this finding played a significant role in understanding soil behaviour and in constitutive modelling of large soil deformation. Large deformations also occur in shear bands so that the concept of a critical state is also relevant of studies on shear banding. In fact, large deformations are always connected to shear banding and it is difficult to measure average porosities of shear bands. For this reason, both experimental data and the concept of critical state have been questioned. It would seem that this question can only be answered by micro-mechanical investigations as reported in the manuscript under review. Originally the Discrete Element Method was applied to circular discs, but it is now applied to assemblies of highly anisotropical polygons with aspect ratios up to 2.3. For such assemblies one defines not only the fabric tensor for contact points, but also the inertia tensor for the direction of the particles.

Chapter 4 is for sure the scientific kernel of this thesis, as it concentrates on the influence of anisotropic particle shapes on the global mechanical behaviour of granular material. For anisotropic particles, it is shown that a critical state cannot be reached in biaxial tests with strains up to 40 %. In order to allow for larger deformations numerical simulations are carried out for a simple shear test. In these simulations a critical void ratio is obtained for relatively low shear strains independent of the original orientations of the anisotropic particles.

An interesting finding concerns the principal stress direction. Independent of the particle shapes a principal stress direction of about $45°$ is found at critical state, which implies full coaxiality with the applied strain rate.

Finally solid proof on the existence of a critical state in granular material is given, even for highly anisotropic particles. On top of that numerical procedures within the Discrete Element Method are critically reviewed and significantly improved.

Stuttgart, 6th of June 2008
Prof. Dr.-Ing. P. A. Vermeer

Acknowledgments

First, I want to thank Prof. Dr. rer. nat. Hans J. Herrmann who gave me the opportunity to work on my thesis at the Institute of Computational Physics (ICP), and offered me continuous encouragement during this study.

Next, I am indebted to Prof. Dr-Ing. P. A. Vermeer who accepted to act as a main reviewer of this thesis.

I want to express my deepest gratitude to those people who contributed with many valuable ideas and stimulation, specially to A. Lizcano, F. Alonso-Marroquin, R. Garcia-Rojo, S. McNamara, S. Luding, F. Kun, P. Lind (muito obrigado), B. Biswal for the critical reading of this work, and other people whose names might escape my memory at this moment.

I am also grateful to all members of the ICP, Stuttgart, who supported this work by an excellent working atmosphere, to F. Raischel, F. Doster, J. Harting, M. Hecht, O. Duran, E. Parteli, F. Huber, D. Maionchi, D. Ciprian, C. Kunert, Wandana, M. Parsons, H. Patzelt and many others.

I acknowledge the support of this work by the German-Israeli Foundation and by the *Deutsche Forschungsgemeinschaft* under the project *Micromechanische Untersuchung des granulares Ratchetings*, HE2732781.

Finalmente, un gran agradecimiento a mis padres y hermano, quienes siempre me han acompañado a pesar de la distancia que nos separa. Gracias por todo a Paula y amigos.

Andrés Alfonso Peña Olarte
Stuttgart, May 2008

Contents

Abstract

Granular soils exhibit under loading a complex macro-mechanical behavior, which is a result of the discrete character of the media. This macro-mechanical response depends on the grains themselves, on the evolution of the granular structure and on phenomena occurring at the grain scale. This global response also involves the existence of the so-called asymptotic stress-strain states, which are independent of the initial state of the material. Different methods have been developed in order to predict and understand soil behavior. One of the most common approaches is the Finite Element Method (FEM), which requires as input a constitutive relation between stress and strain. However, one of the fundamental drawbacks with these relations is that they involve parameters that either lack of physical meaning or might be very difficult to calibrate with experimental data [1].

Numerical simulations using the discrete element method (DEM) have become a promising tool in the study of granular materials [2, 3]. In DEM the mechanical response of the media is obtained by modeling the interactions between the individual particles as a dynamic process and by using simple mechanical laws in these interactions. The DEM permits to study and understand phenomena occurring at the grain scale level and thus allows one to study and understand the related global response of the media. Furthermore, it enables to take into account other properties such as particle shape, size distribution, cohesion, etc.

In this thesis we use the DEM to investigate two central problems. First, the problem concerning the existence and uniqueness of the critical state in shear granular packing and, second, the influence of particle shape anisotropy on their macro-mechanical response. We start with a description of the main features of our two-dimensional polygonal DEM model. The existence of the critical state on granular packing and the role of the deformation patterns on the strain accumulation is then studied by means of numerical simulations of biaxial test. Subsequently, the influence of anisotropic particle shape on the overall mechanical response is investigated both through biaxial and periodic shear cell numerical experiments. Additionally, we study the dependency of the mechanical behavior on the evolution of inherent anisotropy regarding contact and anisotropic particle orientations. For the particular case of very slow shear processes, e.g., fault zones, we also use isotropic and anisotropic polygonal particles to represent the material within the shear zone. Here we find that the emergence of discrete avalanches with size spanning several orders of magnitude is a characteristic feature of the dynamical response of the system. Finally, we uncover a numerical problem in the DEM related with the calculation of the tangential force and propose a new approach to improve its numerical accuracy. The results presented in this thesis provide better comprehension of the role of particle shape on the macro and micro-mechanical response of granular materials, and highlight the need of its proper characterization.

Zusammenfassung

Das Gebiet der Bodenmechanik beschäftigt sich mit der Klassifizierung, den Eigenschaften und der Vorhersage des mechanischen Verhaltens von Bodenkörpern. Solche Bodenkörper werden in der Geotechnik üblicherweise in kohäsive oder granulare Böden unterteilt. Während kohäsive Böden im Allgemeinen aus Partikeln bestehen, die durch lehmartige Mineralien verbunden sind, sind granulare Böden aus losen Teilchen aufgebaut, zwischen denen nur schwache Wechselwirkungen bestehen [4]. Wir werden uns im Folgenden mit dieser zweiten Bodenart beschäftigen.

Granulare Böden weisen unter Belastung ein komplexes mechanisches Verhalten auf. Dieses makromechanische Ansprechverhalten resultiert aus dem diskreten Charakter dieser Stoffe und hängt von den Körnern selbst, der Entwicklung der granularen Struktur sowie einigen Phänomenen auf der Kornskala ab, wie etwa Rollen und Gleiten. Diese globale Systemantwort beinhaltet auch die Existenz der so genannten asymptotischen Spannungs-Dehnungs-Zustände, welche vom Anfangszustand des Materials unabhängig sind [5, 6].

Einer dieser asymptotischen Zustände, der in der Bodenmechanik betrachtet wird, ist der so genannte kritische Zustand. Das Verständnis des kritischen Zustandes stellt eine beträchtliche Herausforderung dar, da er eine zentrale Rolle in der konstitutiven Modellierung einnimmt. So wird er zum Beispiel zur Definition der Versagenskriterien und des Verhaltens vieler konstitutiver Modelle nach dem Versagen angewandt [6–11].

Die erste Beschreibung des kritischen Zustandes geht auf die Arbeit von Casagrande im Jahr 1936 zurück [12]. Er führte Scherversuche an Sandproben durch und bemerkte, dass das Spannungs-Dehnungs-Verhalten von Sand unter groṡen Scherdeformationen einen Grenzzustand erreicht, d.h. ein kritisches Volumen oder eine *kritische Porenzahl*. Dieser Grenzzustand erwies sich als unabhängig von der Anfangsdichte der Probe. Auṡerdem deformierte die granulare Probe im kritischen Zustand ohne weitere Volumen- oder Spannungsänderung, Dehnung und Spannung nahmen somit einen asymptotischen Wert an. Die kritische Porenzahl hängt lediglich vom Druck ab, daher kann eine so genannte kritische Zustandslinie definiert werden, die die kritische Porenzahl und das zugehörige kritische Spannungsverhältnis in Beziehung setzt. In den 1960er-Jahren wurde die Beschreibung des nichtlinearen Verhaltens von Böden mit der Einführung des triaxialen Tests durch Bishop [13] verbessert. Dies erleichterte die Entwicklung von elasto-plastischen Bodenmodellen, wie etwa dem Cam-Clay-Modell [14], und die Etablierung der kritischen Zustandstheorie [6]. Von experimenteller Seite wurde die Existenz und Eindeutigkeit des kritischen Zustandes unabhängig voneinander durch Castro et al [15] im Jahre 1975 und durch Verdugo et al. [16] im Jahre 1996 bestätigt. Dennoch vertreten einige Arbeitsgruppen den Standpunkt, dass ein solcher Zustand von der Konsolidierungsgeschichte des Sandes abhängt [17], und zweifeln seine Eindeutigkeit

an [18].

Ein weiterer zentraler Punkt in der Bodenmechanik ist der Einfluss der Teilchenform auf das mechanische Verhalten granularer Böden. Die Teilchenform hat sich insbesondere für Sand- und Kiesböden als eine wichtige Eigenschaft herausgestellt. Sie beeinflusst die Festigkeit unter schwacher Belastung, die Komprimierbarkeit, Festigkeitsparameter und die Anisotropie [19–21].

Während die Korngröße und deren Verteilung als wichtige Faktoren für das mechanische Verhalten von Böden anerkannt sind [4, 22, 23], wurde die Rolle der anisotropen Teilchenform bisher nicht charakterisiert. Weiterhin muss der Zusammenhang zwischen anisotroper Teilchenform und Anisotropie studiert werden, da die Anisotropie die Deformierbarkeit, Festigkeit und Permeabilität beeinflusst [21].

In dieser Arbeit werden zwei zentrale Probleme behandelt, die eng miteinander verbunden sind. Einerseits betrachten wir das Problem der Existenz und Eindeutigkeit des kritischen Zustandes. Andererseits studieren wir den Einfluss der Teilchenformanisotropie auf die makromechanische Reaktion einer gescherten granularen Packung. Hierbei verwenden wir Diskrete-Elemente-Modelle (DEM) granularer Böden, wobei die globale Reaktion stark vom diskreten Charakter des Mediums abhängt. Die DEM erlaubt es uns Phänomene zu verstehen, die auf der Skala der einzelnen Teilchen entstehen. Dadurch ist ein umfangreiches Verständnis der zugehörigen globalen Reaktionen des Mediums möglich.

In der Regel verwenden diskrete Modelle Scheiben [2, 26–28] oder Kugeln [3, 29, 30]. In unserem Fall werden die einzelnen Körner jedoch durch zufällig generierte konvexe Polygone repräsentiert, so dass wir den Einfluss der Teilchenform studieren können. Mit Hilfe von Polygonen können die zwei wesentlichen Skalen der Ungleichmäßigkeit der Teilchenform, die auf der Größenordnung des Teilchendurchmessers existieren, re-

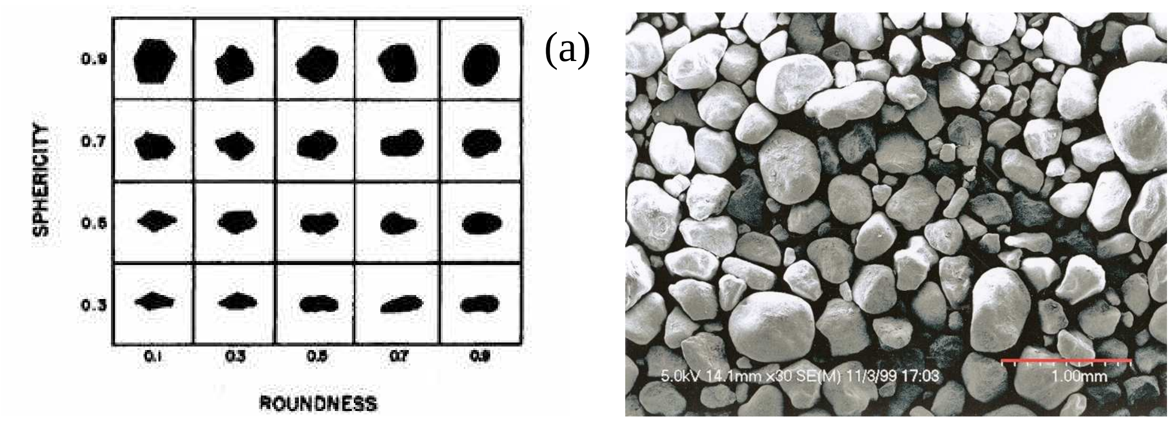

Figure 0.1: Charakteristische Teilchenformen von natürlichem Material: (a) "Sphericity" und "roundness" Diagramm, wie es zur Klassifizierung der Teilchenform verwendet wird [24]. (b) Natürlicher Quarzsand aus vier Metern Tiefe (Hwange-Nationalpark, Zimbabwe) [25].

produziert werden: die “Spherizität” (Formanisotropie) und die “Kantigkeit” (siehe Abb. 0.1).

Daher erlaubt unser Partikelmodell nicht nur die Darstellung der Haupteigenschaften einer granularen Packung, wie bspw. Elastizität, strukturelle Anisotropie, Reibung, “stick-slip”, sondern behandelt ebenfalls den wichtigen geometrischen Einfluss der Teilchenform und erlaubt so eine realistischere Modellierung von Böden.

Diese Arbeit ist wie folgt aufgebaut: In Kapitel 2 führen wir die Hauptmerkmale unseres zweidimensionalen DEM Modells für Polygone ein. Das Verfahren zur Generierung anisotropischer Polygone und Kriterien zur Wahl des Integrationsschritts für die numerische Simulation werden beschrieben.

In Kapitel 3 führen wir Simulationen von biaxialen Tests durch, um die Existenz des kritischen Zustandes und die Verformungsstrukturen der Polygonpackung unter monotoner Belastung zu studieren. Charakteristisch für die Verformung in granularen Materialien sind die Drehung und das Rollen von Teilchen [31–33], das Abrutschen an Kontakten [34, 35], sowie die Bildung von *Scherb"andern* [26, 36, 37]. Wir betrachten kleine [38] und große Scherverformungen [39]. Für kleine Verformungen studieren wir anfängliche Lokalisierungen der Belastung und/oder die Bildung von Scherbändern, sowie die zugehörigen Mikrovorgänge. Wir finden einen direkten Zusammenhang zwischen Belastung und der Anzahl rutschender Kontakte und Teilchenrotationen. Für große Verformungen studieren wir die Entwicklung des kritischen Zustandes. Wir zeigen mit Hilfe von numerischen Simulationen, dass die granularen Medien einen Grenzzustand erreichen, in dem eine kritische Menge von Leerräumen existiert und in dem bei Verformungen Volumen und Deviatorspannung konstant sind. Die Existenz und Eindeutigkeit des kritischen Zustandes ist in Abb. 0.2 für unterschiedliche Anfangsdichten und Belastungszustände dargestellt.

Im kritischen Zustand ist die dynamische Systemantwort von Spannungsfluktuationen geprägt, die aufgrund von Reibungsinstabilitäten auftreten. Die Spannungsfluktuationen, die mit Kraftketten in Verbindung gebracht werden können, sorgen dafür, dass die Gleitbedingung an den Kontakten nicht mehr erfüllt ist, und bringen das System temporär in einen stabilen Zustand. Ein ähnliches Verhalten wurde in Experimenten mit Glaskugeln beobachtet, sowohl unter Scherung [40] als auch bei uniaxialer Kompression [41]. Die durch abwechselndes Einrasten und Gleiten geprägte Bewegung in granularen Packungen ist insbesondere aufgrund der Analogie zur Erdbebendynamik interessant [42, 43].

Ferner untersuchen wir die Abhängigkeit der Systemantwort des granularen Mediums von der zwischen den Partikeln wirkenden Reibungskraft. Für verschwindende Reibungskoeffizienten zwischen den Teilchen zeigt das System einen kleinen, aber bedeutsamen Scherwiderstand. Wir können daher sagen, dass die Reibung zwischen den Partikeln nicht der einzige Ursprung des makroskopischen Reibungsverhaltens granularer Materialien darstellt. Diese Erkenntnis deckt sich mit der Vorstellung von nichtlokalem Verhalten granularer Packungen, wobei das makroskopische mechanische Verhalten nicht nur auf Phänomene zurückgeht, die auf der Skala der Kontakte auftreten, sondern auch auf die Anordnung auf der mesoskopischen Skala, wie zum Beispiel Strukturentwicklung [44] und Kraftketten [45–47].

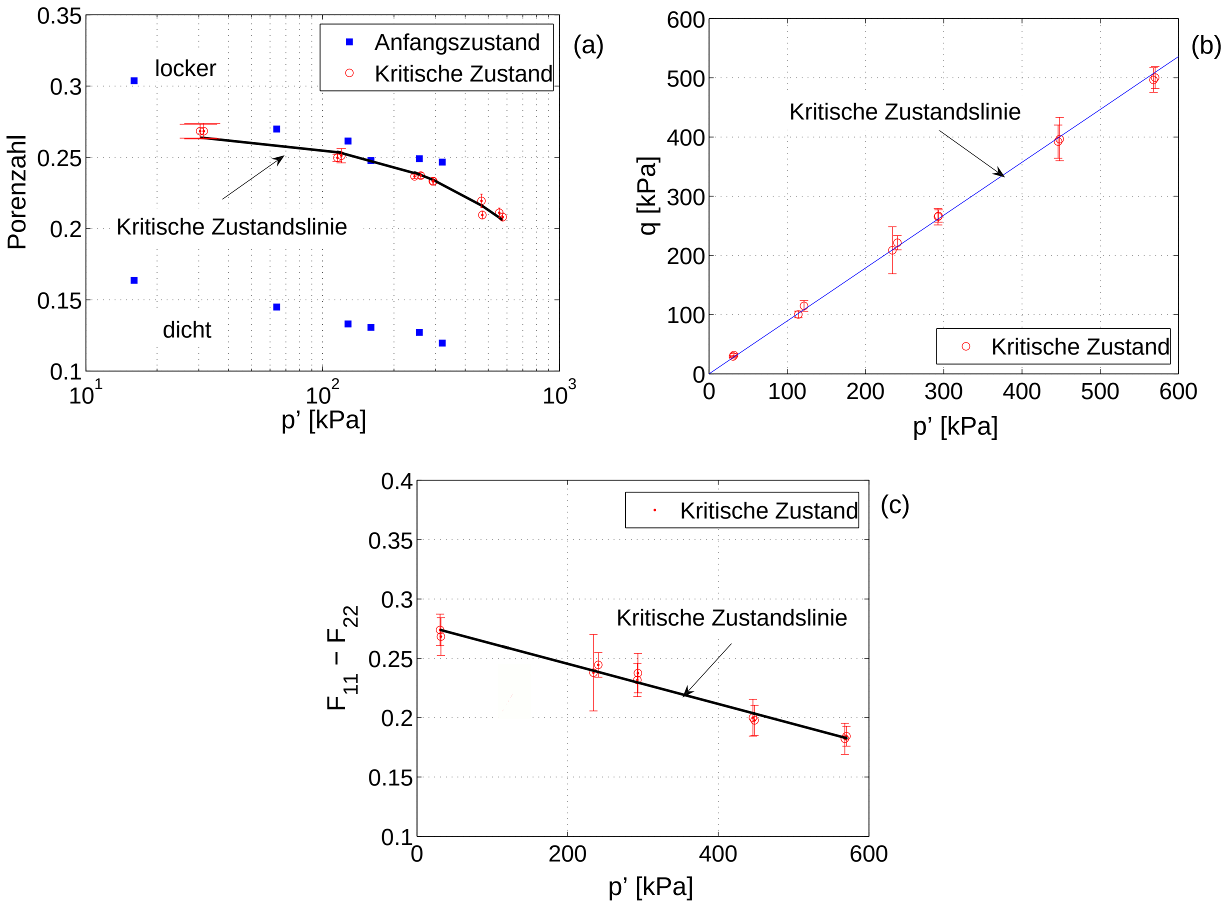

Figure 0.2: Kritische Zustandslinie in der Kompressionsebene: Porenzahl - Durchschnittsbelastung p', (b) Belastungsebene: Deviatorspannung q - Durchschnittsbelastung p' und (c) $(F_{11} - F_{22})$ - Durchschnittsbelastung p'. Systemparameter: $N = 900$ Teilchen, Reibungskoeffizient $\mu = 0.5$. Die Quadrate in (a) verdeutlichen den Anfangszustand der Proben. In (a), (b) und (c) sind die Werte im stationären Zustand durch Kreise gegeben, und die Fehlerbalken entsprechen der Standardabweichung der analysierten Daten.

In Kapitel 4 simulieren wir das mechanische Verhalten von anisotropen Teilchen in einer biaxialen Kammer und in einer periodischen Scherzelle. Wir konzentrieren uns auf den Einfluss der Partikelformanisotropie auf die mechanische Systemantwort. Wir untersuchen die Abhängigkeit des mechanischen Verhaltens von der Entwicklung inhaerenter Anisotropie in Bezug auf die Orientierung von Kontakten und von anisotropen Partikeln. In biaxialen Kompressionsversuchen wird der kritische Zustand nicht erreicht, weil auf der mikromechanischen Ebene Struktur- und Partikelorientierungen nicht zu einem konstanten Wert konvergieren. In der periodischen Scherzelle zeigen die Resultate auf der makroskopischen Ebene, dass für Proben mit anisotropen Teilchen sowohl

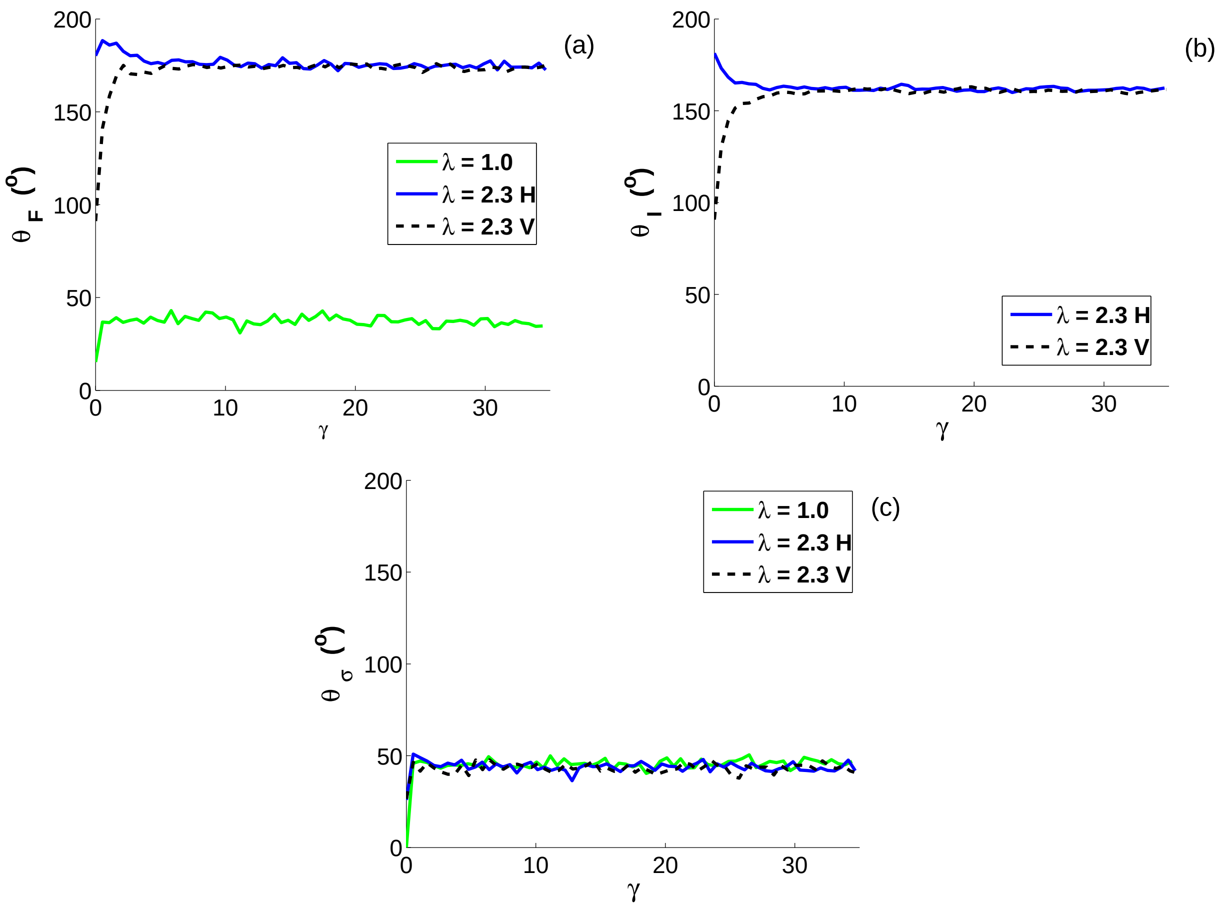

Figure 0.3: Entwicklung der Hauptrichtung von Struktur- (a), Trägheits- (b) und Spannungstensor (c) für isotrope Teilchen (λ = 1.0) und anisotrope Teilchen (λ = 2.3), die ursprünglich in horizontaler (H) und vertikaler (V) Richtung orientiert sind.

für die Scherkraft als auch für die Porenzahl bei großen Scherdeformationen unabhängig von der Anfangsorientierung der Teilchen derselbe kritische Wert erreicht wird [48]. Dieser stationäre Zustand ähnelt dem sogenannten kritischen Zustand in der Bodenmechanik. Auf den in den Kapiteln 3 und 4, vorgestellten Resultaten unserer numerischen Simulationen aufbauend wird die Eindeutigkeit des kritischen Zustands in der Bodenmechanik verifiziert, und er stellt sich als unabhängig von der gewählten Anfangsbedingung der Spannungsverteilung und Partikelformcharakteristik heraus. Auf mikromechanischer Ebene erreichen die Komponenten des Spannungstensors, des Strukturtensors und des Trägheitstensors der Teilchen ebenfalls denselben stationären Zustand. Im Fall isotroper Teilchen ist die Orientierung der Struktur abhängig von der Hauptrichtung des Spannungstensors, während für anisotrope Teilchen die Strukturorientierung durch die Partikelorientierung bestimmt wird, wie es in Abb. 0.3 dargestellt ist.

Bezüglich Deformationslokalisierung und Teilchenrotation haben wir beobachtet, dass die Breite der Scherzone und die akkumulierte Rotation für isotrope Teilchen größer ist als für anisotrope. Dieses Ergebnis kann durch die Hemmung der Rotation erklärt werden, die anisotrope Teilchen aufgrund stärkerer Verzahnung untereinander erfahren, und kann deutlich anhand der Wahrscheinlichkeitsverteilung des Rotationswinkels, um den sich die Teilchen während der Scherung gedreht haben, beobachtet werden. Die charakteristischen Moden, mit welchen anisotrope Teilchen Rotation akkumulieren, sind Vielfache von $\pi \, rad$.

Die Anisotropie der Teichen ist durch das Aspektverhältnis λ zwischen dem größten und kleinsten Teilchendurchmesser gegeben. Durch Variation des Aspektverhältnisses kamen wir zu den folgenden Schlussfolgerungen über die Parameter, die die granulare Packung im kritischen Zustand erreicht. Je größer die Anisotropie λ der Partikel,…

- …um so größer die Festigkeit des Materials im kritischen Zustand.
- …um so größer die Porenzahl im kritischen Zustand, und somit auch die volumetrische Deformation.
- …um so größer die Koordinationszahl Z der Teilchen. Für $\lambda > 2.3$ sättigt der Z-Wert und bleibt konstant.
- …um so größer die strukturelle Anisotropie im kritischen Zustand.
- …um so größer die Anisotropie der Teilchenorientierung im kritischen Zustand.
- …um so kleiner der mittlere akkumulierte Rotationswinkel $\langle \Theta \rangle$.
- …um so länger die notwendige Zeit, um das mikromechanische Gleichgewicht in der Orientierung von Struktur und Teilchen zu erreichen.

Um die Reibungsinstabilitäten, die im kritischen Zustand beobachtet wurden, genauer zu untersuchen, benutzen wir unser Modell mit polygonen Teilchen, um den sehr langsamen Scherprozess, wie er zum Beispiel bei Erdbebenverwerfungen auftritt, zu simulieren. Das Material in der Erdbebenstörung, der *Gouge*, hat starke Auswirkungen auf die Dynamik des Erdbebens, da man vermutet, dass es die Reibungsinstabilitäten, die den Erbebenprozess charakterisieren, bestimmt [49]. In Kapitel 5 verwenden wir isotrope und anisotrope polygone Teilchen zur Modellierung des *Gouge*. Wir modellieren die Verwerfungszonen durch Transform-St"orungen, das bedeutet, dass die Ränder der tektonischen Platten parallel zur Richtung orientiert sind, in welcher sich die tektonischen Platten bewegen [50, 51]. Diskrete Lawinen, deren Größe sich über mehrere Größenordnungen erstreckt, charakterisieren die dynamische Antwort des Systems. Dieses Verhalten deckt sich mit dem *crackling noise* physikalischer Systeme, welche durch diskrete Ereignisse unterschiedlicher Größe auf äußere Störungen reagieren [52].

Die Verteilung der Größe der Lawinen in unseren numerischen Simulationen stimmt gut mit dem Gutenberg-Richter-Gesetz, welches die Verteilung bei natürlichen Erdbeben

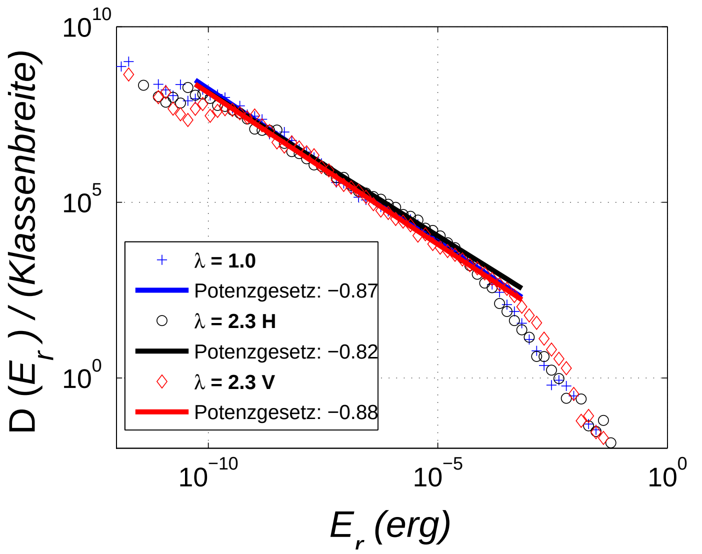

Figure 0.4: Die Abbildung zeigt die Anzahl der Ereignisse doppelt-logarithmisch aufgetragen gegen ihre freigesetzte Energie. Die Verteilung zeigt unterschiedliche λ-Werte. Es wird eine logarithmisches Klassenbreite verwendet.

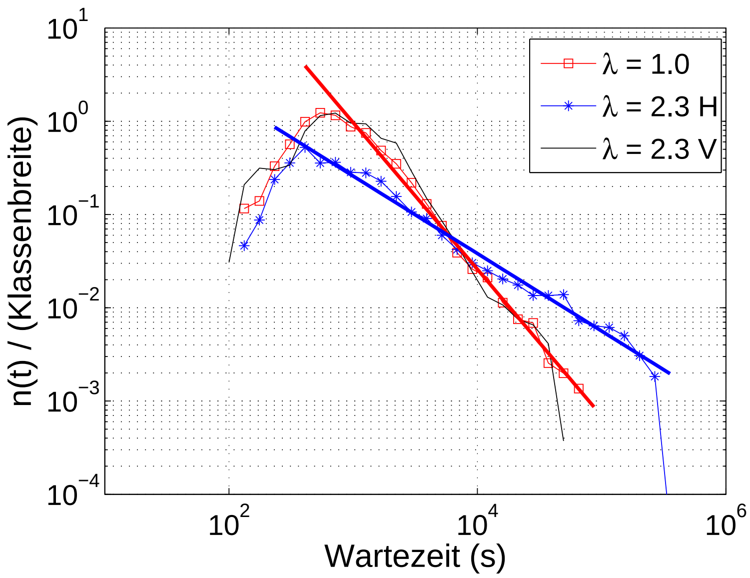

Figure 0.5: Verteilung $n(t)$ der Wartezeiten für Sequenzen von Nachbeben in der numerischen Simulation, in doppelt logarithmischer Auftragung. Es werden isotrope $\lambda = 1.0$ und anisotrope Teilchen $\lambda = 2.3$ dargestellt.

beschreibt, überein [53]. Die Verteilung gilt für sechs Größenordnungen und ist unabhängig von der Teilchenform (siehe Abb. 0.4). Wir stellen fest, dass die Anzahl der Ereignisse nach einem Hauptschock mit dem Kehrwert der Zeit, also ähnlich wie beim Gesetz von Omori [54], abnimmt. Die Wartezeiten von Nachschocksequenzen zeigen ein Potenzverhalten (siehe Abb. 0.5). Das wichtigere Ergebnis bezüglich des Einflusses der Form der anisotropen Teilchen auf die Systemdynamik ist aber, dass der Exponent des Potenzgesetzes von der ursprünglichen Probenkonfiguration und damit von der Teilchenformanisotropie abhängt. Anisotrope Proben mit Teilchen, die entlang der Scherrichtung orientiert sind, zeigen eine größere zeitliche Stabilität. Diese größere Stabilität kommt von der Hemmung von Deformationsmoden wie Rollen und Behinderung der Teilchenrotation. Auf makroskopischer Skala ist es daher möglich, die Anwesenheit von anisotropen Teilchen durch die zeitliche Verteilung von Ereignissequenzen zu überprüfen. Außerdem haben wir die Steifigkeit und die Reibungsstärke, welche das granulare System beim Entfestigen entwickelt, untersucht. Wir berechneten die Wahrscheinlichkeit einer Lawine und beobachteten, dass diese exponentiell mit der Steifigkeit abnimmt. Der Exponent ist dabei von der Teilchenformanisotropie abhängig. Anisotrope Proben zeigen aufgrund ihrer größeren mechanischen Stabilität einen größeren Steifigkeitsbereich, bevor eine Lawine auftritt. Die Reibung bei anisotropen Proben ist größer als bei isotropen; anisotrope Proben zeigen außerdem bei gleicher Reibung eine niedrigere Entfestigungs-Wahrscheinlichkeit. Einige mikromechanische Eigenschaften, welche als Vorboten von Lawinen gesehen werden können und eventuell auch ihr Auftreten erklären können, werden diskutiert.

In Kapitel 6 führen wir eine detaillierte Untersuchung der Grenzen für den Integrationsschritt der Diskreten-Element-Methode bei der Simulation von Kollision und Scherung von granularen Packungen durch. Konkret studieren wir dabei die Dynamik des Systems während der Relaxationsphase und zeigen, dass noch nicht garantiert werden kann, dass das System numerisch konvergiert, wenn man die obere Grenze für den Integrationsschritt, wie allgemein ”ublich, durch die durchschnittliche Kontaktdauer festsetzt [55]. Wir finden heraus, dass der Integrationsschritt deutlich kleiner gesetzt werden muss, als allgemein angenommen wird [56–58], um die Konvergenz des numerischen Schemas zu gewährleisten. Wir zeigen, dass der Wert der oberen Grenze für den Integrationsschritt sehr stark vom Ansatz, mit welchem die Tangentialkräfte berechnet werden, von der durchschnittlichen Kontaktzeit, sowie der Anzahl der Freiheitsgrade des Systems abhängt. Zum Schluss stellen wir einen Ansatz zur Berechnung der Tangentialkräfte vor, welcher einen deutlich höheren Zeitschritt ermöglicht und dennoch die Konvergenz des numerischen Integrationsschemas sicherstellt [59].

Im letzen Kapitel werden die Hauptergebnisse dieser Doktorarbeit zusammengefasst. Außerdem werden offene Fragen diskutiert und ein Ausblick auf mögliche weiterführende Arbeiten gegeben.

Chapter 1

Introduction

1.1 Motivation

Soil mechanics deals with the classification, properties and prediction of the mechanical behavior of soil bodies. Geotechnical engineers often classify such soil bodies as either cohesive or granular soils. While cohesive soils are typically composed of particles bound together with clay minerals, granular soils are formed from loose particles having weak inter-particle forces [4]. We will focus on this second type of soils.

Granular materials in general, and granular soils in particular, are ubiquitous in nature and engineering applications, being a determinant factor in shaping the world we live in. As illustrated in Fig. 1.1, they are observed in a wide variety of industrial activities such as mining, agriculture, construction and energy production and also in natural or geological processes, namely landslide, erosion and tectonic motion [4, 60]. Further, in civil engineering, most of the infrastructure projects such as buildings, highways, tunnels, bridges and dams use the granular soil either as foundation to support the structures or as construction material [23]. In this context, the understanding of the behavior of granular soils is therefore of utmost importance.

Granular soils exhibit a complex macro-mechanical behavior during loading. This macro-mechanical behavior is a result of the discrete character of the media and depends on the grains themselves, on the evolution of the granular structure and on some phenomena occurring at the grain scale such as rolling and sliding. This global response also involves the existence of the so-called asymptotic stress-strain states, which are independent of the initial state of the material.

One of the asymptotic states studied in soil mechanics is the so-called *critical state*. The understanding of the critical state is a major task since it plays a central role in constitutive modeling and in engineering applications. For example, it is used to define the failure criteria and post-failure behavior of many constitutive models [6–11].

The critical state was first described by Casagrande in 1936 [12]. From shear test on sand specimens he established that the stress-strain behavior of sand under large shear deformation reaches a limiting state, i.e. a critical volume or *critical void ratio*. This limiting state was independent of the initial density of the samples. Additionally, in the critical state the granular sample deformed without further volumetric and stress increments, namely strain and stress attained an asymptotic value. In the 60's, the non-linear behavior of soils was further characterized due to the development of the triaxial test by Bishop [13]. This lead to the development of elasto-plastic soil models such as the

Figure 1.1: Granular materials are present in a wide variety of industrial and natural/-geological processes such as (a) *Mining*, Yanacocha project, Perú, the world's largest gold mine [61] (b) *Construction*, Corin Dam, earth and rockfill embankment dam [62], (c) *Landslides*, la Conchita landslide in California 1995 [63], and (d) *Tectonic motion*, San Andreas Fault in California, US [64].

Cam-Clay model [14] and the stablishment of the Critical State Theory [6]. In these models, the soil response was described in terms of an initial elastic behavior followed by yielding, in which the soil reaches an ultimate critical state of unlimited shearing without changes in volume or effective stress. The critical void ratio is only dependent on the confining pressure, and thus the so-called critical state line relating the critical void ratio and the corresponding critical stress ratio can be defined. Experimentally, the existence and uniqueness of the critical state has been independently proven by Castro and co-workers [15] in 1975 and by Verdugo et al. [16] in 1996.

Another central issue in soils mechanics is the influence of particle shape on the mechanical behavior of granular soils. Particle shape has emerged as a significant soil property, particularly in sands and gravels, affecting small-strain stiffness, compressibility, strength parameters and anisotropy [19–21]. However, while usually grain size and size distribution are widely recognized as important factors for the mechanical behavior of soils [4, 22, 23], up to now the role of anisotropic particle shape is not as well studied. The relationship between anisotropic particle shape and anisotropy has to be evaluated, since anisotropy affects properties such as deformation, strength and permeability [21].

Casagrande and Carrillo [65] distinguished between inherent and induced anisotropy, as a result of the sedimentation of particles and as a product of inelastic deformation, respectively. Oda et al. [66] and Oda and Nakayama [67] listed three sources for the inherent anisotropy: (i) anisotropic distribution of contacts or fabric anisotropy, also called structural anisotropy, (ii) shape and preferred orientation of void spaces and (iii) shape of the particles and preferred orientation of non-spherical ones. The complete alteration of inherent anisotropy due to types (i) and (ii) during early stages of inelastic deformation in biaxial compression tests, on two-dimensional assemblies of rods, was also observed by Oda et al. [66]. They found, however, that the one due to type (iii) was still present at large deformations. Therefore, it is expected that at the critical state [6, 11], associated with large shear deformation, the persistence of inherent anisotropy is mainly due to the orientation of non-spherical particles [68]. The induced anisotropy in flows of non-spherical particles has been studied, both experimentally and analytically, by Ehrentraut and Chrzanowska [69]. Experimentally, they observed ordering of the grains (rice) and flow alignment in shear flow boundary conditions. In addition, they confirmed that particle geometry hinders the rolling motion and enhances the sliding of the grains. Experimentally, Bowman and Soga [70] found that the stress-strain and creep response of fine silica sand is influenced by particle elongation.

The influence of anisotropic particle shape on the mechanical behavior of soils is therefore an important and open problem to be addressed in both engineering applications and the modeling of granular soils [1, 19, 21].

In the context of granular soil models, different methods have been developed in order to predict and comprehend soil behavior. One of the most common approaches is the Finite Element Method (FEM), where the medium is considered as a continuum, the equations of continuum mechanics are discretized and boundary value problems can be solved. This method requires as input a constitutive relation, i.e. a relation between stress (force transmission) and strain (deformation). Many different constitutive laws have been proposed in the last decades. There are two fundamental drawbacks with these relations: either they yield satisfactory results under the experimental conditions in which they were built up or they involve a large number of parameters, that either lack of physical meaning or are very difficult to calibrate with experimental data [1]. Some constitutive models have attempted to relate grain characteristics to the material parameters of the model [71], but there is still much to do concerning the physical meaning of the parameters and certain behaviors such as hysteresis, creep, ageing and liquefaction.

Numerical simulations using the discrete element method (DEM) have also been a promising tool in the study of granular materials [2, 3]. In DEM the mechanical response of the media is obtained by modeling the interactions between the individual particles as a dynamic process and using simple mechanical laws in these interactions. Furthermore, particle shape, size distribution, cohesion etc can be taken into account.

The DEM allows us to study and understand the phenomena occurring at the grain scale level and therefore allows for the consequent comprehension of the related global response of the media. Remarkable advances using DEM have been achieved in the field of soil mechanics, e.g., the understanding of the micro-mechanism governing the response under cyclic loading or granular ratcheting [34], and the study of particle crushing and through it the potential explanation of the plastic yielding and the plastic hardening phenomena [1, 72–74].

Generally, discrete models use discs [2, 26–28] or spheres [3, 29, 30]. The simplicity of their geometry enables the reduction of the computational time by using simple interaction laws. They do not consider, however, the diversity of shapes of the constituent grains in natural materials and hence none of the scales in particle shape [21, 24]. Particle shape is classified according to three main scales, namely sphericity or platiness, roundness or angularity, and roughness. The first two scales manifest at the scale of the particle diameter (see Fig. 1.2a), while roughness involves features of smaller scale [21, 75].

1.2 Scope

In this thesis we study two central problems related with each other. On one hand, we deal with the problem of existence and uniqueness of the critical state. On the other hand we study the influence of particle shape anisotropy in the macro-mechanical response of sheared granular packing. To this end, we deal with DEM models of granular soils where the global response is strongly dependent on the discrete character of the medium.

To take into account the influence of particle shape we represent grains by randomly generated convex polygons. These reproduce the two principal scales of shape irregularity present at the level of the particle diameter [19, 20, 76]: sphericity (shape anisotropy) and roundness (angularity) as sketched in Fig. 1.2. Thus, our particle model not only enables the representation of the main features observed in granular packing, such as elasticity, structural anisotropy, friction, stick-slip and loss of energy during collisions, but also considers the important geometrical effect of particle shape allowing for a more realistic soil representation. In particular, we study in this context the stress-strain response, strain accumulation, and fabric evolution of the granular packing under shearing.

Concerning the critical state some researchers assert that such state depends on the consolidation history of sand [17] and challenge its uniqueness [18]. In order to assess the existence and uniqueness of the critical state we undertake a robust program of nu-

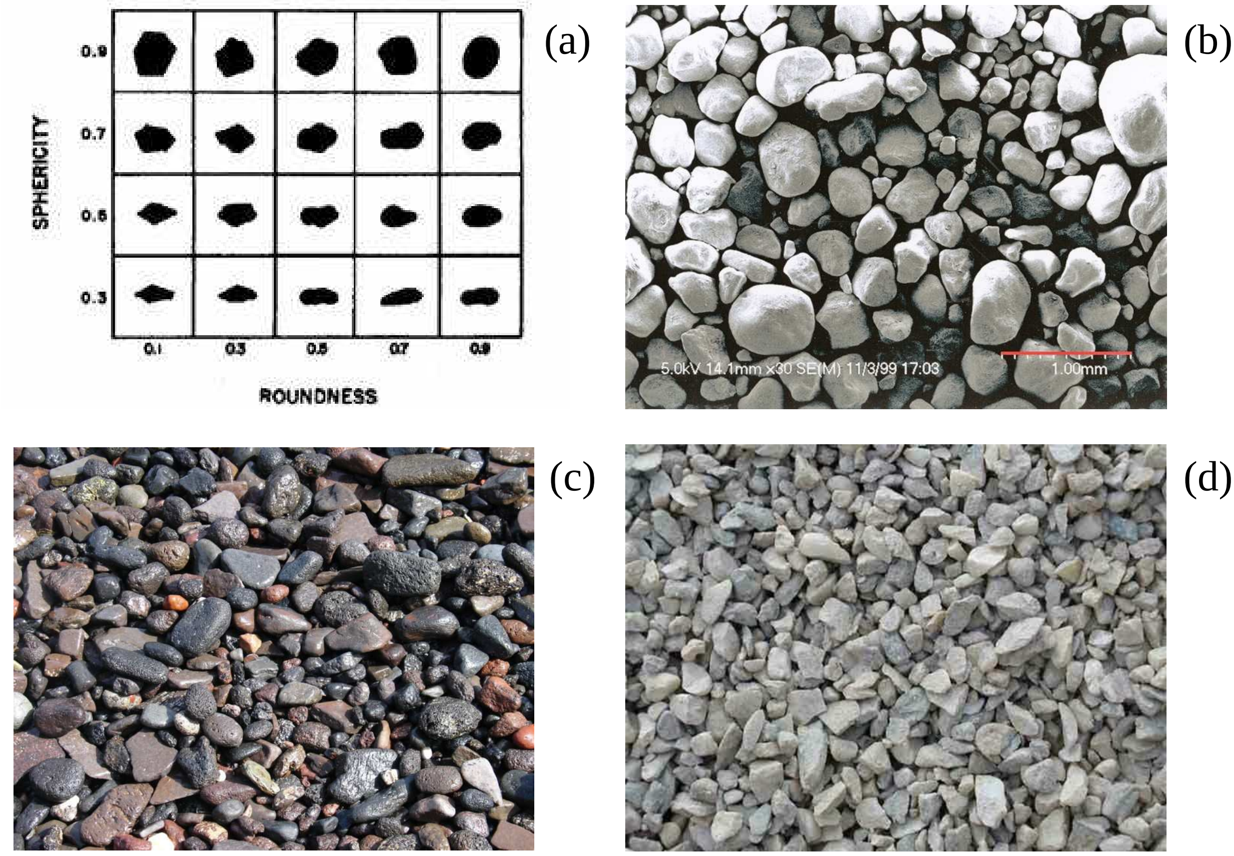

Figure 1.2: Particle shape characteristics of granular material (a) Sphericity and roundness chart used in practice to evaluate particle shape characteristics [24], (b) natural quartz sand excavated 4 meters below the ground surface, Hwange National Park, Zimbabwe [25], (c) natural gravel on a beach in Thirasia, Greece [77] and (d) crushed gravel with mean size two cm [78].

merical simulations performing biaxial and shear cell tests and using different initial conditions. We also address the problem of the lack of clear information at the micromechanical level. This concerns the influence of particle shape and the orientation of anisotropic particles on the evolution of granular soils and the corresponding anisotropic network of contacts towards the critical state. The role of anisotropic particle shape on the mechanical behavior, i.e. stress-strain response and particle rotation, is also studied. Further, we investigate the deformation patterns at small and large deformation stages of the granular packing. The characteristic modes of deformation considered are rotation and rolling of particles [31–33], contact sliding [34, 35] and localization of strain in narrow shear bands [26, 36, 37].

At the critical state the granular packing exhibit force fluctuations. These fluctuations are also observed in monotonic tests on glass bead samples [40] and packing of glass spheres [79]. Experimental biaxial tests also show evidence of dynamic instabilities at the critical state [80]. The force fluctuations are related to the frictional instabilities or stick-slip motion, study of both are considerably important owing to their potential analogy with the earthquake dynamics [42].

To further study such frictional instabilities, using our model of polygonal particles we simulate very slow shearing processes as in the case of earthquake faults, e.g. the San Andreas Fault presented in Fig. 1.1d. The material within the earthquake fault, *the gouge*, has deep implications on the earthquake dynamics, since it is thought to control the frictional instabilities characterizing the earthquake process [49]. Since numerical particle models of earthquake fault usually represent the gouge as being composed by discs [42, 81] or spheres [29], the influence of particle shape on the earthquake is still an open problem to be addressed. In this thesis, we use isotropic and anisotropic polygons to study the influence of anisotropic particles as constituent of the gouge on the dynamic of the granular system under slow shearing.

Finally, from the computational point of view, some additional improvements are introduced into the numerical method. In DEM, depending on the case of study, e.g. earthquake faults, very small shear rates are required to capture the dynamics of the real system [42, 81]. In such cases the large integration steps adopted to avoid unreasonable computational effort may introduce new problems such as convergence of the numerical scheme. The upper limit for the integration step is usually defined on empirical reasoning [56]. We uncover a convergence problem related to the calculation of the tangential forces, that vanishes by using integration steps much smaller than the upper limit typically used. We propose a new approach to calculate the tangential force that allows the use of larger integration steps.

1.3 Overview

This thesis is organized as follows: In Chapter 2, we introduce the main features of our two-dimensional polygonal DEM model. The procedure to generate anisotropic polygons and the criteria used to select the integration step for the numerical simulation are discussed.

In Chapter 3, we perform biaxial test simulations on isotropic granular packing to study the existence of the critical state and the role of the deformation patterns on strain accumulation under monotonic loading. Two different stages of the deformation are investigated, namely small [38], and large shear deformations [48]. For small deformation, we study the first steps of strain localization and/or shear band formation as well as the related micro-mechanisms. For large deformation, we study the evolution of the granular packing toward the so-called critical state. We show that in the numerical simulations the granular media evolve toward a limiting state in which the system reaches a critical void ratio and deforms with constant volume and deviatoric stress.

At the critical state, the dynamical response of the system is characterized by stress fluctuations that appear as a consequence of frictional instabilities. The stress fluctuations are related to the force chains collapses that remove the contacts from the sliding condition and lead the system to a temporal stability. We also investigate the dependency of the overall response of the media on the interparticle friction. For zero interparticle friction coefficient the system presents a small but significant shear strength, showing that the interparticle friction is not the unique cause of the macroscopic frictional behavior of granular materials. This supports the idea the nonlocal behavior of granular assemblies.

In Chapter 4, we focus on the influence of anisotropic particle shape on the overall mechanical response. Biaxial and periodic shear cell experiments are performed. The dependency of the mechanical behavior on the evolution of inherent anisotropy regarding contact and anisotropic particle orientations is studied. We find an important influence of the particle shape anisotropy on the evolution of the stress-strain response, on the evolution of the anisotropic contact network, on the time for the system to reach the asymptotic state, and on the particle rotation.

In the periodic shear cell, the results at macro-mechanical level show that for large shear deformations samples with anisotropic particles reach the same critical value for both shear force and void ratio independent of their initial orientations [48]. At the micro-mechanical level the components of the stress, the fabric and the inertia tensors of the particles also attain the same stationary state. This is stated as a micromechanical requirement for the system to attain the critical state at the macro level.

In Chapter 5, we mimic fault zones with transform boundaries, i.e. the boundaries of the tectonic plates are parallel to the direction along which the tectonic plates move [50, 51]. Isotropic and anisotropic polygonal particles are used to represent the gouge. Discrete avalanches with size spanning several orders of magnitude characterize the dynamical response of the system. This behavior is in agreement with the crackling noise of physical systems, in which the response of the system to the external conditions is given by discrete events of a variety of sizes [52].

The distribution of the magnitude of the avalanches in our numerical simulations is in good agreement with the Gutenberg-Richter law describing the distribution of natural earthquakes [53]. We find that the number of events after a mainshock decrease with the inverse of time similar to the Omori's law [54]. The exponent of the decay depends on the initial sample configuration and hence on the particle shape anisotropy. At the macromechanical level, therefore, it is possible to verify the presence of anisotropic particles studying the temporal distribution of event sequences. We also study the stiffness and frictional strength that the granular system develops at failure. We calculate the probability of occurrence of an avalanche for given values of stiffness or frictional strength. Relevant influence of the particle shape anisotropy is observed.

In Chapter 6, we perform a detailed analysis of the limits used for the integration step in the Discrete Element Method when collision and shearing of granular assemblies are simulated. In particular, we study the dynamics of the system during the relaxation stage and show that the upper limit for the integration step, usually taken from the average duration of one contact [55], is not sufficiently small to guarantee numerical convergence of the system. We find that the proper integration step to assure the convergence of the numerical scheme has to be significantly smaller than the upper limit commonly accepted [56–58]. We show that the upper limit for the integration step is strongly dependent on the approach used to calculate the tangential forces between the particles, on the average duration of one contact and on the number of degrees of freedom of the system. Finally, we propose an alternative approach to compute the tangential forces that allows the use of considerably larger integration steps and assures the convergence of the numerical integration scheme [59].

Finally, in Chapter 7 we present a summary of the main results of this thesis. This is followed by remarks on the open questions and perspectives for future work.

Chapter 2

The Model

Most of the discrete element models use discs or spheres to represent the constituents particles of granular packing. The simplicity of their geometry reduce the computational time of the simulations, and allows to use simple contact force laws in the calculation of the interactions. However, these models do not take into account the diversity of shapes of the grains in realistic granular materials, and consequently are unable to ascertain their influence on the micro and macro-mechanical behavior of the system.

In this chapter, we present a detailed review of the two-dimensional discrete element method that has been used to model granular materials using polygonal particles [37, 82–84]. Polygonal particles are more realistic because they exhibit two of the three main scales of particle shape irregularity, namely sphericity or platiness, and roundness or angularity [21]. The one left is the surface roughness, which involves features of smaller scale than particle diameter [21, 75]. Therefore, this model of polygonal particles takes into account not only important features of granular materials such as elasticity, frictional forces, stick-slip, and loss of energy during collisions, but also the geometrical effect of particle shape on the overall mechanical behavior allowing for a more realistic soil representation. Due to the nature of our two dimensional analysis a suitable interpretation of the results has to be done through comparisons with 3 dimensional models, and experimental observations.

In the following sections we describe the relevant aspects about molecular dynamic simulations, the contact laws and the related open issues, the numerical integration scheme, the procedure for particle and sample generation, the search of neighbors, the imposed boundary conditions, the parameters of the simulation and some additional remarks.

2.1 Molecular dynamics simulation

In numerical simulations using the molecular dynamic (MD) technique the mechanical response of the media is obtained by modeling the particle interactions as a dynamic process and using simple mechanical laws in these interactions. Within the granular media each particle is subjected to contact forces, specifically forces f^c from interparticle contacts and forces f^b from contact with the boundaries. When these forces are known, the evolution of the position $\vec{r}_i$ and orientation θ_i of the i polygon is given by the integration of Newtons's equation of motion:

$$m_i \ddot{\vec{r}}_i = \sum_c \vec{f}_i^c + \sum_{c_b} \vec{f}_i^b \tag{2.1a}$$

$$I_i \ddot{\theta}_i = \sum_c \vec{l}_i^c \times \vec{f}_i^c + \sum_{c_b} \vec{l}_i^b \times \vec{f}_i^b \tag{2.1b}$$

where m_i denotes the mass of particle i, I_i is its moment of inertia and $\vec{l}^c$ is the branch vector which connects the center of mass of the polygon to the contact point. The sum in c is over all the particles in contact with polygon i, and the sum in c_b is over all the vertices of the polygon in contact with the boundary.

The force laws and definition of contact and boundary forces are introduced in Sec. 2.2 and Sec. 2.6, respectively.

2.2 Contact law

Pioneering work in the field of discrete element method applied to granular materials was performed by Cundall in the late 70's [2], in that work he uses disks to represent the particles and defines the contact forces to be proportional to the relative displacement of the particles in contact.

In the case of polygonal particles, the definition of contact forces between them is far to be trivial. An usual approach is to assume that particles interact elastically with each other, and they can neither be broken nor deformed, but they can overlap when they are pressed against each other. This overlap represents the local deformation of the grains, and thus the corresponding repulsive contact force is calculated as a function of this overlap [37, 85]. For the calculation of the contact force an appropriate definition of the overlapping length and the contact reference system defining the orientation of the forces is required. It is desirable that these two quantities change continuously with time. Time discontinuities in the force might eventually lead to numerical problems in the integration of the equation of motions and in the convergence of the solution.

In the case of disks, the direction of the contact forces and the penetration length are well defined. For polygonal particles, the orientation of the overlap area representing the flattened contact surface of the particles in contact is here calculated from the intersection points of the boundary of the overlapping polygons. In Figure 2.1 the configuration of a particle contact is presented. Points P_1 and P_2 represent the intersection points between the edges of the polygons and the segment that connects those points gives the contact line $\vec{S} = P_1P_2$. This vector $\vec{S}$ defines a coordinate system $(\hat{n}, \hat{t})$ at the contact, where $\hat{t} = \vec{S}/|\vec{S}|$ and $\hat{n}$ normal to it give the direction of the tangential f_t and normal f_n components of the contact force. The contact point, i.e. the point of application of the contact forces is taken as the center of mass of the overlap area A. Since the point of application of the force is not collinear with the centers of mass of the interacting polygons, there is a contribution of the torque from both components of the contact force. This makes an

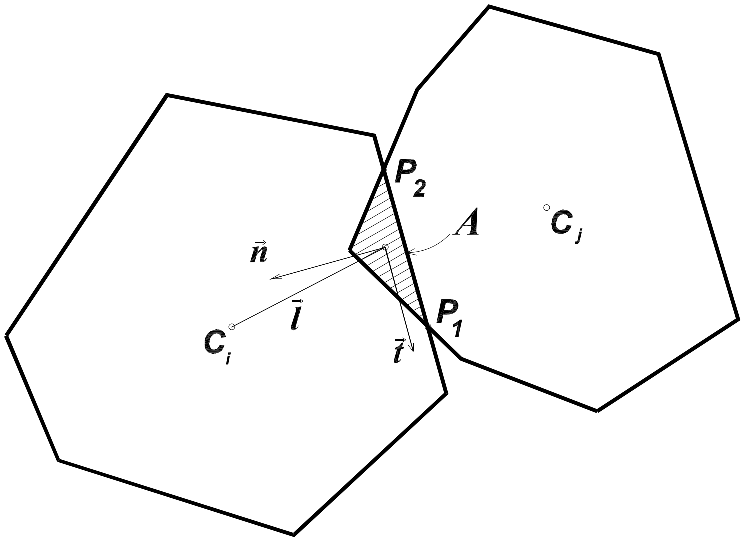

Figure 2.1: Schematic representation of a particle contact, the overlapping area A is indicated by the shaded zone.

important difference with respect to the interaction between disks or spheres: Polygons can transmit torques even in the absence of frictional forces.

In most of the cases, we have only two intersection points and the direction of the contact line $\vec{S}$ is therefore unique. Nevertheless, when more than two intersection points occurred, as presented in Fig. 2.2, the uniqueness of the orientation of $\vec{S}$ is lost. We refer to this situation as pathological contacts, since it does no represent a realistic contact situation. In order to have a continuous change of $\vec{S}$ [82], in the case of more than two intersection points the contact line is defined by the vector $\vec{S} = \overrightarrow{P_1P_2} + \overrightarrow{P_3P_4}$ or $\vec{S} = \overrightarrow{P_1P_2} + \overrightarrow{P_3P_4} + \overrightarrow{P_5P_6}$, for four or six intersections points respectively.

The contact forces, are decomposed into their elastic and viscous contributions, namely $\vec{f^c} = \vec{f^e} + \vec{f^v}$. The elastic part $\vec{f^e}$ of the contact force is simply given by the sum of its normal and tangential components:

$$\vec{f^e} = f_n^e \hat{n}^c + f_t^e \hat{t}^c \tag{2.2}$$

with respect to the contact plane. Next, we explain how the normal f_n^e and tangential f_t^e components are calculated.

2.2.1 Normal elastic force

Contrary to the case of spheres [86], for particles with arbitrary shape there is no analytical derivation for the force-displacement behavior of particles in contact. In the approach we use for the calculation of the contact force the particle shape is taken into account. We assumed that the overlap of the particles is a measure of the way particles deform and is

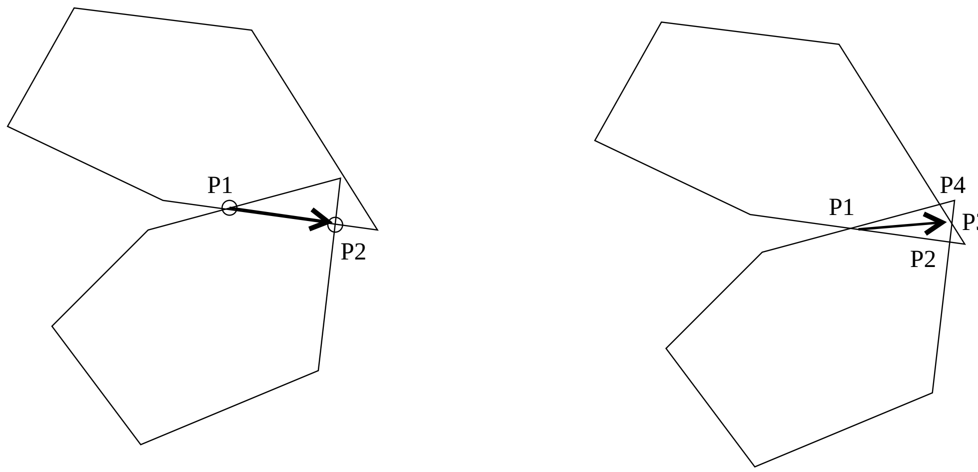

Figure 2.2: Formation of a pathological contact, i.e a contact in which more than two contact points are involved. Lower particle moves through the other particle generating four intersection points.

therefore proportional to the repulsive force between them [37]. Thus, the normal elastic force is equal to

$$f_n^e = -k_n(A/l_c), \tag{2.3}$$

with k_n the normal stiffness, A the overlapping area and l_c the characteristic length of the contact. This characteristic length is given by $l_c = c_i + c_j$, with $c_i = \sqrt{A_i/\pi}$ where A_i is the area of polygon i, and similarly for particle j. Due to the reduced dimensionality of our 2D model, the stiffness k_n has units of N/m, and therefore the normalization of A with l_c is required for consistency of units.

2.2.2 Tangential elastic force

In our model, the frictional force is given by a tangential elastic force between each pair of particles. This force is obtained using an extension of the Cundall-Stack spring [2], as follows, the force is considered to be proportional to the elastic elongation ξ of an imaginary tangential spring at each contact, namely

$$f_t^e = -k_t\xi, \tag{2.4}$$

where k_t is the tangential stiffness. Through time, the elastic elongation ξ is updated as

$$\xi(t + \Delta t) = \xi(t) + \vec{v}_t^c \Delta t \tag{2.5}$$

where Δt is the time step of the molecular dynamic simulation, and $\vec{v}_t^c$ the tangential component of the relative velocity $\vec{v}^c$ at the contact point between the two particles.

$$\vec{v}^c = \vec{v}_i - \vec{v}_j + \vec{w}_i \times \vec{l}_i - \vec{w}_j \times \vec{l}_j. \tag{2.6}$$

Here $\vec{v}_i$ and $\vec{v}_j$ are the linear velocities, and $\vec{w}_i$ and $\vec{w}_j$ are the corresponding angular velocities. The tangential elongation ξ increases in time whenever the elastic condition

$$|f_e^t| < \mu f_e^n, \tag{2.7}$$

is satisfied, whereas the sliding condition is enforced by keeping constant the elastic displacement ξ when the Coulomb limit condition is reached, namely $|f_e^t| = \mu f_e^n$. This latter condition corresponds to the inelastic regime, where the elongation takes its limiting values $\xi = \pm\mu k_n A/(k_t l_c)$ (see Eqs. (2.3) and (2.4)), while the former in Eq. (2.7) corresponds to the elastic regime. Parameter μ is the inter-particle friction coefficient.

The Cundall-Strack model has been widely used in the literature, since its implementation requires practically no computational effort and has been proven to be in good agreement with the simulation of static behavior of packings [87, 88], and to reproduce important features of the plastic deformation of soils, such as the plastic flow-rule [89] and stick-slip fluctuations [39, 42]. A clear drawback of this method is that it introduces a time integration error of $O(\Delta t^2)$, as seen from Eq.(2.5), in contrast with the much smaller error introduced by the numerical integration schemes used to calculate the system evolution.

In recent work, McNamara et al. [90] find that the Cundall-spring produces a path-dependent elastic potential energy in the contact, and that due to this dependence behaviors such the so-called granular ratcheting [34] can emerge.

In Chapter 6 of this thesis, we will discuss some other numerical problems arising from the Cundall-Strack spring model. We will mainly deal with the divergence of the numerical solution for shearing and relaxation of the granular packings [59]. For this situation, we introduce an alternative approach based in geometrical relations to compute the frictional forces, that corrects properly the evolution of the system and enables the usage of larger integration steps.

2.2.3 Damping forces

Viscous forces are introduced in order to take into account dissipation at the contact, maintain numerical stability of the method, and obtain quick convergence to the equilibrium configuration. These forces are calculated as

$$\vec{f}_v^c = -m_r(\nu_n\, \vec{v}_n^c\, \hat{n}^c + \nu_t\, \vec{v}_t^c\, \hat{t}^c) \tag{2.8}$$

where $m_r = (1/m_i + 1/m_j)^{-1}$ is the reduced mass of the two particles in contact, and ν_n and ν_t are the damping coefficients.

Since almost any value of the damping coefficient ν might be selected. A straightforward way to choose the value of ν is to relate it to the corresponding value of contact stiffness k through the coefficient of restitution ϵ. One can then select one value for ϵ from the range of values of the restitution coefficient obtained experimentally on various materials [91]. The restitution coefficient is given by the ratio between the relative velocity after and before the collision. In particular, the normal restitution coefficient ϵ_n

can be written as a function of k_n and ν_n [55], namely

$$\epsilon_n = \exp\left(-\pi\eta/\omega\right) = \exp\left(-\frac{\pi}{\sqrt{4m_r k_n/\nu_n^2 - 1}}\right) \tag{2.9}$$

where $\omega = \sqrt{\omega_0^2 - \eta^2}$ is the frequency of the damped oscillator, $\omega_0 = \sqrt{k_n/m_r}$ is the frequency of the elastic oscillator corresponding to the pair of particles in contact, and $\eta = \nu_n/(2m_r)$ is the effective viscosity, with ν_n the damping coefficient in the direction perpendicular to the contact plane. The tangential component ϵ_t of the restitution coefficient is defined similarly using k_t and ν_t in Eq. (2.9). Next, we explain how the numerical integration scheme is used to solve the equations of motion.

2.3 Numerical Integration Scheme

To solve the equations of motion we use the Gear's predictor-corrector scheme [56]. This scheme consist of three main stages, namely prediction, evaluation and correction.

In the prediction stage the position, velocities and higher-order time derivatives are updated by expansions of the corresponding Taylor series using the current values of these quantities [56, 92]. For the position $\vec{r}$ of the center of mass these equations read

$$\vec{r}_{(t+\Delta t),p} = \vec{r}_{(t)} + \dot{\vec{r}}_{(t)}\,\Delta t + \ddot{\vec{r}}_{(t)}\,\frac{\Delta t^2}{2!} + \vec{r}^{\,iii}_{(t)}\,\frac{\Delta t^3}{3!} + \vec{r}^{\,iv}_{(t)}\,\frac{\Delta t^4}{4!} + \vec{r}^{\,v}_{(t)}\,\frac{\Delta t^5}{5!} \tag{2.10a}$$

$$\dot{\vec{r}}_{(t+\Delta t),p} = \dot{\vec{r}}_{(t)} + \ddot{\vec{r}}_{(t)}\,\Delta t + \vec{r}^{\,iii}_{(t)}\,\frac{\Delta t^2}{2!} + \vec{r}^{\,iv}_{(t)}\,\frac{\Delta t^3}{3!} + \vec{r}^{\,v}_{(t)}\,\frac{\Delta t^4}{4!} \tag{2.10b}$$

$$\ddot{\vec{r}}_{(t+\Delta t),p} = \ddot{\vec{r}}_{(t)} + \vec{r}^{\,iii}_{(t)}\,\Delta t + \vec{r}^{\,iv}_{(t)}\,\frac{\Delta t^2}{2!} + \vec{r}^{\,v}_{(t)}\,\frac{\Delta t^3}{3!} \tag{2.10c}$$

$$\vec{r}^{\,iii}_{(t+\Delta t),p} = \vec{r}^{\,iii}_{(t)} + \vec{r}^{\,iv}_{(t)}\,\Delta t + \vec{r}^{\,v}_{(t)}\,\frac{\Delta t^2}{2!} \tag{2.10d}$$

$$\vec{r}^{\,iv}_{(t+\Delta t),p} = \vec{r}^{\,iv}_{(t)} + \vec{r}^{\,v}_{(t)}\,\Delta t \tag{2.10e}$$

$$\vec{r}^{\,v}_{(t+\Delta t),p} = \vec{r}^{\,v}_{(t)} \tag{2.10f}$$

From the equations above, one extracts a predicted position $\vec{r}_{(t+\Delta t),p}$ and acceleration $\ddot{\vec{r}}_{(t+\Delta t),p}$. During the evaluation stage, one uses the predicted coordinate to determine the contact force $\vec{f}^{\,c}_{t+\Delta t}$ at time $t+\Delta t$. Since the method is not exact, there is a difference between the acceleration $\ddot{\vec{r}}_{(t+\Delta t)} = \vec{f}^{\,c}_{t+\Delta t}/m$ and the value obtained in the prediction stage, namely

$$\Delta\ddot{\vec{r}} = \ddot{\vec{r}}_{(t+\Delta t)} - \ddot{\vec{r}}_{(t+\Delta t),p}. \tag{2.11}$$

The difference in Eq. (2.11) is used in the corrector step to correct the predicted position and time derivatives. This correction is performed using proper weights α_i for each time derivative [56], as follows [92]

$$\vec{r}_{(t+\Delta t)} = \vec{r}_{(t+\Delta t),p} + \alpha_0 \frac{\ddot{\vec{r}}\Delta t^2}{2!} \tag{2.12a}$$

$$\dot{\vec{r}}_{(t+\Delta t)}\,\Delta t = \dot{\vec{r}}_{(t+\Delta t),p}\,\Delta t + \alpha_1 \frac{\ddot{\vec{r}}\Delta t^2}{2!} \tag{2.12b}$$

$$\ddot{\vec{r}}_{(t+\Delta t)}\,\frac{\Delta t^2}{2!} = \ddot{\vec{r}}_{(t+\Delta t),p}\,\frac{\Delta t^2}{2!} + \alpha_2 \frac{\ddot{\vec{r}}\Delta t^2}{2!} \tag{2.12c}$$

$$\vec{r}^{\,iii}_{(t+\Delta t)}\,\frac{\Delta t^3}{3!} = \vec{r}^{\,iii}_{(t+\Delta t),p}\,\frac{\Delta t^3}{3!} + \alpha_3 \frac{\ddot{\vec{r}}\Delta t^2}{2!} \tag{2.12d}$$

$$\vec{r}^{\,iv}_{(t+\Delta t)}\,\frac{\Delta t^4}{4!} = \vec{r}^{\,iv}_{(t+\Delta t),p}\,\frac{\Delta t^4}{4!} + \alpha_4 \frac{\ddot{\vec{r}}\Delta t^2}{2!} \tag{2.12e}$$

$$\vec{r}^{\,v}_{(t+\Delta t)}\,\frac{\Delta t^5}{5!} = \vec{r}^{\,v}_{(t+\Delta t),p}\,\frac{\Delta t^5}{5!} + \alpha_5 \frac{\ddot{\vec{r}}\Delta t^2}{2!} \tag{2.12f}$$

These weights depend upon the order of the algorithm and the differential equation being solved. In our simulations we integrate equations of the form $\ddot{\vec{r}} = f(\vec{r}, \dot{\vec{r}})$, and use a fifth order predictor-corrector algorithm [56]. The coefficients α_i for this situation are: $\alpha_0 = 3/16$, $\alpha_1 = 251/360$, $\alpha_2 = 1$, $\alpha_3 = 11/18$, $\alpha_4 = 1/6$ and $\alpha_5 = 1/60$.

Finally, the corrected values are used for the next integration step $t + \Delta t$, and the procedure starts again from these values to further integrate the system's evolution. The resulting numerical error for the fifth order integration scheme is proportional to $(\Delta t)^6$.

While the expansions above for $\vec{r}$ and corresponding time derivatives describe the dynamics of the center of mass of the particles, the same procedure is equally applied for the rotation angles θ_i around the center of mass as well as for their time derivatives.

2.4 Particle and sample generation

2.4.1 Generation of polygons

The random generation of the convex polygons used in this model is carried out by means of a special form of the Voronoi tessellation, which is a simple method to discretize a media. The special form of the Voronoi tessellation is the so-called vectorizable random lattice and was developed by Mourkazel and Herrmann [93]. The discretization using this method does not introduce any kind of anisotropy to the media.

The first step of the discretization is to define a reference regular square lattice with cell size ℓ, as presented in Fig. 2.3. Next, in each cell of the reference lattice a point is randomly set within a square of length a. This square region, where the point is set, is centered on the reference cell. The value of a varies in the interval $0 \leq a \leq \ell$. The polygons are then constructed by assigning to each point the part of the plane that is nearer

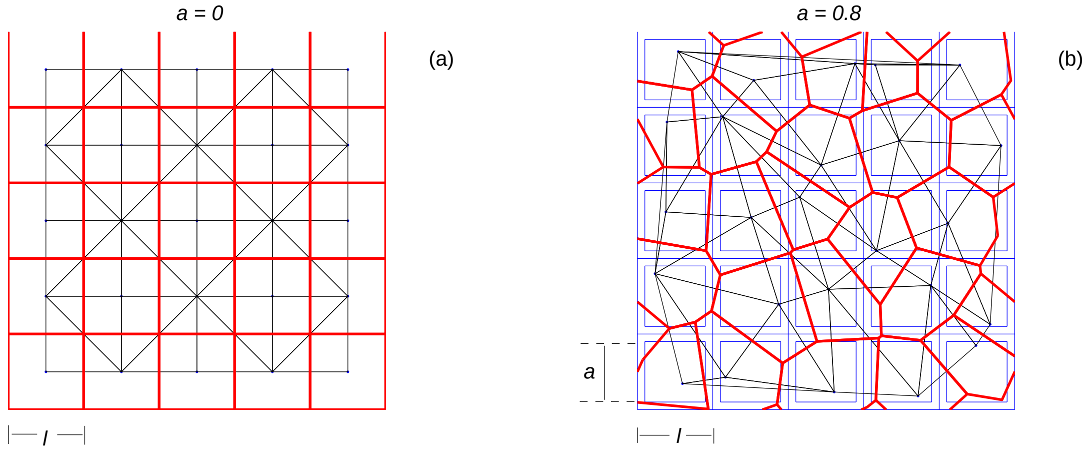

Figure 2.3: Construction of vectorizable random lattice. The thin line (black in color) connecting the random points represents the random lattice. The thick lines (red lines in color) are the edges of the polygons obtained from the Voronoi tessellation. Two values of a are used, 0.0 (reference lattice) and 0.8 (random lattice).

to it than to any other point. In Fig. 2.3, the vectorizable random lattice is represented by the black line connecting the random points and the edges of the polygons are plotted as red lines. By using different seeds for the random generation of the points, we end up with different Voronoi tessellations and thus different initial sample configurations.

The degree of randomness of the tessellation is controlled by the parameter a, where the upper limit $a = \ell$ yields the maximal randomness and the lower limit $a = 0$ the original reference lattice (Fig. 2.3). Furthermore, the closer the parameter a is to ℓ the smaller the corresponding anisotropy. In this case, anisotropy refers to the distribution of the orientation of the edges of the polygons. In particular, for $a = \ell$ this distribution is isotropic. The outcome of the Voronoi tessellation using the vectorizable random lattice for different values of a is depicted in Fig. 2.4. For further details about the Voronoi construction see [93–95].

For molecular dynamics, the vectorizable random lattice has also the computational advantage that the potential number of neighbors of each cell is limited to 20, while in the case of the standard or Poissonian Voronoi tessellations the possible number of neighbors is not bounded [93]. The fact of having a bounded number of potential neighbors enables to fix the list for the calculation of particles interactions leading to a reduction of the computer time of the simulation [37, 82].

Concerning the geometrical properties of the Voronoi tessellation, one can see in Fig. 2.5 that the distribution of the area of particles is approximately symmetric around ℓ^2. The larger the parameter a the wider the distribution of areas. We use five different values of $a = \ell$, 0.75ℓ, 0.5ℓ, 0.25ℓ and $1.0 \times 10^{-6}\ell$. The corresponding standard deviations are 0.25, 0.19, 0.067 and $2.8 \times 10^{-7}\ell$. The average number of edges of the Voronoi polygons

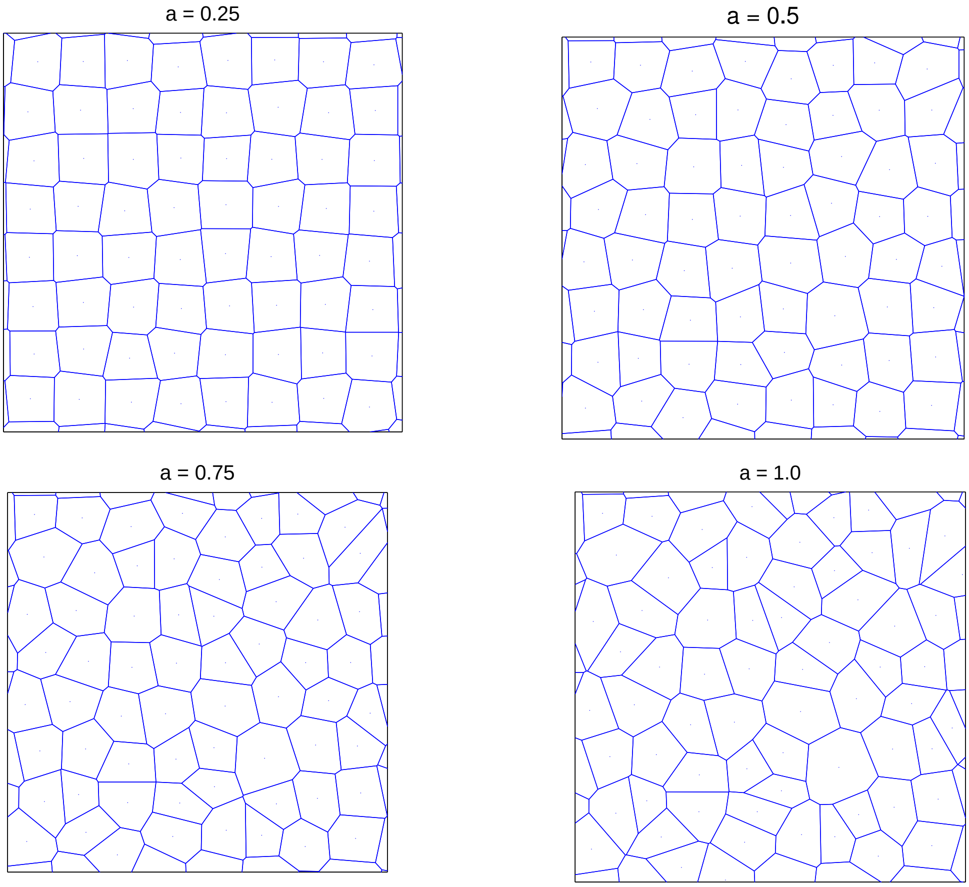

Figure 2.4: Outcome of the Voronoi construction using different values of the parameter a. Periodic boundary conditions are used.

depends just weakly on a as illustrated in Fig. 2.6. This average number of edges for any random tessellation has been shown analytically [95] and using numerical simulations [93] to be 6. Nevertheless, one can observe that the larger the value of a the more diverse the number of edges and therefore the less the angularity of the particles, as can be seen in Fig. 2.4. Systematic study of the influence of particle angularity, i.e. the influence of the number of edges on the mechanical behavior of granular assemblies was already performed by Mirghasemi et al. [20]. In this work, we use $a = \ell$ that gives Voronoi constructions with the wider distribution of areas. Since the polygons fill completely the plane, in order to create porous material an additional procedure has to be performed. It is explained in the next section.

2.4.2 Generation of samples

In this Section, we will explain how using the outcome of the Voronoi tessellation samples with different porosities and with anisotropic, i.e. elongated particles, are con-

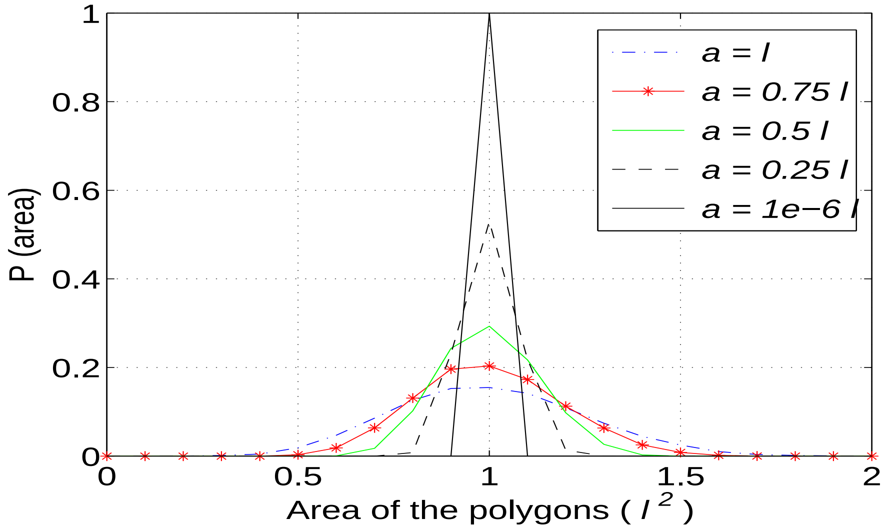

Figure 2.5: Probability distribution function of polygon areas of the Voronoi construction. Different values of parameter a are used. The wider distribution corresponds to $a = \ell$. Every Voronoi construction consists of 10^4 polygons.

structed. The porosity of the samples is characterized by the void ratio $e = V_v/V_s$, with V_v the volume of voids and V_s the volume of solid grains. The shape of the anisotropic

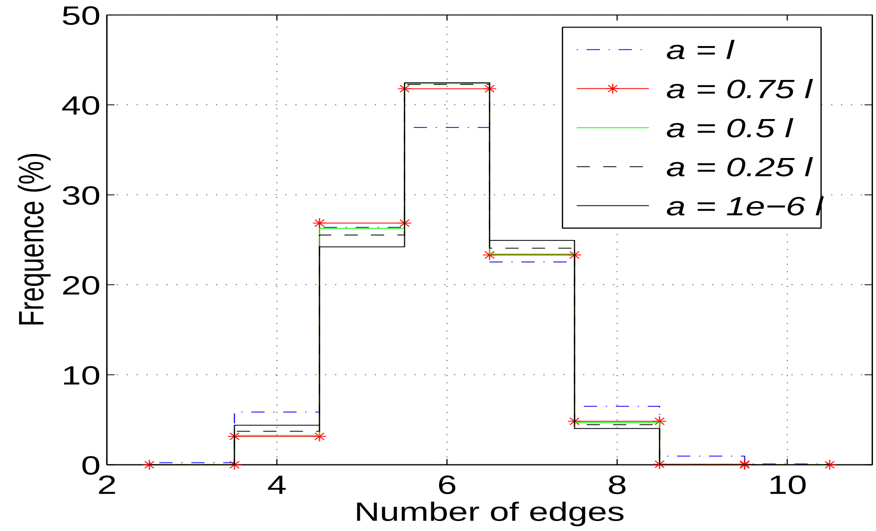

Figure 2.6: Distribution of number of edges of the polygons of the Voronoi constructions for different values of parameter a. Every Voronoi construction consists of 10^4 polygons.

particles is described by the aspect ratio λ, between the length of the longest and shortest axis of the particles.

First, in order to obtained different porosities the initial perfectly packed Voronoi polygons are moved apart to obtain a very loose state. This is accomplished by multiplying the coordinates of the polygons by a constant larger than one. Then, we use rigid walls as boundaries to compress the granular material. The sample is first compacted by applying a centripetal gravitational field to the particles and on the boundary walls, oriented to the center of mass of the assembly. After that, the sample is compressed isotropically using the four rigid walls until the desired confining pressure is reached. At this stage, the system is free to relax to its steady state. In order to generate dense samples, the interparticle friction is set to zero during the construction process. The loose samples are created taking damping coefficients 100 times larger than those used in the test stage.

Second, by stretching or contracting the reference square lattice used for the Voronoi construction in Sec. 2.4.1 particles with different aspect ratios λ are obtained. The dis-

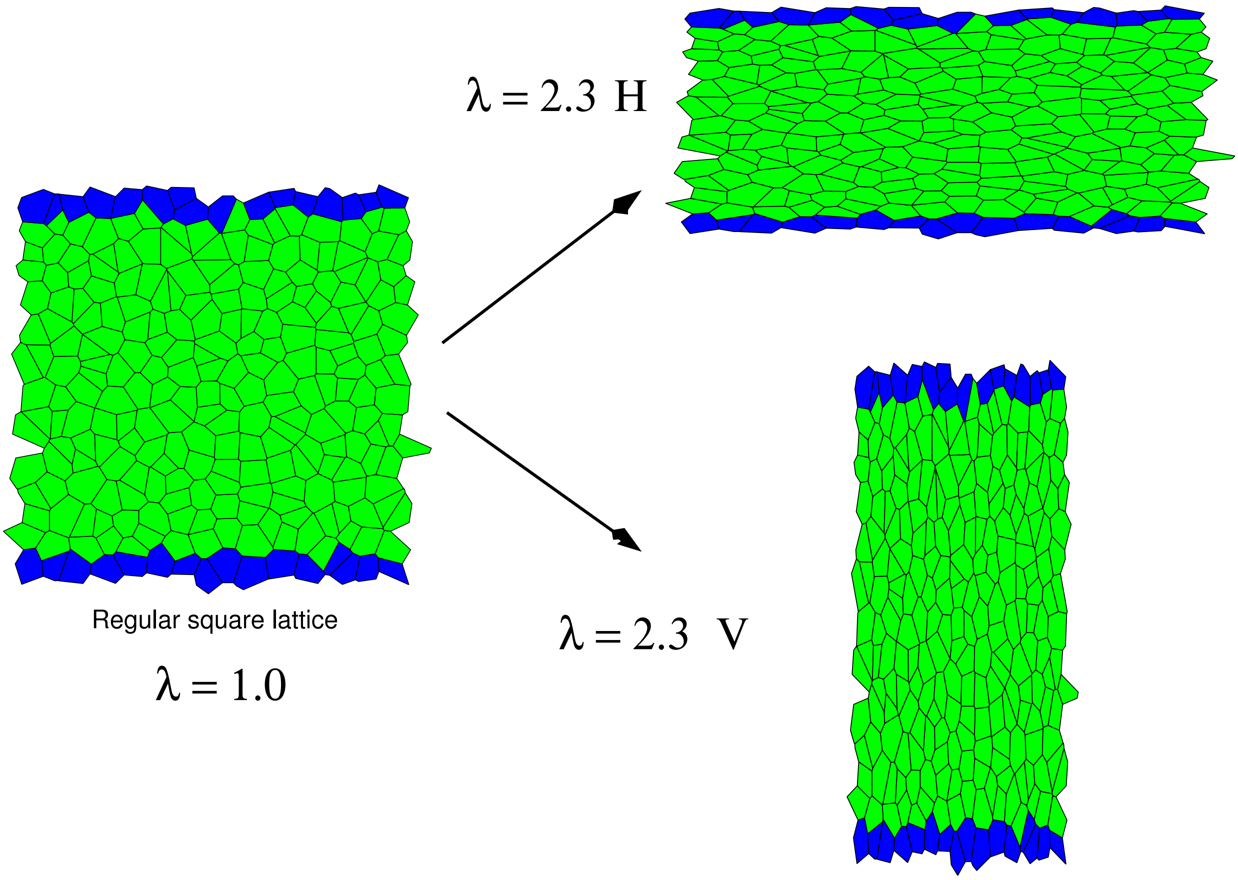

Figure 2.7: Distortion of the regular reference square lattice $\lambda = 1$ in order to generate samples with anisotropic particles $\lambda > 1.0$. Labels H (horizontal) and V (vertical) indicate the axis along which particles are initially stretched.

tortion of the square lattice is performed along the horizontal (H) or vertical (V) axis. In Fig. 2.7, the initial isotropic configuration λ = 1, and two distorted configurations are presented. The average elongation of the grains is given by the ratio between the stretching/contraction factors used to distort the lattice. In particular, the anisotropic samples presented in Fig. 2.7 have an aspect ratio λ = 2.3. The maximum value of λ used in this thesis is 4, chosen in order to avoid particles with very sharp angles that could have an unrealistic overlap. To generate porous samples with anisotropic particles the same procedure as explained above is used.

2.5 Neighbor search

The efficiency of the granular dynamics simulation is mainly determined by the method of contact detection. If the system consist of n particles, the required calculation operations for contact detection in each time step is $O(n^2)$ without any optimized algorithm. Special neighbor search algorithms such as Verlet Lists and Link Cell Algorithms [3, 56] have been proposed to reduce the computational effort.

Our method combines these two algorithms to determine the list of particles in potential contact using $O(n)$ calculations. The Verlet List contains the list of pair particles (i, j) which are relative close to each other. We then attach to each particle a *halo* of radius R, where R is the minimum radius of a sphere containing the particle. We call two particles *neighbors* if their halos touch or overlap.

At the same time, we use a Link Cell algorithm to allows a rapid calculation of this Verlet List: First, the space occupied by the particles is divided in cells of side D, where D is equal to the size ℓ of the reference square lattice used for the Voronoi construction (see Fig. 2.3). Then the Link Cell list is defined as the list of particles hosted in each cell. In the case of anisotropic particles, the link cells are also distorted similar to the case of the reference square lattice. Consequently, the candidates of neighbors for each particle are searched for isotropic particles only in the cell occupied by this particle, and in the 5×5 cluster around it excluding the corners. This search is based on the propability of potential neighbors of each cell on a vectorizable random lattice [93]. For anisotropic polygons, the search is increase to the 7×7 cluster around the host cell due to the fact that elongated shape increase the probability of finding additional neighbors.

2.6 Boundary conditions

2.6.1 Rigid walls

Walls are often used as boundaries to compact and load granular assemblies [34, 35, 96]. These walls can be either strain or stress controlled, i.e the velocity or the force applied on them is specified. The displacement of the walls and the total force on them can be used to determine the global stress and strain of the assembly. Boundary forces are applied on each grain in contact with these walls. The walls are frictionless, so they transmit only normal forces to the polygons in contact with them. When one of the vertices of a polygon penetrates one of the walls, a force, proportional to the penetration length δ, is applied on the polygon. This elastic boundary force $\vec{f}_n^b$ is oriented in normal direction $\hat{n}$ to the wall:

$$\vec{f}_n^b = -k_n \delta \hat{n} \tag{2.13}$$

Viscous forces $\vec{f}_v^b$ in wall-polygons interactions are also considered: $\vec{f}_v^b = -m_i \nu_n \vec{v}_n^c$, where m_i is the mass of the particle in contact with the boundary wall, ν_n the damping coefficient in normal direction, and $\vec{v}_n^c$ is the normal relative velocity of the vertex with respect to the wall. The boundary force is calculated for all the cases of interaction between walls and polygons in the same way.

2.6.2 Periodic boundaries

The periodic boundary technique is a very useful tool in granular dynamics simulations. Its main feature is the ability to remove the surface effects, which are presented in any finite sample. Therefore, it is a clever way to make a simulation consisting of only a few hundred particles behave as if it were infinite in size [56].

We use periodic boundaries to simulate extended shear zones. In this scenario, the periodic condition is imposed along the horizontal direction of our two-dimensional sample and is combined with fixed boundaries in vertical direction. This configuration is presented in Fig. 2.8. The top and bottom layers of the sample either undergo a constant

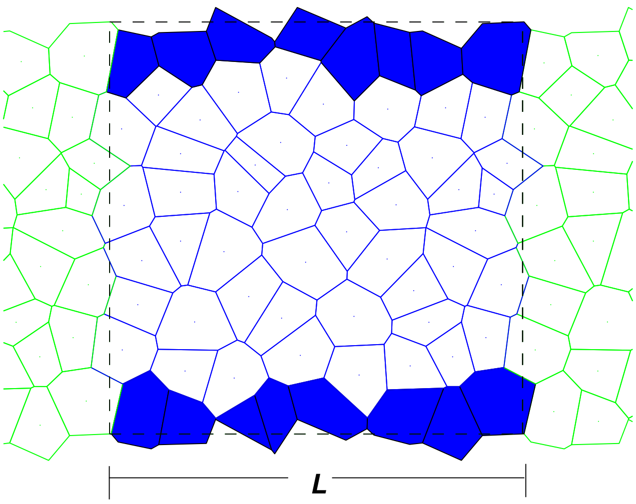

Figure 2.8: Sketch of the periodic boundary condition imposed in horizontal direction of the granular sample in order to mimic a shear zone. Light particles are the image used to implement the periodic boundary conditions. The black dash-line defines the space domain of the simulation. Dark layer of particles (blue in color) have fixed boundary conditions.

vertical force or are constrained to move in vertical direction. The periodic boundary condition is introduce as follows: particles are contained in a space domain of length L. When a particle leaves the left (right) side of this domain, it reenters from the opposite site. In each time step, particles in the left (right) side of the domain can interact with the particles in the right (left) side. This is implemented by wrapping the link cell in Section 2.5 as a doughnut, so that particles in the left (right) cells of the link cell can be neighbor of the particles in the right (left) ones. If a pair of particles are neighbors through the periodic boundary condition, their interaction is calculated in three steps: (1) shift the left (right) particle by L; (2) calculate the contact forces; and (3) shift the particle back.

2.7 Determination of the parameters

The whole set of parameters used in the molecular dynamics simulations are presented in Table 2.1. A suitable closed set of *material parameters* for this model is to chose the values for the ratios k_t/k_n and ϵ_t/ϵ_n, together with the value of the normal stiffness k_n and the interparticle friction μ. Since these parameters determine the mechanical response of the system, they should be adjusted to reproduce in reasonable agreement the main characteristics of realistic materials depending on the specific case under study [83, 84, 97].

The size of the Voronoi cells is defined in terms of ℓ as explained in Section 2.4.1. The value used in our simulations is 1 cm. The aspect ratio λ characterizes the anisotropy of particle shape. The density of the particle is taken 1 gr/cm^3, considering particles to be rods with a unit length of 1 cm in three dimensions.

Another important choice is the selection of the time step of the numerical simulation. It has to be done in order to maintain the stability of the numerical solution and improve the effectiveness of the computational time. The time step is usually determined in terms of the characteristic period of oscillation, specifically

$$t_s = 2\pi\sqrt{\frac{\langle m\rangle}{k_n}}, \tag{2.14}$$

where $\langle m\rangle$ is the smallest particle mass in the system. For a fifth order predictor-corrector integration scheme, it is usually accepted that a proper integration step should be in the range $\Delta t < t_s/10$ [56].

Alternatively, instead of considering a threshold referred to averages over the particles the integration step is extracted from local contact events [55, 57, 58]. Here, one usually considers only each pair of particles and defines the duration of a contact as

$$t_c = \frac{\pi}{\sqrt{\omega_0^2 - \eta^2}}. \tag{2.15}$$

Typically $t_c \simeq t_s/2$, and therefore in such cases, one also considers an admissible range of proper integration steps as $\Delta t < t_c/5$ [55, 87].

Symbol	Parameter
kn	normal contact stiffness
kt	tangential contact stiffness
μ	friction coefficient
ϵ_n	normal coefficient of restitution
ϵ_t	tangential coefficient of restitution
ν_n	normal coefficient of viscosity
ν_t	tangential coefficient of viscosity
ρ	density of the grains
ℓ	size of the cells of the Voronoi generation
λ	aspect ratio
Δt	time step for the MD simulation

Table 2.1: Parameters of the molecular dynamic simulation.

While performing shear and relaxation tests on granular packings, we find that the usual above thresholds for Δt are far from being conservative concerning the convergence of the solution of the numerical scheme. This non-convergence is directly related with problems arising from the calculation of the tangential contact forces explained in Sec. 2.2.2. Further discussion about the proper threshold to define the time step of the molecular dynamic simulations is hold in Chapter 6 of this thesis.

2.8 Additional definitions and remarks

In the next chapters of this thesis, the evolution of the local stress tensor, the fabric tensor and the inertia tensor of the isotropic and anisotropic samples will be used to follow the micro-mechanical evolution of the system. These key concepts will be required for the description of the media and are now introduced.

The fabric tensor $\mathbf{F}$ of second order characterizes the anisotropy of the contact network within the granular sample. The tensor $\mathbf{F}$ takes into account the distribution of the orientations of the contacts between particles, i.e. the geometrical structure of the medium [66]. For a single particle p its components F^p_{ij} are obtained from

$$F^p_{ij} = \sum_{c=1}^{C^p} l^c_i l^c_j \tag{2.16}$$

where the dyadic product of the vector $\vec{l^c}$ is summed over all the contacts C_p of particle p. The trace of the fabric tensor F^p_{ii} gives the number of contacts C_p of particle p. It is also possible to define a normalized fabric tensor F^p_{ij}/C_p, whose trace is unity. Finally, the mean fabric tensor for an assembly of particles is defined as:

$$\langle F_{ij} \rangle = \frac{1}{N_p} \sum_{p=1}^{N_p} F_{ij}^p \tag{2.17}$$

where the particle fabric tensor F_{ij}^p is summed over the total number of particles N_p within a representative volume element (RVE). The trace of this tensor is the local mean coordination number C_m, and therefore the normalized mean fabric tensor can also be defined as $\langle F_{ij} \rangle / C_m$.

The inertia tensor is calculated for each particle as follows:

$$I_{ij}^p = \int \rho(\delta_{ij} \sum_k x_k^2 - x_i x_j) dA \tag{2.18}$$

where ρ is the density of the particles, δ_{ij} is the Kronecker delta-symbol, k runs in our two-dimensional case from 1 to 2, dA is the differential area element, $x = \sqrt{x_1^2 + x_2^2}$ is the shortest distance from the rotation axis to dA, and $i, j = 1, 2$.

The mean inertia tensor follows from (2.18):

$$\langle I_{ij} \rangle = \frac{1}{N_p} \sum_{p=1}^{N_p} I_{ij}^p \tag{2.19}$$

where the particle inertia tensor I_{ij}^p is summed over the total number of particles N_p in the RVE.

The stress tensor for each particle is defined in terms of the contact force $\vec{f}^c$ between the grains (acting at the contact point c), and the branch vector $\vec{l}^c$ belonging to the contact point [98], namely

$$\sigma_{ij}^p = \frac{1}{V_p} \sum_{c=1}^{C_p} l_i^c f_j^c \tag{2.20}$$

where V_p is the volume of the particle p. In the same way, the global stress tensor of the assembly is calculated as follows:

$$\sigma_{ij} = \frac{1}{V} \sum_{c=1}^{N_c} l_i^c f_j^c \tag{2.21}$$

where V is the volume of the RVE, and the summatory extends over all the contacts N_c in the RVE.

We will also compute the principal directions (major M and minor m) of the mean fabric $\mathbf{F}$, inertia $\mathbf{I}$ and stress σ tensors. These principal directions are defined from their angle with the horizontal axis x of the absolute reference frame. We denote θ_F the angle corresponding to the major principal direction of the fabric tensor, θ_I the angle corresponding to the major principal direction of the inertia tensor and θ_σ the one of the stress tensor.

We are also interested in the individual orientation of non-isotropic particles. We symbolized by θ^p the angle formed by the major principal direction of the inertia tensor I_M^p of the particle p and the horizontal axis x. Notice that, θ^p gives the preferred orientation for each particle of the assembly.

In Fig. 2.9, a sketch of a particle and its surrounding neighbors in order to illustrate the calculation of the fabric, inertia and stress tensors is presented. The particle's contact network is plotted in Fig. 2.9a. Here the red lines represent the branch vectors $\vec{l}^c$. The principal axis of the tensors are depicted in Fig. 2.9b. In this particular case, the principal axis of the stress (red lines) and fabric (dashed blue lines) tensors are aligned. The principal axis of the inertia tensor are in green.

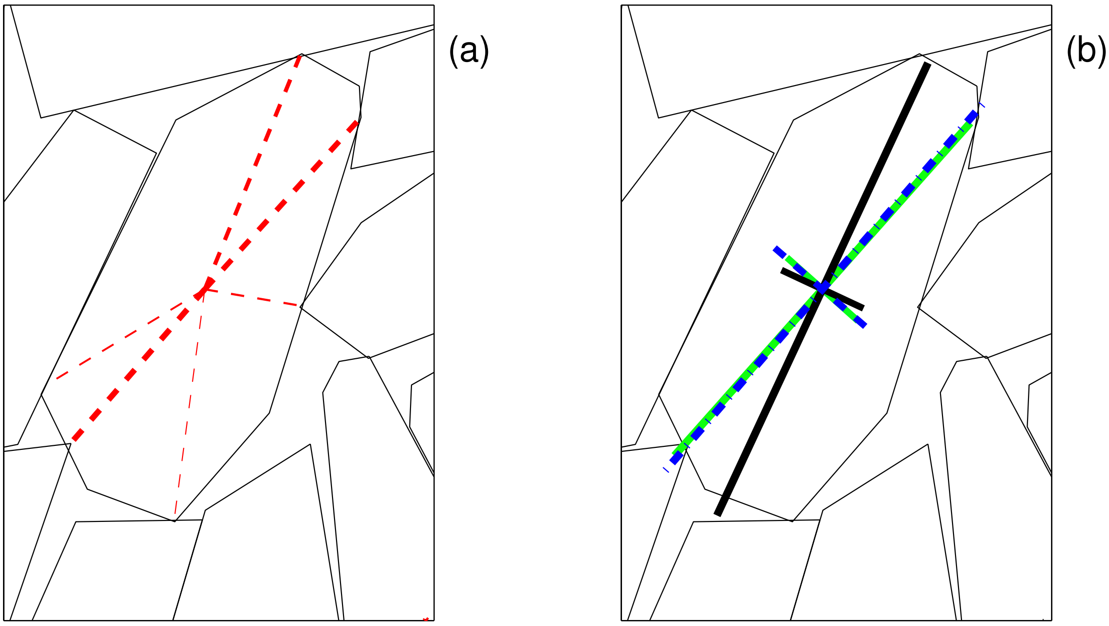

Figure 2.9: Illustration of the contact network and the fabric tensor, inertia tensor and stress tensor of a particle. (a) dashed lines are the branch vectors l^c, the width of the lines is proportional to the magnitude of the contact force, (b) Principal axis of $\mathbf{F}$ (dashed dark lines, blue in color), θ_I (solid dark lines, black in color) and θ_σ (solid light lines, green in color).

Chapter 3

Critical state, strain localization and stress fluctuations

The stress-strain behavior of dense and loose sand under shearing is described by Casagrande in 1936 [12]. He concludes that sand for large shear deformations independent of the initial density state reaches a limiting state (critical void radio) in which samples undergo unlimited deformation without further volumetric and stress increments. He also concludes that the critical void ratio is only dependent on the confining pressure, and thus determines the so-called critical state line relating the critical void ratio e_c and the effective normal stress σ' as applied on the shear box test.

The existence and uniqueness of this critical state is a major feature in soil mechanics since it is used to define post-failure behavior of many constitutive models describing granular materials. These models correspond not only to the family of elasto-plastic models [6, 11] but also to more recent alternative approaches like hypoplastic models [7–10]. The existence of a unique critical state has been experimentally proven to be independent of sample preparation and test conditions [15, 16]. Nevertheless, since there are some experimental difficulties to characterize the pre-and-post peak mechanical behavior of dense samples arising from the strain localization [11, 99]. There are some groups of researchers that claimed that the uniqueness of this state is still an open issue [18], and depends on the consolidation history of sand specimens [17].

In this chapter, we carry out biaxial test simulations of polygonal packing of particles, as a simple model of granular material as presented in Chapter 2. The existence of the critical state and the deformation patterns of the material under monotonic loading are investigated. Characteristic modes of deformation in granular material are rotation and rolling of particles [31–33], contact sliding [34, 35] and localization of strain in narrow *shear bands* [26, 36, 37]. Hence, we consider two different stages of the deformation of the granular media: (i) small deformation in order to study the first steps of strain localization and/or shear band formation and related micro-mechanisms [38], and (ii) large shear deformations in order to study the evolution of the granular packing toward the so-called critical state [39]. In the case (i), we find a strong correlation between contact sliding, grain rotation and strain accumulation. In the latter (ii), we show that the MD simulations of biaxial test reproduces the main features of the critical state in soil mechanics, namely, the granular media evolve toward a stationary state in which the system reaches a constant void ratio and deforms with constant volume and deviatoric stress, and that for different initial stress states the corresponding stationary values collapse onto a unique critical state line. Furthermore, at this stationary state, the dynamical response is characterized by fluctuations of stress and abrupt collapse of the number of sliding contacts. These stress fluctuations appear as a consequence of frictional instabilities. Experimentally, stress fluctuations have been observed in sheared glass bead samples [40], and packings of glass spheres under uniaxial compression [41] and axisymmetric stress condition [79]. Experimental biaxial tests performed on sand show evidence of *dynamic instabilities* at the critical state [80].

We also investigate the dependency of the overall response of the media on the interparticle friction and the system size. The results of stages (i) and (ii) of deformation are presented in Sec. 3.2 and 3.3, respectively.

3.1 Biaxial test simulations

In the field of soil mechanics, the occurrence and evolution of deformation patterns in granular materials is investigated systematically by means of laboratory tests [22]. In these experiments, a certain stress state is imposed on the sample by means of different boundary conditions, namely rigid plates and flexible membranes. The more commonly used experimental setup, is the axisymmetric triaxial test in which a flexible membrane maintains the sample together while imposing a hydrostatic pressure on the lateral direction, whereas two hard plates at the top and the bottom impose a certain axial strain or stress. However, to study the rheological behavior of granular materials the plane strain experiment is a very convenient test since it allows to determine the strain field at any stage of deformation [36, 99–101]. In this case, the sample is encased in a flexible membrane and confined between to parallel glass plates and two loading plattens, imposing plane strain conditions.

In our MD simulations the experimental setup, a two dimensional biaxial chamber with rigid walls see Fig. 3.1, mimics the strain plain test. Two types of experiments are performend: stress and strain controlled. The first one is used to explore the early stages of deformation, while the second one is employed to examine the steady state of the material since it allows one to observe both the hardening and softening behavior after peak of dense media [99].

In the tests the axial and lateral directions are indicated as 1 and 2, respectively. That is σ_1 and ε_1 are the axial stress and strain, and σ_2 and ε_2 are the lateral components. The strains are defined as follows:

$$\varepsilon_1 = \frac{L_1^0 - L_1(t)}{L_1^0}, \tag{3.1}$$

$$\varepsilon_2 = \frac{L_2^0 - L_2(t)}{L_2^0}, \tag{3.2}$$

where $L_1(t)$ and $L_2(t)$ are the dimensions of the system at the time t, and L_1^0 and L_2^0 the dimensions at the beginning of the test. Stresses have the same sign convention used in soil mechanics: compressive normal stresses are positive and tensile normal stresses are

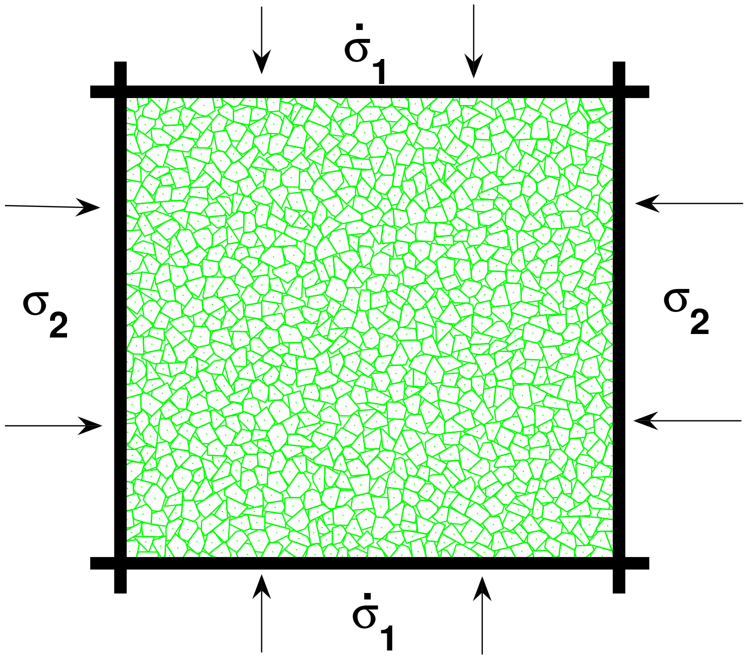

Figure 3.1: Biaxial cell. The stress state is imposed in the sample through four mobile walls. The lateral stress σ_2 is kept constant, while we increase the vertical stress σ_1 in a either stress controlled way, Eq. 3.4, or in a strain controlled manner $\dot{\varepsilon}_1 = const.$

negative. The deviatoric strain, γ, is defined in terms of the axial and lateral strains:

$$\gamma = \epsilon_1 - \epsilon_2. \tag{3.3}$$

In both tests, the pressure in lateral walls σ_2 is kept constant and equal to the initial isotropic confining pressure p_0. In the stress controlled test the axial stress σ_1 is slowly increased following the law:

$$\sigma_2 = p_0, \quad \sigma_1(t) = p_0\left[1 + \Delta\sigma \cdot f(t)\right]. \tag{3.4}$$

Different functions f(t) can be implemented. We have selected a very slowly varying function, given by:

$$f(t) = 0.5 \times \left(1 - \cos\left(\frac{2\pi t}{t_a}\right)\right), \tag{3.5}$$

where the period t_a considered is $t_a/\sqrt{k_n/\langle m\rangle} = 10^7$, being $\langle m\rangle$ the average mass of the particles in the system. The lateral walls can move, so that some strain accumulation is expected in the system.

In the strain controlled test, the horizontal walls (axial direction) are simply moved at constant rate $\dot{\varepsilon}_1$ inducing deviatoric stress.

The material parameters of the simulations are $k_n = 1.6 \cdot 10^8$ N/m, $\epsilon_n = 0.8$, and the ratios $k_t/k_n = 0.33$ and $\epsilon_t/\epsilon_n = 1.1$. The relatively low dissipation obtained with $\epsilon_n = 0.8$ allows us to reduce viscous effects during loading.

3.2 Small deformation stage

The main purpose of this section is the investigation and characterization of different factors influencing the first stage of deformation on granular packings, i.e. long before the material has either reached its peak strength or the steady state. This requires us to stay in the range of very small deformations [102]. We are interested in the existence of strain localization, and the idea is specifically to examine how the systems starts to deform in a biaxial test as the stress increases. The influence of the number of particles is investigated, for it is expected to be relevant in the formation of a shear band [37]. We use dense samples, different system size N, namely 400, 625, 900, 1600 and 3600 particles, and different interparticle friction coefficient μ.

According to previous work by Aström et al. [26], the succession of sliding and rotations of the particles in their shear experiments are related to the formation of some *bearings* in the shear band. Following these ideas, it is especially interesting for our purposes to monitor the evolution of the number of sliding contacts N_s and the mean rotation of the grains as the strain accumulates.

The time evolution of the relative number of sliding contacts $n_s = N_s/N_c$ being N_c the total number of contacts is shown in Figure 3.2. Here, three different system sizes are studied. In all the shown cases, the same kind of behavior is observed: The number of sliding contacts increases in time, but this evolution is interrupted from time to time by some events, in which the number of sliding contacts decays abruptly. The recurrence of this phenomenon has been checked for different time steps of the simulation and also for different functions $f(t)$ (as described in Eq. 3.5). In some of these drop-offs, all the contacts stop sliding, whereas in others the number of sliding contacts is considerably

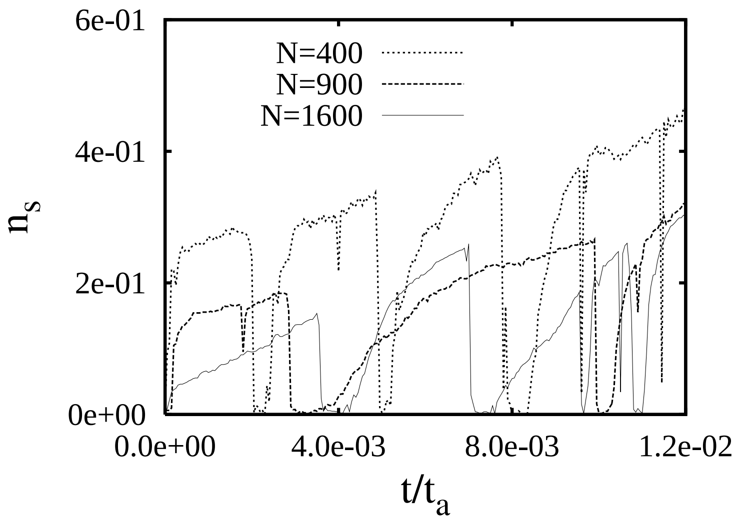

Figure 3.2: Results of the simulation of a system of polygons with $\mu = 0.25$ and different number of particles 400, 900 and 1600. The relative number of sliding contacts n_s is plotted against time.

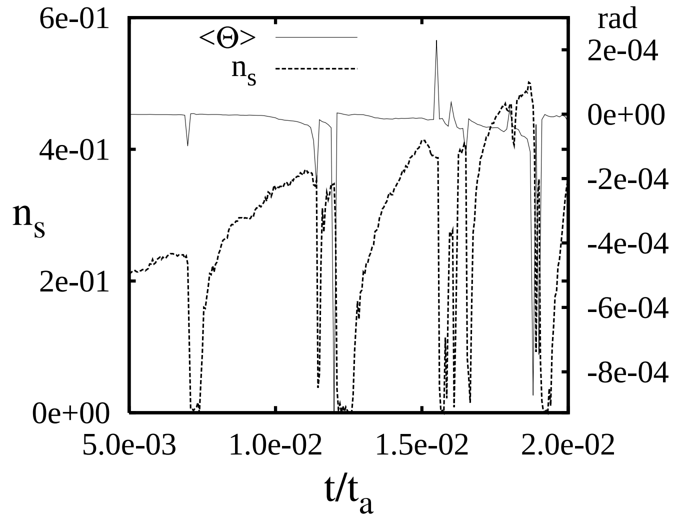

Figure 3.3: Evolution of the relative number of sliding contacts n_s and the mean angle $\langle\Theta\rangle$ through which the particles have rotated. The simulation details are $\mu = 0.25$ and $N = 400$.

reduced, but remains bigger than zero. In more detail, the sequence is the following: At the beginning, the number of sliding contacts grows steadily as the stress increases. Above a certain value, there is a sudden decrease on n_s. After this change, the number of sliding contacts remains low for a while before starting again to increase in time. In

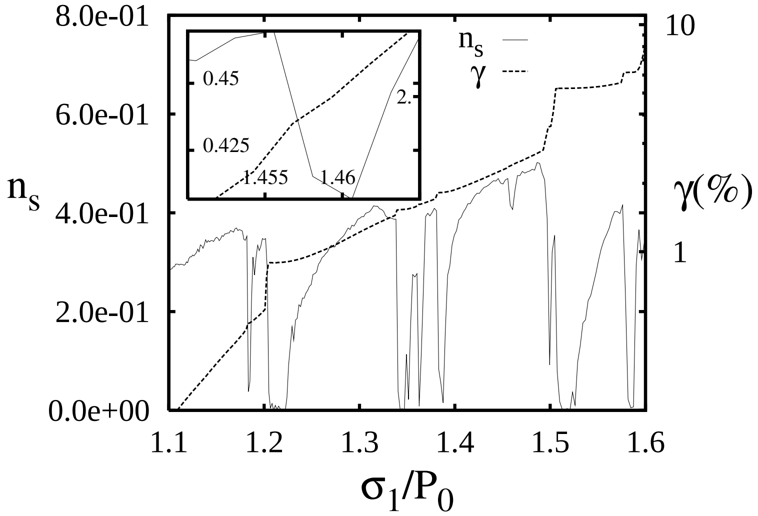

Figure 3.4: Correlation between the behavior of n_s and the strain accumulation. The inset shows in detail that also smaller drop-offs are related to a change in the evolution of γ. The simulation details are $\mu = 0.25$ and $N = 400$.

this new stage, the number of sliding contacts can grow beyond the value previous to the collapse. Observe that the frequency with which these abrupt changes in n_s occur increases as the experiment continues. Note also that the time at which the first event occurs is later for bigger systems. It is also observed that the cases in which there is a partial decay of n_s, the value of sliding contacts remains low for a shorter period of time than in the drop-offs where n_s decays to zero.

Figure 3.3 shows the relationship between sliding and the rotations for the system size $N = 400$ presented in Fig. 3.2. During the experiment, each grain rotates a certain angle $\theta_i(t)$. We have calculated the mean angle rotated by the grains at a certain time $\langle\Theta(t)\rangle$. This average rotation is plotted on the secondary y axes of Figure 3.3, while on the primary axes we show the time evolution of the relative number of sliding contacts at the same point of the experiment. The strong changes in n_s described in the previous paragraphs correlate very well with a strong increase of the rotations of the system. Figure 3.3 clearly indicates a strong correlation between the collapse on n_s sliding, and the rotation of the grains. One can also observe that there is no preferential direction of rotation.

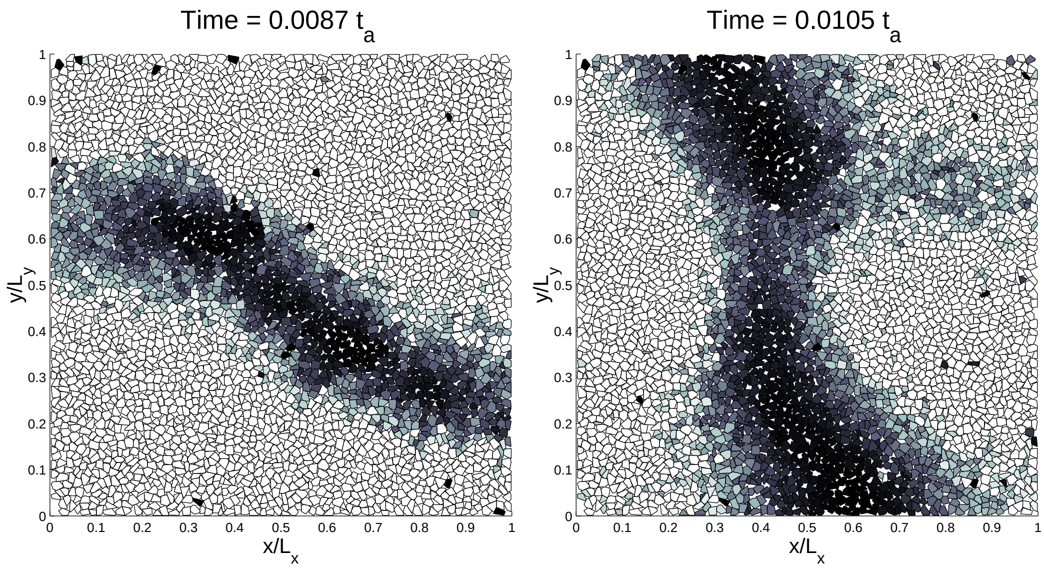

Figure 3.5: The kinetic energy of the grains is plotted here in two snap-shots of the simulation, just before (left) and right after a collapse (right).The gray scale is proportional to the kinetic energy of the grains in the sample. The scales in the left and right graphs are different, but in both of them the darker grains move slower. Some localization of the kinetic energy can be identified before the collapse, whereas after the jump in the strain, the shear band has disappeared and the grains move faster following walls displacement (the average kinetic energy after collapse increases about one order of magnitude). The results correspond to the simulation of a system with $N = 3600$ polygons and $\mu = 0.1$.

In Figure 3.4 we want to stress the relationship between the behavior of the sliding contacts and the strain accumulation γ. We observe a direct relationship between the increase of γ and the decay in n_s, which is more evident for the strongest decays, but is also observed in the smaller collapses (see the inset of Fig. 3.4). Between collapses, as n_s is increasing, γ grows almost linearly with the stress.

The results shown in Figures 3.3 and 3.4 indicate the following picture of what is happening in the system. As the stress slowly increases, the system does not change appreciably its spatial configuration. At this point there is not creation or destruction of contacts. The changes of strain occur in the existing contacts: some of them start to slide, while the contacts that are already sliding continue sliding. This situation correspond to a steady increase of the strain γ. It is important to remember that our boundary conditions are fully mobile hard walls. The small change in the strain is due to tiny changes in the position of these walls, caused by the sliding of the system. This small deformation-rate stage leads at some point to a rearrangement of the system which suddenly causes a rapid movement of the walls (namely, the sudden jumps of γ). In this new situation, the system undergoes, from one time to the next, a stress relaxation in which the grains can move and rotate, and the contacts are removed from the sliding condition. In the new configuration, the process starts again, the existing contacts start sliding and the system

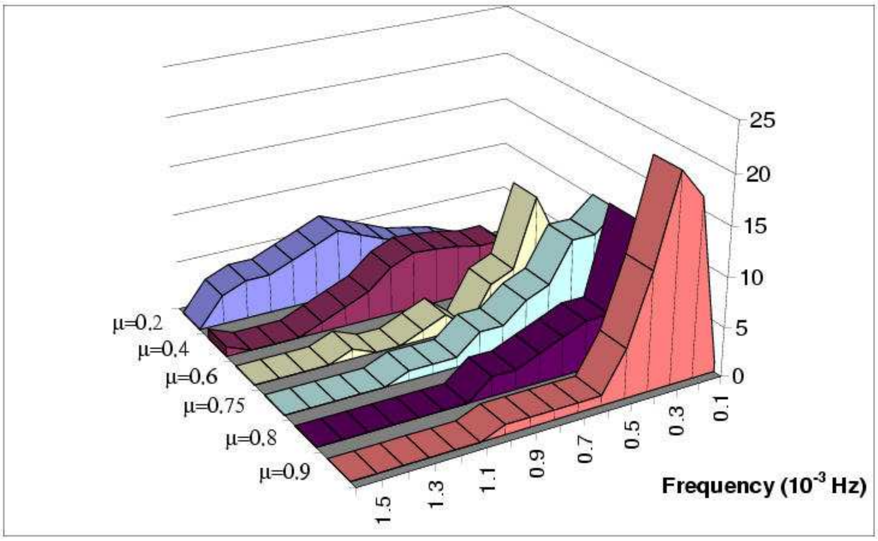

Figure 3.6: Histogram of the frequency of occurrence of the collapses, measured through the waiting time for the drop-offs in the relative number of sliding contacts. Each of the histograms corresponds to a different μ. The simulations correspond to a system size $N = 625$ particles.

accounts for small deformations due to this sliding. This will lead to a new configurational change, and the process will begin again. The system gets more dense after each of this collapses, which agrees well with the observed fact that the maximum value that the number of sliding contacts before a new drop-off increases event by event.

Concerning strain localization, in none of our experiments (with systems up to 3600 polygons) a clear and lasting shear band was observed. There are, however, some stages of the test in which a shear band seems to appear, see Figure 3.5, but it is very unstable and it quickly disappears as soon as one of the drop-offs on n_s occur.

Finally, we address the influence of the interparticle friction μ on the frequency of abrupt changes of n_s. Thus, we measure the waiting times between every consecutive decay of n_s and based on these results we calculate the histograms of the frequency of occurrence of the collapses. The histogram is presented in Figure 3.6, here one can see the existence of a characteristic frequency for each friction coefficient. This is more clearly observed in the more frictional samples, since the distribution function of the frequencies narrows as friction grows. At the same time, the mode of the distribution moves towards the origin i.e. the events become less frequent. Figure 3.7 shows the characteristic frequency of collapse occurrence for different friction coefficients. It clearly decreases as the friction coefficient grows up to a certain value around $\mu = 0.6$. Above this friction, the most probable frequency seems to be independent of μ.

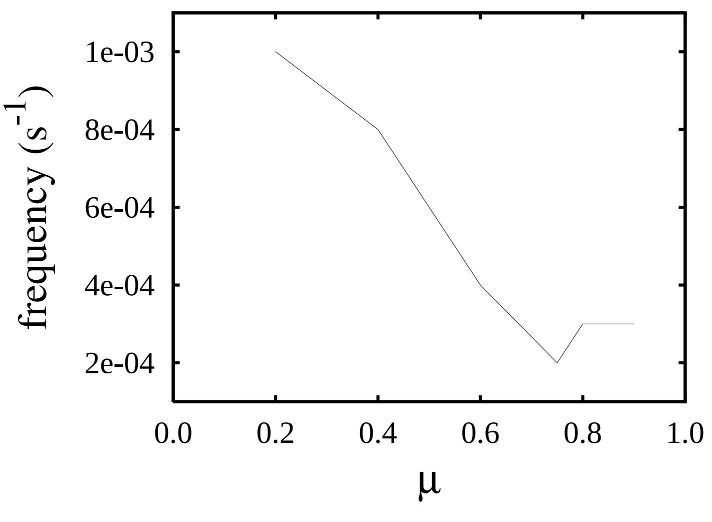

Figure 3.7: Dependence of the characteristic frequency of occurrence of the drop-offs on n_s with friction. The simulations correspond to a system size $N = 625$ particles.

3.3 Large deformation stage - critical state

3.3.1 Critical state

In order to assess the existence of the critical state on granular packings, we first explore the macro-mechanical evolution of granular samples under large shear deformations. The experimental procedure is explained in Sec. 3.1. The experiments are performed over different initial conditions, namely, (i) three different samples each one corresponding to a different seed used in the random generation of polygons and therefore with differences in particle's distribution, Sec. 2.4.1 and (ii) different initial density states. We characterize the density of the samples by the void ratio e, as defined in Sec. 2.4.2. The samples we use in this analysis are constructed with an initial isotropic confining pressure $p_0 = 64$ kN/m, have system size $N = 900$ particles, and the interparticle friction coefficient is $\mu = 0.5$. The corresponding initial void ratios of the dense and loose samples are presented in Table 3.1. Figure 3.8 presents the sample configuration at the end of the construction process, for both dense and loose media.

Table 3.1: Initial void ratio of the samples used to evaluate the critical state.

Sample	Dense state	Loose state
1	0.145	0.270
2	0.144	0.266
3	0.146	0.278

In Figure 3.9(a) the evolution of $\sin\phi = (\sigma_1 - \sigma_2)/(\sigma_1 + \sigma_2)$ with axial strain ε_1 for the dense and loose samples is presented. In general, the dense samples exhibit a higher initial stiffness than the loose ones. After the peak in the dense media, which is about

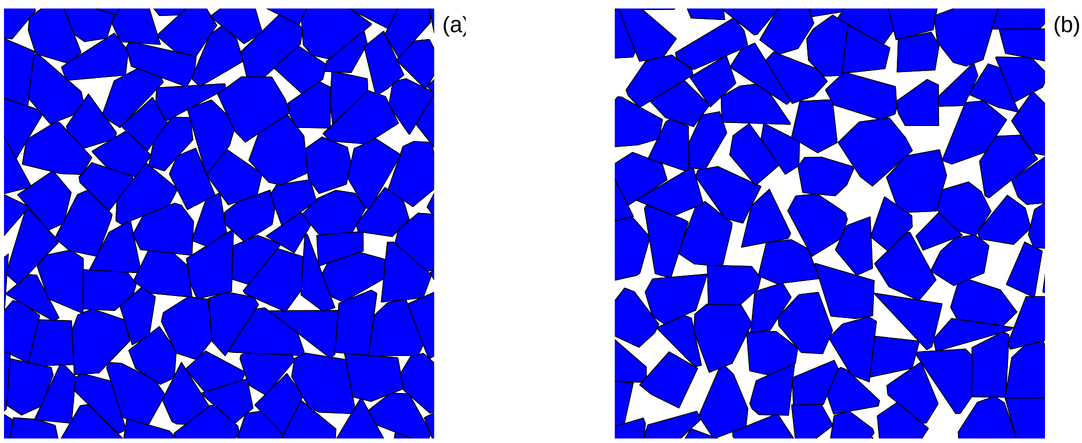

Figure 3.8: Sample configuration at the end of the construction process: (a) dense and (b) loose media.

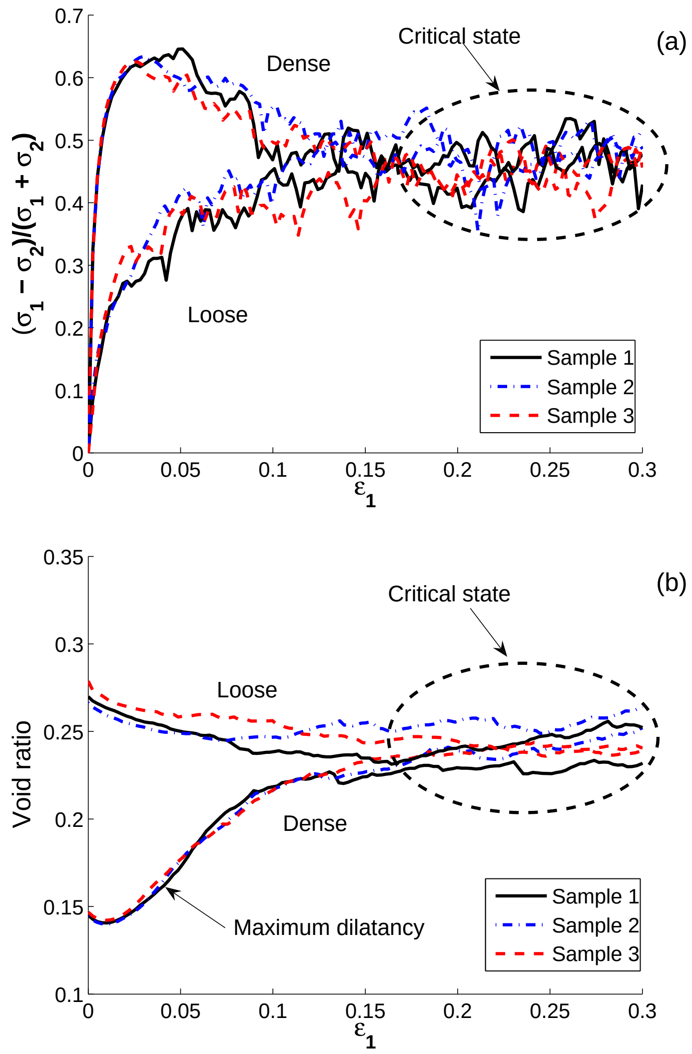

Figure 3.9: Evolution of (a) the deviator stress and (b) void ratio of the samples used to asses the existence of the critical state. Simulation parameters, $p_0 = 64$ kN/m, $N = 900$ particles and $\mu = 0.5$.

5% axial strain, a strain-softening behavior is observed. The loose media exhibit more frequent and bigger variations in the stress behavior. Additionally, a peak strength is not observed. Although an increase of fluctuations of the stress are observed for both systems at large deformations, it presents a tendency to stabilize around a value that one could consider as the steady state of the material ($d\dot{sin\phi}/dt = 0$). The evolution of the void ratio with axial strain is illustrated in Figure 3.9(b). Initially, the dense samples contract and later the void ratio increases (dilatancy). For large axial strain values the void ratio reaches a constant value. Comparing the evolution of dense samples in Figure 3.9(a) and (b) we notice that the maximum rate of dilatancy agrees with the peak strength

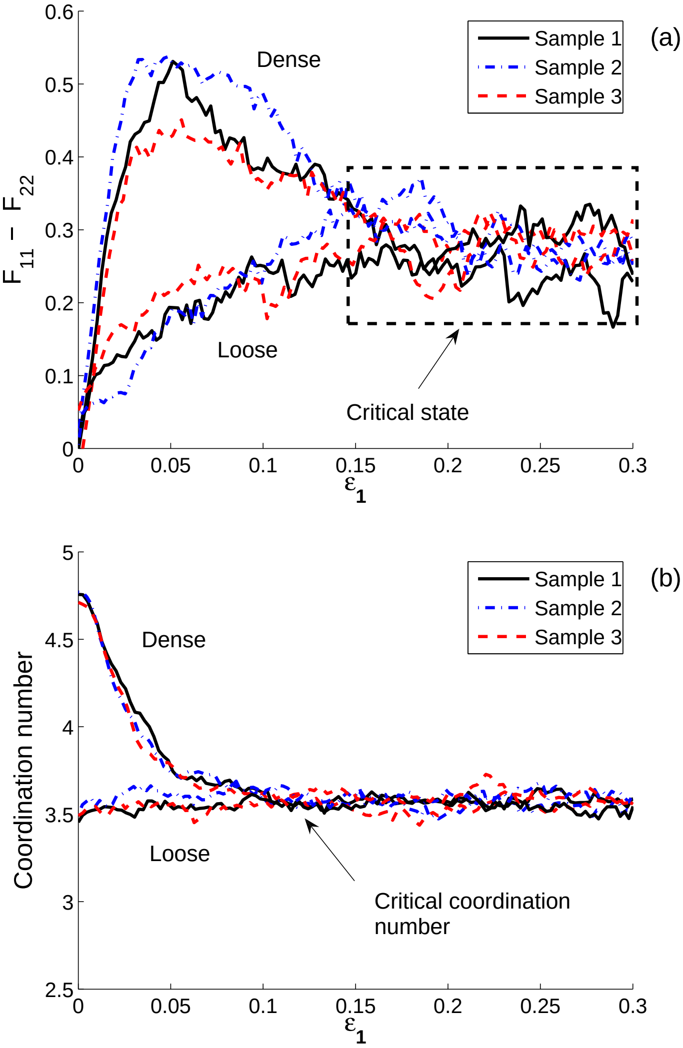

Figure 3.10: Evolution of (a) the deviatoric component $F_{11} - F_{22}$ and (b) the trace $F_{11} + F_{22}$ (coordination number) of the fabric tensor of the samples. Simulation parameters, $p_0 = 64$ kN/m, $N = 900$ particles and $\mu = 0.5$.

($\approx 5\%$ axial strain) which is expected on soils. It is especially observed in samples 1 and 2. The loose samples reduce their void ratio during the test (Fig. 3.9(b)), and it tends to a constant ratio near to 20% axial strain. The void ratio in both dense and loose samples varies until it achieves a constant value between 0.23 and 0.25. This stationary value of e is slightly different for each sample, since the parameters e and ϕ at this stationary state depend on the granulometric properties of the material [22, 71]. In this stage of large deformations, the granular medium is deformed at constant volume and with the same approximate value of deviator stress, which corresponds to the critical state of the material and it is independent of the initial sample density [6]. All these features reproduce the asymptotic behavior of soils obtained in laboratory experiments [11]. Thus, the existence of the critical state is validated in our numerical simulations.

Another issue we address is the evolution of the structural anisotropy or anisotropy of the contact network of the granular packing [66, 67]. It is characterized using the deviatoric component of the fabric tensor $\mathbf{F}$ defined in Sec. 2.8, and takes into account the orientational distribution of contact normal vectors $\vec{n}$. In Figure 3.10a the evolution of the deviatoric component $F_{11} - F_{22}$ of the fabric tensor with ε_1 for the three reference samples is presented. One can notice that the contact network start from a rather initial isotropic configuration $F_{11} - F_{22} \approx \;\; 0$, and that as soon as the shear proccess begins anisotropy is developed. This anisotropy is created due to creation and reorientation of contacts and force chains along the direction of loading. For dense samples, the anisotropy increases until the granular system develops its peak strength i.e. the maximum anisotropy coincides with the maximum strength ($\approx$ 5 % axial strain ε_1). On the other hand, the anisotropy in loose samples simply increases until it saturates at a constant value between the statistical fluctuations. In the strain-softening regime the anisotropy of dense samples decreases until it converges to the same value that the loose samples have reached. Hereafter, the media deforms at a critical anisotropy. This has been previously observed in numerical simulations of biaxial tests with the DEM [76, 103, 104].

The creation and destruction of contacts can be studied by following the coordination number Z, which is defined as the average of the number of contacts per particle on the assembly. As defined in Sec. 2.8, the trace of $\mathbf{F}$ gives the coordination number. In Figure 3.10b the evolution of the coordination number of the samples is presented. At low axial strain values, the dense system contracts and as a consequence a small increment of Z is observed. This is followed by a decrease of the Z value when the system start to dilate. This decrease is associated with the the breaking of interlocking between particles and the related formation and collapse of force chains along the direction of loading. As a result, each particle begins to lose contacts. This is macro-mechanically observed by the trend of dense samples to increase their volume. In contrast, the loose granular sample tends to a denser structure, and therefore new contacts are generated. Both samples around 8% axial strain reach a similar coordination number Z close to 3.6. This critical coordination number is the first signal that the granular packing is evolving towards the critical state, and at the same time it enables the contact network to reach an steady structure. Thus, the micro-mechanical requirements for the granular media to reach the critical state at the macro-mechanical level are given. At the critical coordination number the media is highly susceptible to collapse, and as consequence fluctuations mainly on the stress Fig. 3.9a are observed. These fluctuation are studied in Sec. 3.3.4.

We want also to evaluate the uniqueness of this stationary state, specifically, that there is a unique void ratio for each state of effective stress at the critical state. Hence, we perform biaxial experiments on one of the samples above mentioned and use different initial confining pressures p_0, namely, 16 kN/m, 64 kN/m, 128 kN/m, 160 kN/m, 256 kN/m and 320 kN/m. We remain in the low stress level, where dense samples still expand and exhibit a peak on the stress behavior [11]. High stress levels are not considered since crushing of particles is the expected to be the primary mechanism of deformation

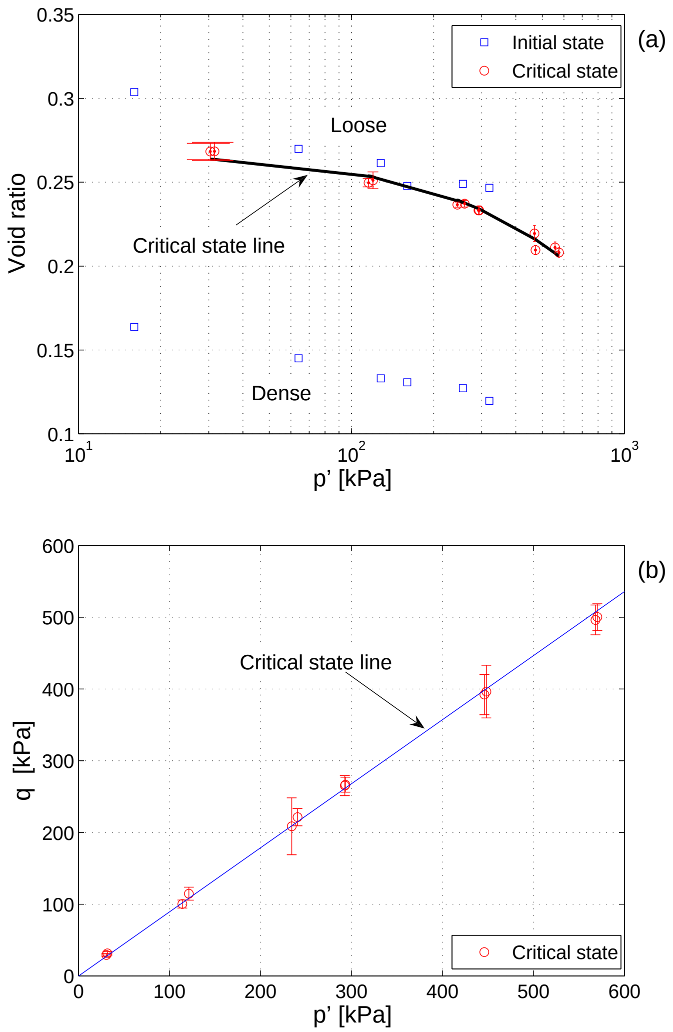

Figure 3.11: Critical state line in the (a) compression plane void ratio e - mean stress p' and (b) and stress plane q - p'. System parameters, $N = 900$ particles and $\mu = 0.5$. In (a) the squares indicate the initial state of the samples. In (a) and (b) the circles are the values that samples reach at the stationary state, and the error bars correspond to 1 standard deviation of the analyzed data.

and our model does not take this feature into account.

In Figure 3.11a, we plot in the compression plane, void ratio e - mean stress p' ($p' = (\sigma_1 + \sigma_2)/2$), the initial states of the samples (blue squares) and the values of void ratio that the loose and dense samples attain at large deformation (red circles). One can see that the same limit state is reached for all the samples defining a unique steady state line. This line can be fitted by a function of the form,

$$e(e_{ref}, n) = e_{ref}\ exp(-n\ (p'/p'_{ref})), \tag{3.6}$$

where e_{ref} and p'_{ref} are the void ratio and the mean stress at the critical state corresponding to the reference initial confining pressure $p_{0,ref} = 16$ kN/m, and n is a constant. The same collapse of the stresses at the critical state (red circles) onto a steady state line is observed in Fig. 3.11b, in which the stress plain $q - p'$, being $q = (\sigma_1 - \sigma_2)$ is depicted. The stress ratio q/p' at the critical state defines the strength parameter M, which for our simulations is related to the critical state friction angle ϕ_{cs} as,

$$M = \frac{q_{cs}}{p'_{cs}} = 2\ sin\phi_{cs}\ . \tag{3.7}$$

The range of variation of the friction angle at the critical state $22° \leq \phi_{cs} \leq 27°$ found in our simulations (Sec. 3.3.3), is compared to the limits usually obtained for sand and gravel in three dimensional experiments in realistic soils $26°$ to $36°$ [16, 22]. This is explained in terms of the higher coordination number of systems in 3D [30], and the higher the coordination number the higher the strength of the material as presented in Figs. 3.9a and 3.10c.

The previous simulation results support the idea of uniqueness of the critical state [6, 11], in which a critical or steady state line links the critical states describing combinations of effective stresses and void ratio $e : q : p'$ at which indefinite shearing occurs. This is also in very good agreement with the experimental results of Verdugo et al. [16].

Finally, we evaluate the critical anisotropy for different stress sates, and we find that a critical state line for anisotropy can also be defined as presented in Fig. 3.12. The relation between structural anisotropy and mean stress p' is best fitted by a linear function. Further analysis concerning induced anisotropy in sheared granular media is carried out in Chapter 4 of this thesis.

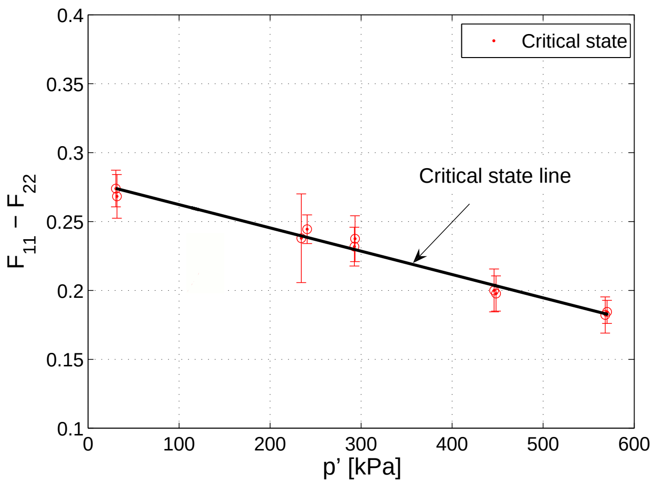

Figure 3.12: Critical state line in the plane deviatoric fabric $(F_{11} - F_{22})$ - mean stress p'. The circles are the values that samples reach at the stationary state. The error bars correspond to 1 standard deviation of the analyzed data. Simulation parameters $N = 900$ particles and $\mu = 0.5$.

3.3.2 Shear bands

Strain localization has been experimentally studied by several researchers in the last two decades, e.g. Vardoulakis [105], Desrues [36] and others. Using the discrete element method Cundall [106], and Bardet and Proubet [107] have also studied this phenomenon. In this section a brief analysis of strain localization is performed by studying the displacement of the individual particles. In Figures 3.13 the displacement vectors of the particles of a dense assembly, with $p_0 = 160$ kN/m, $N = 400$ particles and $\mu = 0.5$, are presented. At the beginning of the test, the displacements are very small and one can observe approximately a symmetrical deformation around the center of the sample (Fig. 3.13(a)). As the axial strain increases and before the peak strength is reached a slight tendency to strain localization is observed. After having overcome the peak strength, the particle displacements seem to define independent bodies with different displacement directions (a clearer strain localization). This localization persists as the loading increases, and becomes clearer around 8.9 % axial strain (Fig. 3.13(b)), where two "shear bands" are observed. After peak, these shear bands are not constant in time. In fact, there are stages in which clear shear bands are observed, but they typically disappear, leading to a stress falloff. These falloffs, as we will see in Section 3.3.4, are related to force

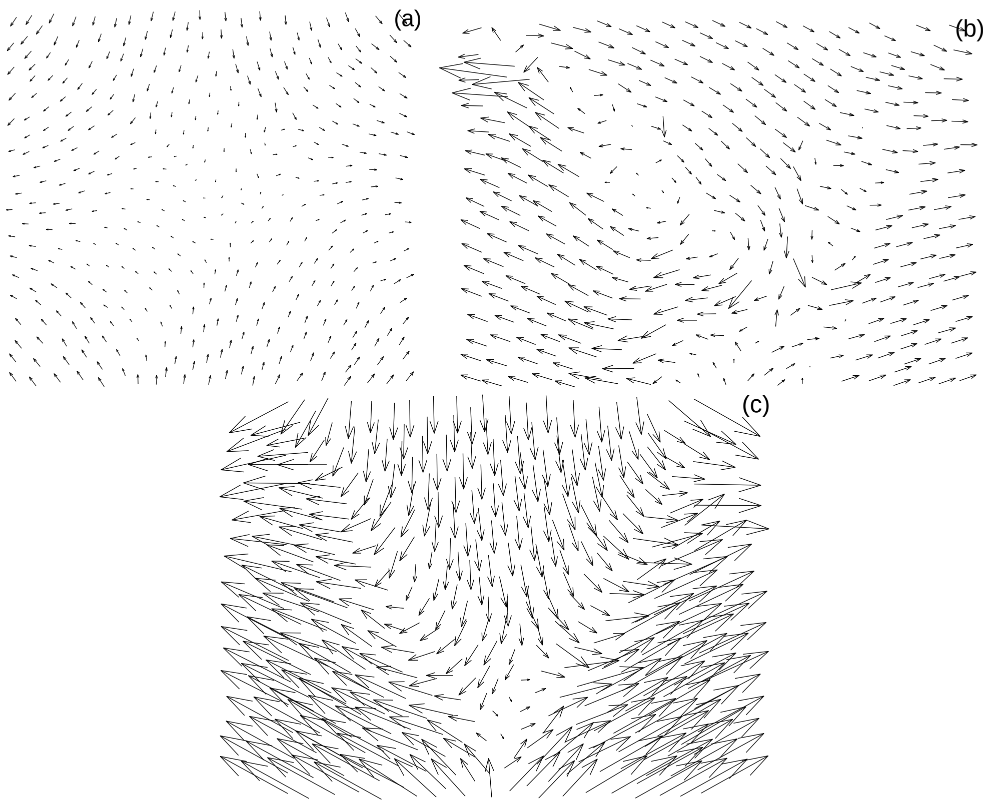

Figure 3.13: Displacement of particle centers within a dense sample at three axial strains values (a) 1.2 %, (b) 8.9% and (c) 20% of total.

chains collapse and therefore to rearrangements of the media that hinder the persistence of the shear bands. The particle displacements of Figures 3.13(a) and (b) are taken from two consecutive time intervals, which correspond to an increment of 0.1 % of axial strain. Figure 3.13(c) presents the displacement at 20 % axial strain measured from the particle initial position. Here three bodies with different direction of displacement, and the areas (shear bands) defined between them are visible.

Concerning shear band orientation, experimental data from biaxial tests on sand indicate that this orientation varies between the Mohr-Coulomb solution $\theta_C = 45° + \phi/2$, where ϕ is the angle of friction of the material, and the Roscoe Solution $\theta_R = 45° + \Psi/2$ [108], where Ψ is the angle of dilatancy. The dilatancy angle is defined as $\Psi = \arcsin(d\epsilon_V/d\gamma)$, where $d\epsilon_V$ and $d\epsilon_\gamma$ are the increments of volumetric and deviatoric strains at failure [109]. We calculate the inclination angle of the shear bands in Figure 3.13(c), and it varies approximately between $52°$ and $58°$. In this case, for ϕ_{micro} = $28.8°$, we can obtained from Fig. 3.15 the values of $\phi_{cs} \approx 26°$ and $\Psi \approx 0°$ at the critical state. In this way, the angles found in our simulation are within the limits defined by the predictions of the Mohr-Coulomb solution $\theta_C \approx 58°$ and Roscoe Solution $\theta_R \approx 45°$.

Although the particle displacements of loose samples are not shown, their evolution reflects the frequent force chains collapses and consequent rearrangement of the particles within the sample. This is observed on the large displacements of the particles which are associated with the drops of the stress-strain behavior. Strain localization is not clear in loose media.

3.3.3 Macroscopic friction

An approach to connect the Coulomb friction at the grain level to the macro-mechanical friction is to construct the Mohr-Coulomb failure surface of the granular sample. This failure surface can be obtained from the envelope of the Mohr circles at the peak stress value from biaxial tests [108]. The tests were carried out on dense samples, at three confining pressures: 80, 160 and 320 kN/m. Different methods are used to describe the failure surface of granular soils. In the following analysis, as used in traditional soil mechanics, we assumed that the failure surface is linear. Figure 3.14 shows the failure envelope of a granular sample with interparticle friction coefficient μ = 0.55 that corresponds to an interparticle friction angle ϕ_{micro} of $28.8°$ (μ = tan ϕ). The envelope is plotted as a tangent straight line to the Mohr circles, and the angle of friction of the bulk material is approximately $41°$. In our simulations, the macroscopic angle of friction was found to be independent of system sizes varying from 100 to 3600 particles. Simulations of much larger number of particles were not performed, since they are limited by the architecture of the program, which requires static storage allocation for all variables.

If we compare this result with the one obtained by Bardet using DEM with disks [31], we can then observe the important influence of particle angularity on the friction angle ϕ_{peak} of the medium. For instance, using very similar values of ϕ_{micro}, $28.8°$ for polygons and $26.5°$ for disks, the obtained values of ϕ_{peak} are $41°$ and $22°$ respectively. The ratio ϕ_{peak}/ϕ_{micro} is then equal to 1.42 for polygons and 0.83 for disks. Furthermore, as

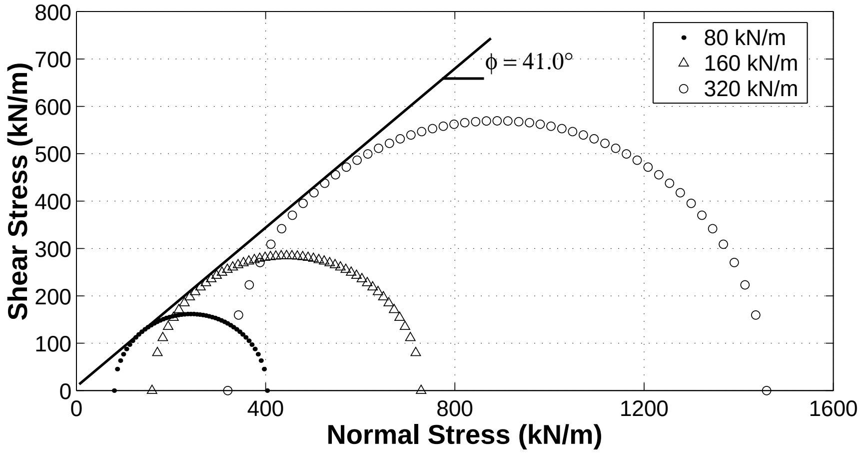

Figure 3.14: Mohr-Coulomb failure envelope constructed from biaxial test and Mohr circles. Interparticle friction angle ϕ_{micro} = $28.8°$, and $N = 400$ particles.

mentioned in the previous Section, different macro-mechanical angles are correlated to different orientation of the shear band, and therefore different localization patterns are expected. In the case of disks, if particle rotation is constrained, as in Ref. [31], a value of ϕ_{peak} = $41°$ is obtained. In such case, although ϕ_{peak} is equal to the value for polygons, the sample dilatancy is almost completely hindered and therefore the stress-strain behavior of the sample is highly affected. For example, no correlation between peak strength and maximum rate of dilatancy is observed. All these observations confirm the important role of particle shape, related to angularity, on the global behavior of granular media.

In order to study the effect of the interparticle friction ϕ_{micro} on the macro-mechanical friction angle ϕ_{macro}, different interparticle friction coefficients and five different samples with system size $N = 400$ were used in the simulations. Additional to the friction angle at the peak stress ϕ_{peak}, the friction angle at the critical state ϕ_{cs} was also calculated. Figure 3.15 shows for the five samples the values of ϕ_{peak} and ϕ_{cs} obtained from variations of ϕ_{micro}. It is observed that at very low values of ϕ_{micro} the macro-mechanical angles are quite similar. For values of interparticle friction angle larger than $15°$ the granular samples develop a clear peak strength ϕ_{peak} (value different from ϕ_{cs}), while the ϕ_{cs} value remains approximately constant. The last agrees with the experimental results obtained by Skinner [110], except for the results from micro-mechanical angle close to zero. These results suggest that, except at small values of ϕ_{micro} where other mechanisms different from friction play the important role, the friction angle mobilized at the critical state ϕ_{cs} is independent of the interparticle friction coefficient. This particular feature has been also observed in numerical simulations with circular particles [42]. The non-dependence of macroscopic friction on contact friction is attributed to the spontaneous formation of rotational patterns, such as the vorticity field shown in the Part (b) of Figure 3.13, and clusters of particles with intense rolling. Those deformation modes have shown to re-

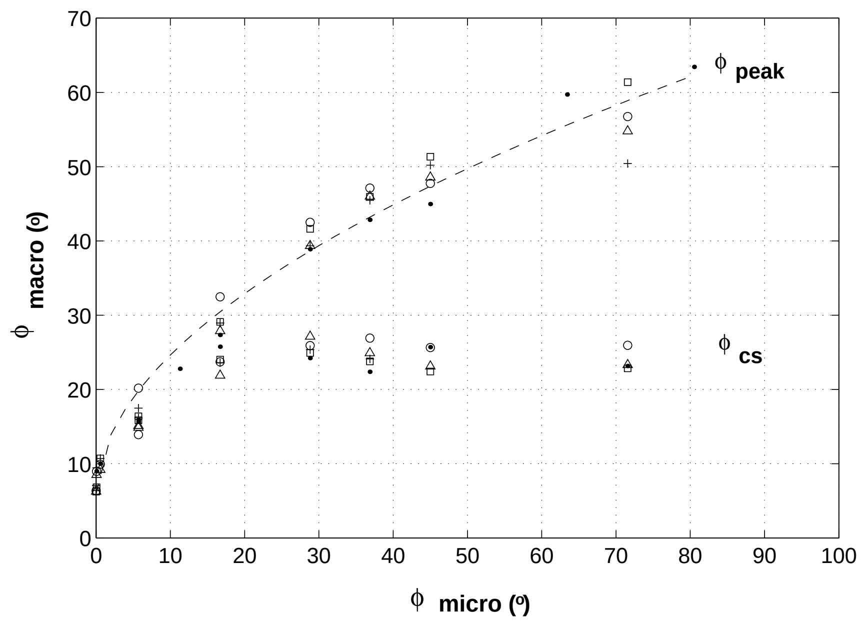

Figure 3.15: Evolution of the macro-mechanical friction angle at peak strength ϕ_{peak} and at the critical state ϕ_{cs}. The dashed line is a power law approximation $\phi_{peak} = 5.5 \cdot \phi_{micro}^{0.53} + 6$. System size $N = 400$ particles.

duce considerably the bulk friction with respect to the expected value of the simple shear deformation [42].

Note that setting ϕ_{micro} to zero, a value of ϕ_{macro} close to $6.0°$ is obtained. Although this value of ϕ_{macro} is calculated from the average of the deviator stress, the frictionless granular media offers a resistance to shear. Similar results have been found experimentally by Skinner [110], in theoretical work by Cambou [111], and more recently in DEM using disks by Kruyt [112]. This support the idea that interparticle friction is not the unique cause of the macroscopic frictional behavior of granular materials, in fact, it might be certainly a consequence of the nonlocal behavior of granular assemblies where the contact scale is not the basic constitutive element.

3.3.4 Stress fluctuations

According to the Critical State Soil Mechanics, large shear deformations drive the granular specimen to limiting state as presented in Sec. 3.3.1. This state is characterized by an isochoric deformation, where the stress ratio and the frictional dissipation stay constant [11]. This is not exactly that our simulations show. Indeed, we find that samples with different densities reach the same critical state, where the density and the stress ratio stay approximately constant, except for some fluctuations. In this Section we investigate the onset of such instabilities exploring the time evolution of the microstructural arrangement of the granular sample by following the evolution the fraction of sliding

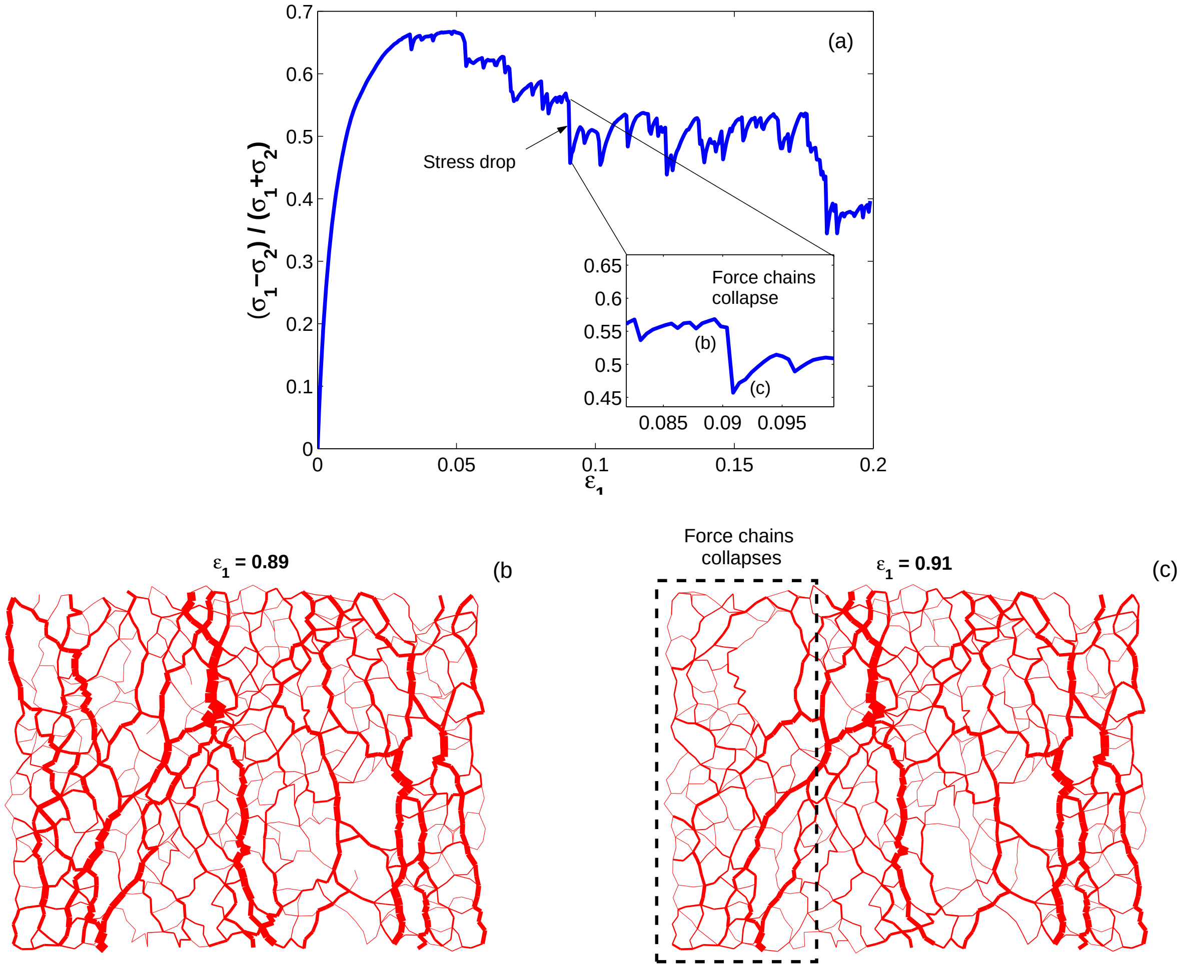

Figure 3.16: Stress drops (a) and their correlation with collapse of force chains: force network just before the stress drop (b) and right after it (c). The width of the lines is proportional to the magnitude of the contact force. The spatial correlation of the contact network in a packing of polygons is more pronounced than in the case of disks. This is reflected in the exponential tail of the distribution of contact forces. In the case of polygons, it is given by $N(f_n) \sim \exp(-x^{1.6})$ [82]. This is different from the distribution $N(f_n) \sim \exp(-x)$ of circular particles [27].

contacts n_s and the force chains.

In Figure 3.16 the direct relation between stress drops and collapse of force chains is presented. We selected one of the several stress drops as depicted in Figure 3.16(a). Then we plot the contact forces of the particles just before the stress drop Fig. 3.16(b) and right after it Fig. 3.16(c). Comparing these two force networks, one can see that some of the principal force chains after the stress drop have collapsed and therefore disappeared.

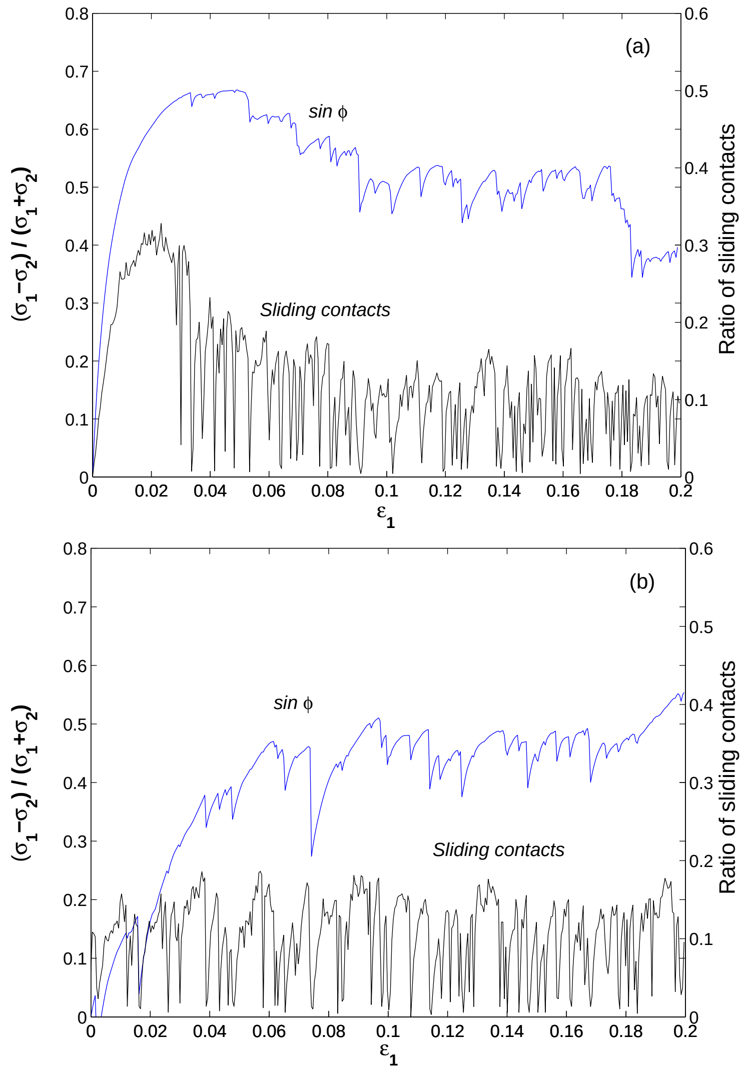

Figure 3.17: Evolution of stress-strain and the fraction of sliding contacts with axial strain (a) dense, (b) loose

This collapse drives the system to an internal rearrangement, in which particles undergo big relative displacements. The last is confirmed by the study of the displacement field of the individual particles as performed in Sec. 3.3.2, where big displacements of the particles are associated with abrupt reductions of the stress. Between two collapses the force chains build up leading to an increase of the macroscopic friction coefficient.

The microstructure of these collapses can be also visualized in the population of the sliding contacts. Figure 3.17 shows the fraction of sliding contacts n_s for dense and loose sample. The sliding condition is given by the Coulomb's condition, $F_t^c = \mu \cdot F_n^c$. Initially, the dense medium has more sliding contacts when it contracts. Later when the sample begins to expand the number decreases. In general, the evolution of the sliding contacts for both systems during loading, consists of stages where their number increases, and short time "failures" where the fraction of sliding contacts jumps down.

Figure 3.17 also compares the stress-strain evolution to the fraction of sliding contacts n_s. We observe more initial stability, with low frequency of jumps in the stress, in the dense sample. This stability is related to the average coordination number of the medium (Sec. 3.3.1), and the bigger this value the bigger the resulting stability of the granular skeleton. Although the jumps observed in the stress-strain behavior are less frequent than ones in the sliding contacts (see Fig. 3.17), each stress jump is associated with an abrupt reduction of the number of sliding contacts. Each stress drop matches with a collapse of the fraction of sliding contacts.

These jumps in the stress deviator are present in realistic experiments of granular material, but on a smaller scale [40, 41, 79]. In our simulations the magnitude of these fluctuations can be partially attributed to the small size of the sample. One may ask the question if these fluctuations disappear as the size of the sample increases. Simulations results presented in Sec. 3.2 show that these fluctuations barely decrease as the number of particles of the specimen increases [38]. The distribution of energy released of these fluctuations in shear cell experiments follows approximately a power law [37]. The analogy of this statistics with the Gutenberg-Ritcher law will be introduced in Chapter 5 of this thesis.

3.4 Concluding remarks

In order to investigate the characteristic modes of deformation and the stationary state that granular packings attain under monotonic load, we perform specific test for the small and large deformation stages. We summarize the results of this chapter as follows:

- For the small deformation stage stress-controlled quasi-static loading tests on granular polygonal packings have been performed. A direct relationship between the way in which strain is accumulated and the behavior of the sliding contacts has been found. As the stress imposed on the sample increases, the strain and the number of sliding contacts gradually increases. It can be then observed a localization of the deformation on an incipient shear band (Figure 3.5). At some point, the strain accumulation shows some discontinuous jumps in which the number of sliding contacts in the sample decays almost to zero. These jumps are related to force chain collapses as presented in Sec. 3.3.4, and therefore to a rearrangement of the granular packing. In this stage, there is a stress relaxation, and the grains can move more freely and contacts are removed from the sliding condition. These drop-offs of the sliding contacts seem to be independent of system size and appear with a characteristic frequency strongly dependent on friction.

- The existence and uniqueness of the steady state that granular materials reach under larger shear deformations have been assessed for different initial conditions. The results show that at large strains the samples reach the critical state independent on their initial density, and they deform at constant void ratio, shear stress, fabric anisotropy and mechanical coordination number. The last one has been found to be the first variable to attain a critical value making possible for the rest of micro-and-macro-mechanical variables the convergence to the critical state. The uniqueness of the critical state is validated for our simulations, when it is found that the critical states related to different stress states collapse onto only one critical state line. We have also proven that for a wide range of contact friction coefficients, axial loading leads to the same critical state. These results are valid for particles with regular shape, in the next chapter we will study the influence of the anisotropic shape of the particles on the previous remarks.

- In the critical state the system approaches and retreats an unstable behavior leading to strong fluctuations of stress. The stress drops were correlated to the fraction of sliding contacts and the stability yielded by the coordination number. We found that the granular sample at critical state develops force chains highly susceptible to collapse, driven to strong stress fluctuations. Stress collapses remove the contacts from the sliding condition, and therefore lead to a temporal stability in the granular sample.

- Biaxial experiments on granular packings with interparticle friction coefficient equal to zero yield a small but still important resistance to shear. This fact implies that interparticle friction is not the unique cause of the macroscopic frictional behavior of granular materials, and is therefore in agreement with the idea of the nonlocal behavior of granular assemblies where the macro-mechanical behavior stems not only from phenomena occurring at the contact scale, but also from mesoscale arrangements such as fabric evolution [44] and force chains [45–47].

Chapter 4

Influence of particle shape and induced anisotropy

There is still no clear information at the micro and macro-mechanical level about the influence of anisotropic particle shape on the evolution of granular materials and the corresponding anisotropic network of contacts towards the critical state reached at the global level. Furthermore, the comprehension of the related micro-mechanisms are very important in geotechnical engineering and physics in order to get a better understanding of the mechanical response of granular materials.

It is known, that the observed macro-mechanical response is a result of particle-level mechanisms, i.e, rolling [31–33] and contact sliding [34, 35], and of mesoscale arrangements such as force chains [44, 46] and fabric anisotropy [66, 113, 114]. For such mechanisms, particle shape is expected to play an important role [19, 21, 33, 48, 103, 115]. The relevance of anisotropic shape stems from the stronger interlocking between particles and the associated hindering of particle rotation.

In this chapter, we study the influence of anisotropic particle shape on the global mechanical behavior of granular media and its evolution toward the critical state. We perform molecular dynamics simulations of biaxial compression and of periodic shear cells. We focus on the influence of particle shape anisotropy on the overall plastic response. Further, the dependency of the mechanical behavior on the evolution of inherent anisotropy, specially contact and non-spherical particle orientations, is studied. Results are analyzed from the macro and micro-mechanical point of view.

In our MD simulations of shear cell tests, the results at macro-mechanical level show that for large shear deformation samples with anisotropic particles reach the same stationary state independent of the initial particle orientations [48]. For isotropic particles the direction of the principal axis of the fabric tensor at the critical state is aligned with the principal axis of the stress tensor, while for elongated particles the fabric orientation is strongly dependent on the orientation of the particles. Results of the isotropic compression of the samples and the biaxial test are presented in Sections 4.1 and 4.2, respectively. In Section 4.3 results of the shear cell tests and the mechanical parameters at the critical state are discussed. Finally, in Section 4.4 the concluding remarks are presented.

4.1 Packing density and initial anisotropy during isotropic compresion

In this section we study the influence of particle shape anisotropy on the maximum and minimum values of density obtained through isotropic compression and on the initial anisotropy. To construct the granular samples, the reference regular square lattice used to generate the isotropic polygons is distorted in vertical or horizontal direction to obtain the anisotropic particles. Then, particles are moved apart to attain a very loose state. In this loose state, we use rigid walls as boundaries to compress the system till the desired confining pressure is reached. Further details of the construction process are presented in Sec. 2.4. Axial (vertical) and lateral (horizontal) directions are indicated as 1 and 2, respectively (see Fig. 3.1).

We use an initial isotropic confining pressure $p_0 = 16$ kN/m, and a system size $N = 900$ particles. The material parameters of the simulations are $k_n = 1.6 \cdot 10^8$ N/m, $\epsilon_n = 0.8$, $k_t/k_n = 0.33$, $\epsilon_t/\epsilon_n = 1.1$, and the interparticle friction coefficient $\mu = 0.5$. We consider two different types of convex polygons as illustrated in Fig. 4.1. Polygons depicted in Fig. 4.1(a) with an almost isotropic shape, from now on, will be called 'isotropic' particles, and polygons in Fig. 4.1(b) will be referred as 'elongated' or 'anisotropic' particles. Samples with anisotropic particles are labeled V or H, depending on the direction (vertical or horizontal) along which were initially stretched. The shape of the anisotropic particles is described by the aspect ratio λ, between the length of the longest and shortest axis of the particles.

In Figure 4.2a the minimum and maximum values of the void ratio, e_{min} and e_{max}, characterizing the density of the isotropic ($\lambda = 1$) and elongated ($\lambda > 1$) particles are presented. Being the void ratio $e = V_v/V_s$, with V_v the volume of voids and V_s the volume

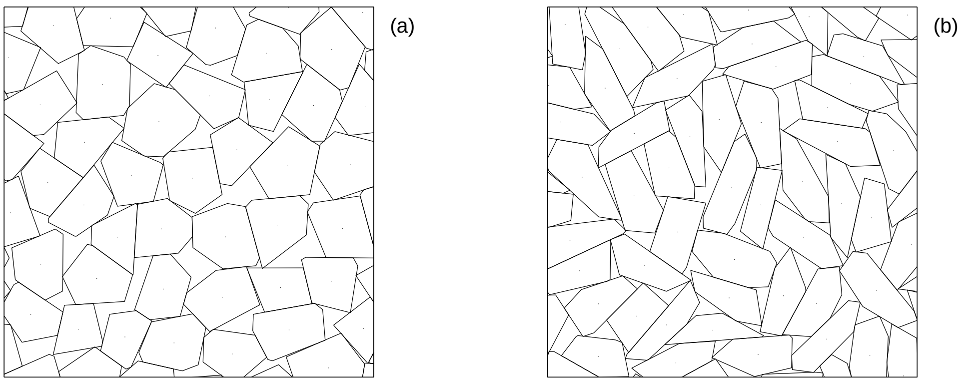

Figure 4.1: Two types of particles used in the numerical simulations: (a) isotropic ($\lambda = 1.0$) and (b) elongated polygons ($\lambda > 1.0$). Points are the center of mass of the polygons. In this particular case, elongated polygons have aspect ratio $\lambda = 2.3$

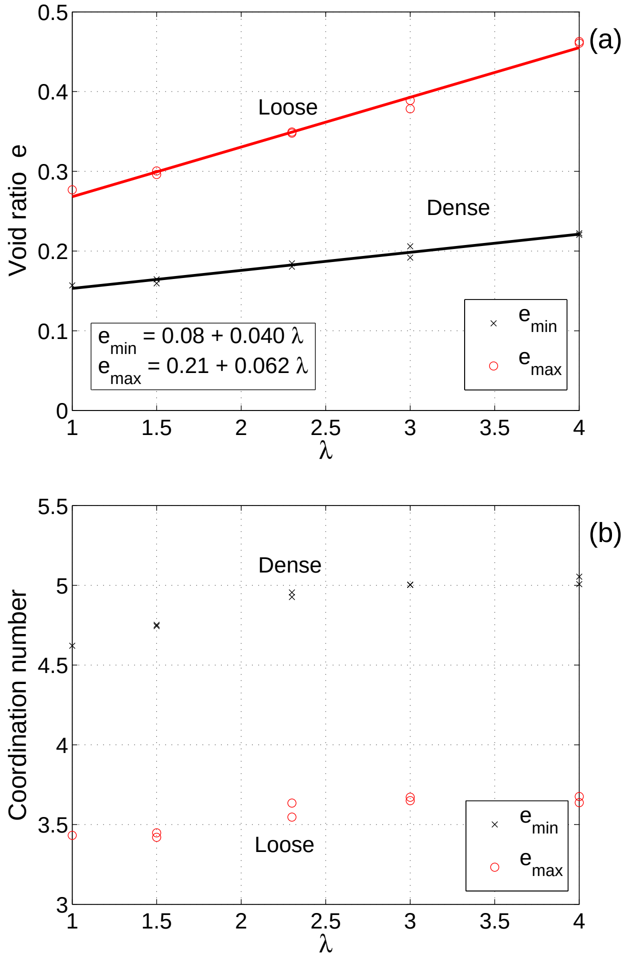

Figure 4.2: Influence of particle shape on (a) the limit void ratios e_{mix} and e_{max} and (b) the coordination number of the granular samples obtained through isotropic compression. Isotropic ($\lambda = 1$) and anisotropic samples ($\lambda > 1$) are used. Anisotropic samples H and V are presented.

of solid grains. One can notice that the value of void ratio e increases with the anisotropy of particle shape λ. The difference between the limit values of the void ratio e_{mix} and e_{max} also increases with λ. The behavior of both density states can be well fitted by a linear expression as shown in Fig. 4.2a. Similar experimental results have been found previously on realistic granular materials [19, 116]. This is a natural consequence of the particle shape anisotropy, which hinders particle rotation and thus the possibility for the granular system to reach denser states. Elongated particles also enables the existence of big gaps and open voids between particles [19].

The mean number of contacts per particle of the assembly, also called coordination number, is presented in Fig 4.2b. The coordination number Z increases with λ due to the larger relative plane surface of anisotropic particles that enables a larger number of

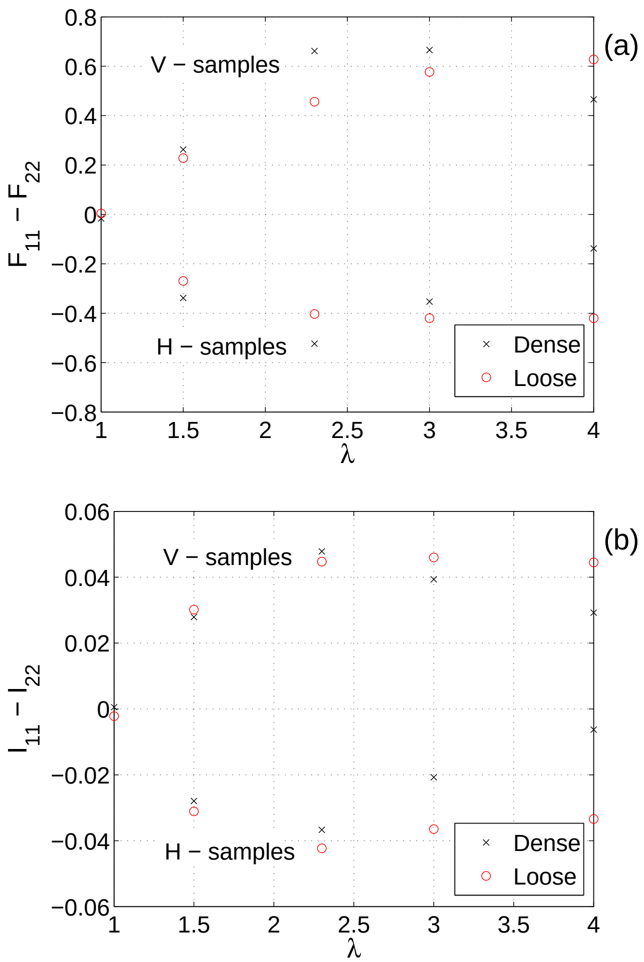

Figure 4.3: Influence of particle shape on the fabric anisotropy and particle orientation of dense and loose samples after the isotropic compression. We present in (a) the deviatoric fabric $F_{11} - F_{22}$ and in (b) the deviatoric component of inertia tensor $I_{11} - I_{22}$. The initial elongation of the particles along the vertical 11 or horizontal 22 direction are indicated with labels V and H, respectively.

contacts. Around a value of $\lambda = 3$ the coordination number saturates to a constan value. The direction along which the anisotropic particles are stretched during the construction process has no influence in the final density state and coordination number as observed in Fig. 4.2.

The situation is different when we look at the anisotropy of the contact network and the orientation of elongated particles. The contact network is described by the mean fabric tensor $\mathbf{F}$ and the orientation of the particles by the mean inertia tensor $\mathbf{I}$. The deviatoric component of $\mathbf{F}$ and $\mathbf{I}$ characterizes the anisotropy of the fabric and the orientation of anisotropic particles, respectively. In Figure 4.3, the deviatoric component $F_{11} - F_{22}$ of the fabric tensor $\mathbf{F}$ and the deviatoric component $I_{11} - I_{22}$ of inertia tensor

I are presented. We can observe in Fig. 4.3a, that starting from a value close to zero for isotropic particles ($\lambda = 1$) the anisotropy of the fabric increases with λ. The preferential orientation of the contacts between the particles is determined by the direction in which the particles are stretched before the compression. That is to say, vertical samples V with particles initially distorted in axial direction develop most of the contacts along the axial axis 11. This is similar in the case of horizontal samples H where the preferred orientation is the lateral axis 22. The preferential orientation of the particles is also determined by the initial direction along which anisotropic particles are elongated, see Fig. 4.3b. In conclusion, the parameter controlling the final mean orientation of the particles as well as the fabric of the assembly is the direction along the particles are initially distorted. These observations are independent of the final density state of the sample. A good correlation between particle orientation and the direction in which contacts are generated is also observed [48].

4.2 Biaxial test simulations

In this section, we evaluate the influence of particle shape anisotropy on the evolution of granular packings toward the critical state. At the critical state granular materials undergo unlimited shear deformation at constant volume and stress ratio [11]. The same procedure as the one used in Chapter 3 for isotropic particles (monotonic biaxial compression) is employed. The effect of the orientation of the initial fabric, i.e., contact network and orientation of anisotropic particles, with respect to the direction of loading is examined. The experimental procedure is the same of the strain controlled test presented in Section 3.3. Particles are contained by rigid wall boundaries, and the deviatoric stress is induced moving the horizontal walls (axial direction) at a constant rate $\dot{\varepsilon}_1$ while the lateral stress σ_2 is kept constant at 16 kN/m. Since our model does not take into account the crushing of particles , we retain low stress levels. For this stress condition dense samples still expand and exhibit a peak on the stress behavior [11]. The material parameters of the simulations are the same of the previous section. Two aspect ratio are used, isotropic samples ($\lambda = 1$) and anisotropic ones ($\lambda = 2.3$). The longest axis of the particles for sample V is parallel to the direction of loading, and for H samples is perpendicular to it.

In Figure 4.4 the macro-mechanical evolution of the systems is presented. Fig. 4.4a shows the evolution of $\sin\phi = (\sigma_1 - \sigma_2)/(\sigma_1 + \sigma_2)$ with the axial strain ε_1. As already presented in Chapter 3, dense samples exhibit a higher initial stiffness and also a peak strength. After this peak a strain-softening behavior is observed. The loose media do not exhibit a peak. At large deformation, samples with the same λ value and the same particle orientation seem to reach a stationary value of stress within statistical fluctuations.

Figure 4.4b illustrates the evolution of the void ratio e with the axial strain. Initially, dense samples contract and later expand. For large axial strain values dense and loose samples with the same aspect ratio and initial orientation reach a similar void ratio. In the case of isotropic samples, once they have reached the same value of void ratio they

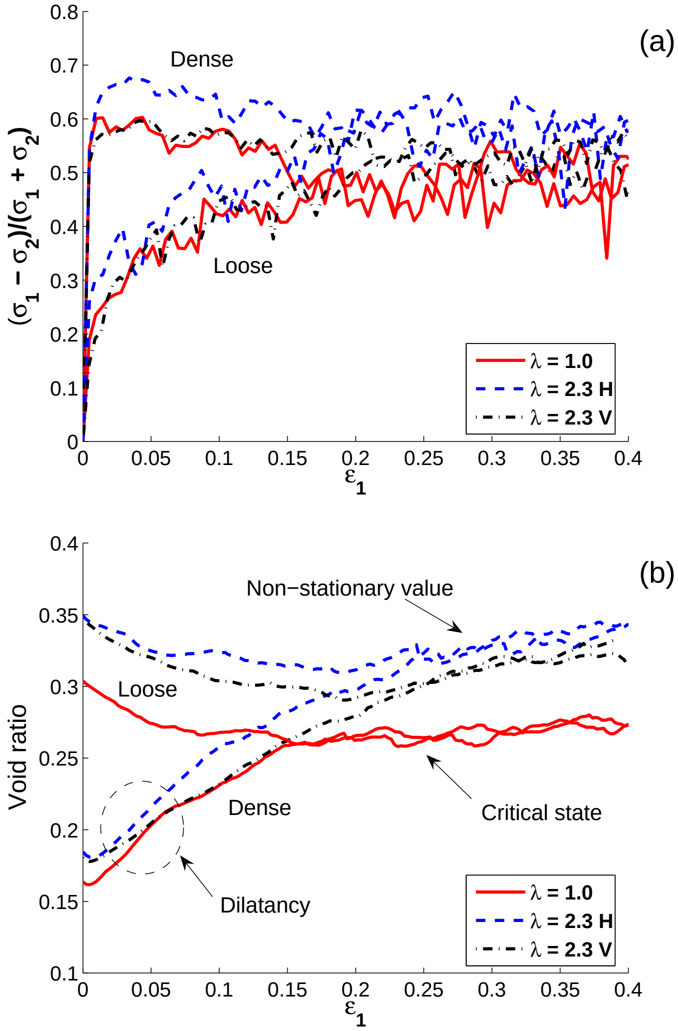

Figure 4.4: Influence of particle shape on the evolution of (a) the deviator stress and (b) the void ratio of the samples under biaxial compression. Isotropic $\lambda = 1$ and anisotropic samples $\lambda = 2.3$ are used.

deform at constant e and constant shear stress. This is the critical state of the material, which is independent of the initial density state [6, 11] (see also Chapter 3). On the other hand, although the anisotropic samples reach similar value of void ratio they continue dilating and no stationary value of e is reached. We conclude that such anisotropic samples do not attain the critical state under biaxial compression. This result has been previously observed in numerical simulations with DEM [76].

The non-convergence of anisotropic samples to the critical state can be micromechanically explained by looking at the evolution of the coordination number, of the deviatoric component $F_{11} - F_{22}$ of the fabric tensor, and of the deviatoric component $I_{11} - I_{22}$ of the inertia tensor. In Chapter 3, a critical value of the coordination number Z was found to

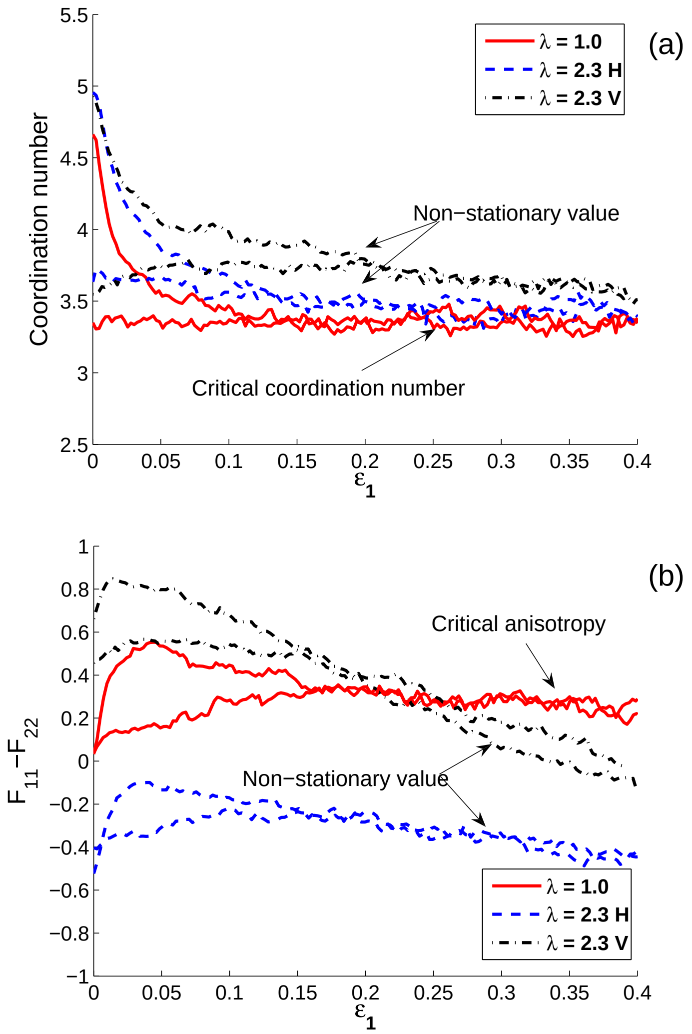

Figure 4.5: Influence of particle shape on the evolution of (a) the coordination number and (b) the deviatoric fabric $F_{11} - F_{22}$ of the granular samples under biaxial compression. Isotropic ($\lambda = 1$) and anisotropic samples ($\lambda = 2.3$) are used.

be the first signal when the systems with isotropic particles approached the stationary state. On the contrary, anisotropic samples do not reach a steady value of the coordination number, as shown in Fig. 4.5(a). There, we can see that anisotropic samples have not arrived to a steady value of coordination number. The structural anisotropy is presented in Fig. 4.5(b). While the isotropic samples reach a critical value of anisotropy, the contact network of anisotropic samples is still changing. The non-stationary state of these variables is directly related to the evolution of the particle orientation. In Figure 4.6 the evolution of $I_{11} - I_{22}$ is presented. We can observe that elongated particles are reoriented during the shear process without converging to a steady state. Thus, the contact network for anisotropic particles does not reach a stationary state either. This micro-mechanical

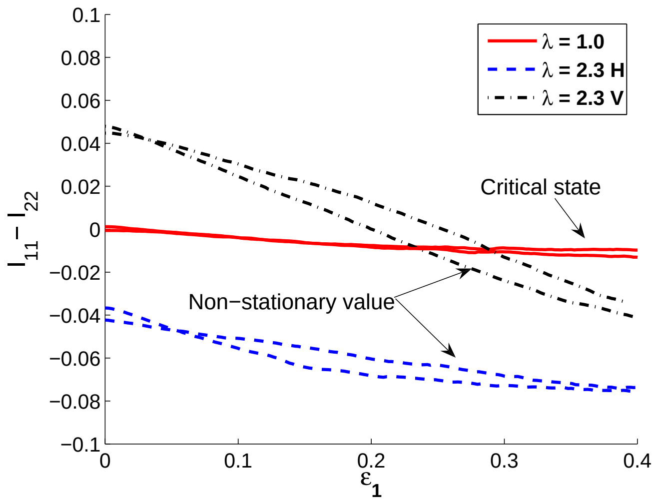

Figure 4.6: Influence of particle shape on the evolution of a) the deviatoric component of inertia tensor $I_{11} - I_{22}$ of the granular samples under biaxial compression. Isotropic ($\lambda = 1$) and anisotropic samples ($\lambda = 2.3$) are used.

evidence, concerning the non-stationary state of the fabric and particle orientation, does not allow the systems to reach the critical state.

Next, we only discuss mechanical properties related to the peak strength ϕ_{peak} on dense packings since anisotropic samples do not attain a stationary state. We analyze the influence of particle shape, initial particle orientation and fabric anisotropy on the mechanical behavior before peak. From Figure 4.4, we see that the anisotropic sample H develops a higher peak strength than sample V. This can be explained in terms of the stability of the packing, i.e., particles oriented perpendicular to the direction of loading (sample H) exhibit the most stable configuration and therefore the higher peak strength. On the contrary, sample V presents an unstable configuration that deforms towards a more stable structure. In this new configuration the particles are oriented perpendicular to the loading direction. This becomes clear if we look at the evolution of the major principal direction θ_I of the inertia tensor and the major principal direction θ_F of the fabric tensor presented in Fig. 4.7. These principal directions are measured with the horizontal axis x. We can see that for sample H, θ_I remains constant at $\approx 180°$, since it is the most stable configuration to loading. Moreover, θ_F follows approximately the particle orientation θ_I. In the case of samples V, θ_I is reoriented toward the horizontal direction. The fabric orientation θ_F is determined by the particle orientation. Hence, as soon as particles are reoriented, the preferential orientation of the contact network θ_F follows θ_I (Fig 4.7b). The fabric in isotropic particles is always oriented in direction of loading $90°$.

Ii is known that an important amount of the energy necessary to shear dense granular media is used in dilation [19, 117]. In this process the breakage of interlocking between particles is necessary to reduce the coordination number. It is therefore expected that the difference on the peak strength is related to the dilatancy rate of the samples. In

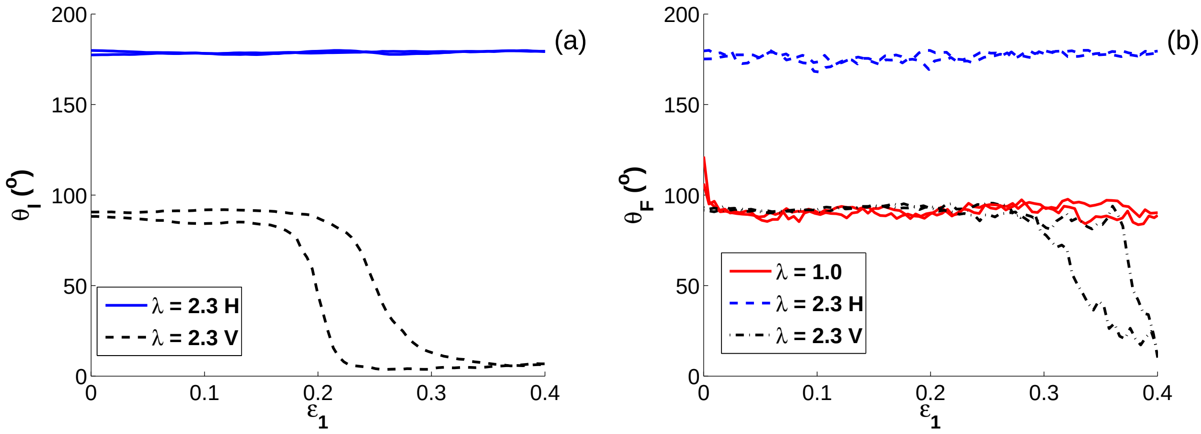

Figure 4.7: Evolution of the major principal direction (a) θ_I of the inertia tensor and (b) θ_F of the fabric tensor for isotropic particles (λ = 1.0), and elongated particles (λ = 2.3). Particles initially oriented in horizontal direction are labeled H and in vertical direction V.

Figure 4.4b, one can see that sample H with higher peak strength has a larger dilatancy angle Ψ than sample V. This difference on the dilatancy rate is also reflected in the coordination number of the samples. In Figure 4.5(a), we see that despite the same initial coordination number the sample V (with smaller dilatancy rate) deforms during the shear process with larger coordination number. This is due to the less breakage of contacts. All these facts confirm the close relation between peak strength, dilatancy rate and coordination number of the samples. Similar experimental results concerning peak strength and dilatancy rate have been observed on natural sands under triaxial compression [113].

To compare the strength that the isotropic and the anisotropic samples mobilize at peak, one has to consider the influence of the stress-induced fabric anisotropy. This is a determinant factor on the overall strength of granular packings [66, 114]. One can expect that the larger the induced fabric anisotropy the larger the strength. The evolution of the fabric anisotropy of the dense granular samples is as follows (see Fig. 4.5). Initially, the deviatoric fabric $F_{11} - F_{22}$ evolves in the direction of loading. This evolution is independent of the initial anisotropy. In particular, for samples H the initial anisotropy is partially erased and reoriented in the loading direction. The anisotropy reaches its peak at similar axial strain value to the one at which the material develops its maximum strength. Hereafter, the fabric anisotropy decreases due to collapses of force chains during the softening regime [118]. The total induced fabric anisotropy at peak strength is the difference between the value at peak and the initial one.

In Figure 4.8, the peak strength and the induced fabric anisotropy for different aspect ratio of the particles are presented. We can see that anisotropic samples H develop higher ϕ_{peak} than isotropic samples due to their stable structure, irrespective of the induced anisotropy. On the contrary, the unstable configuration of samples V develops lower or similar strength. In general, anisotropic samples before reaching the peak un-

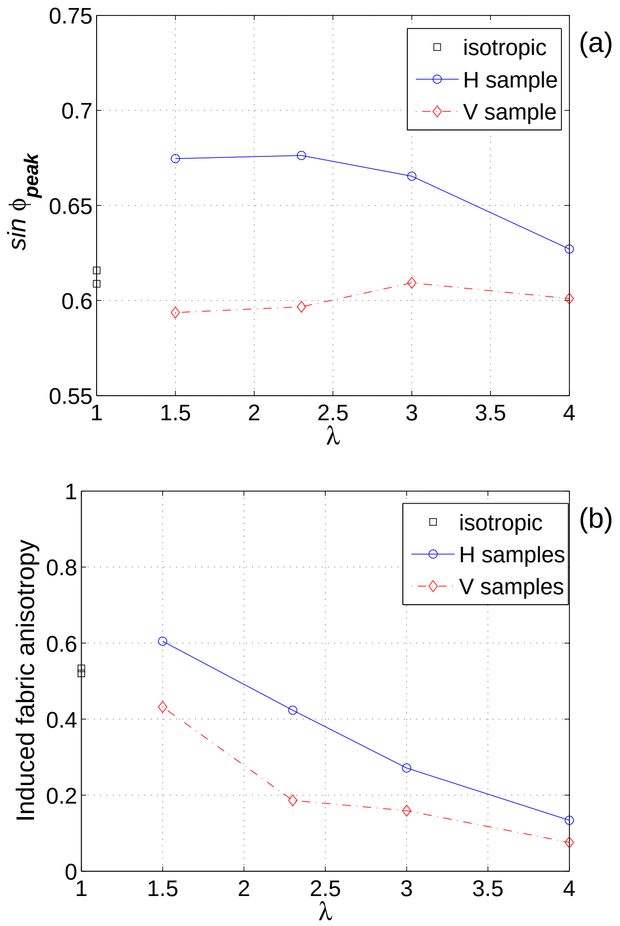

Figure 4.8: Influence of particle shape on (a) peak strength $\sin\phi_{peak}$ and (b) induced fabric anisotropy at peak under biaxial compression. Isotropic ($\lambda = 1$) and anisotropic samples ($\lambda > 1$) are used. Anisotropic samples H and V are presented.

dergo smaller fabric changes than isotropic samples due to the stronger interlocking and preferential orientation of particles. The same is observed when comparing samples H to samples V.

Finally, we plot in Fig. 4.9 the difference on peak strength $\Delta\sin\phi_{peak}$ and the corresponding difference of the induced fabric anisotropy for samples with the same aspect ratio λ. We can observe that a good correlation between $\Delta\sin\phi_{peak}$ and Δ induced fabric anisotropy is present. This correlation seems to be independent of the aspect ratio, but still a deviation is observed. This deviation is expected, since additional factors responsible for the shear strength such the development of internal forces and its relation to the fabric are not being considered. Further investigations regarding the relationship between fabric, internal forces, and shear strength can be found in Ref. [30, 114, 119, 120].

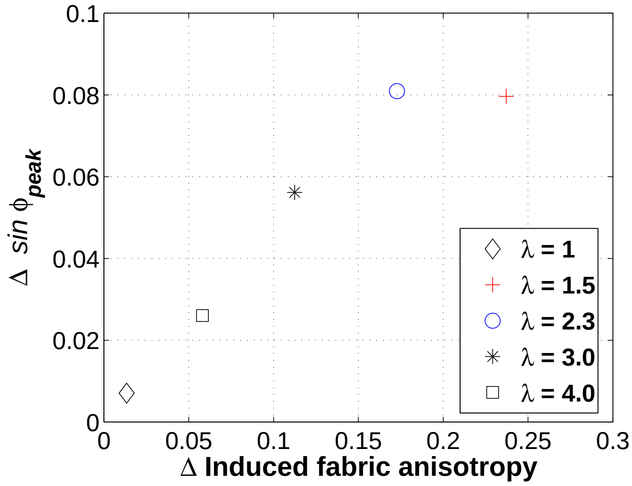

Figure 4.9: Relationship between the difference of induced fabric anisotropy and the difference of peak strength $\Delta \sin \phi_{peak}$ for samples with the same aspect ratio λ.

4.3 Shear Cell test - Critical state

In this section, we study the existence of the critical state for samples consisting of anisotropic particles and the corresponding global mechanical behavior. The evolution of micro-mechanical variables such as the fabric tensor, the stress tensor and the inertia tensor are considered. In Section 4.3.1 the experimental setup is presented. In Sections 4.3.2, 4.3.3, 4.3.4 the results concerning mechanical behavior, evolution of micro-mechanical variables and particle rotation are discussed. In these sections, two aspect ratio of the particles are investigated, isotropic ($\lambda = 1.0$) and anisotropic ($\lambda = 2.3$). In Section 4.3.5, we present a summary of the influence of the aspect ratio on the micro and macro-mechanical parameters obtained at the critical state.

4.3.1 Numerical experiment

A configuration of the shear cell used in our simulations is depicted in Figure 4.10. The shear cell contains 1500 particles, being 50 particle diameters wide and 30 diameters high. The mean diameter of the particles is 1 cm. Periodic boundary conditions are imposed in horizontal direction. The top and bottom have fixed boundary conditions. A constant confining stress $p_0 = 16$ kN/m is imposed between the bottom and the top horizontal walls. The top and bottom layers of particles are moved in opposite direction with a constant shear rate $\dot{\gamma}$. The particles in these layers are not allowed to rotate or move against each other. The top boundary is free to move in vertical direction in order to permit a volumetric change of the sample, while the bottom is kept fixed.

In all simulations the mechanical parameters are the same given in Section 4.1. Additionally, a background damping coefficient ν_b = 12 s^{-1} was used. This produces a

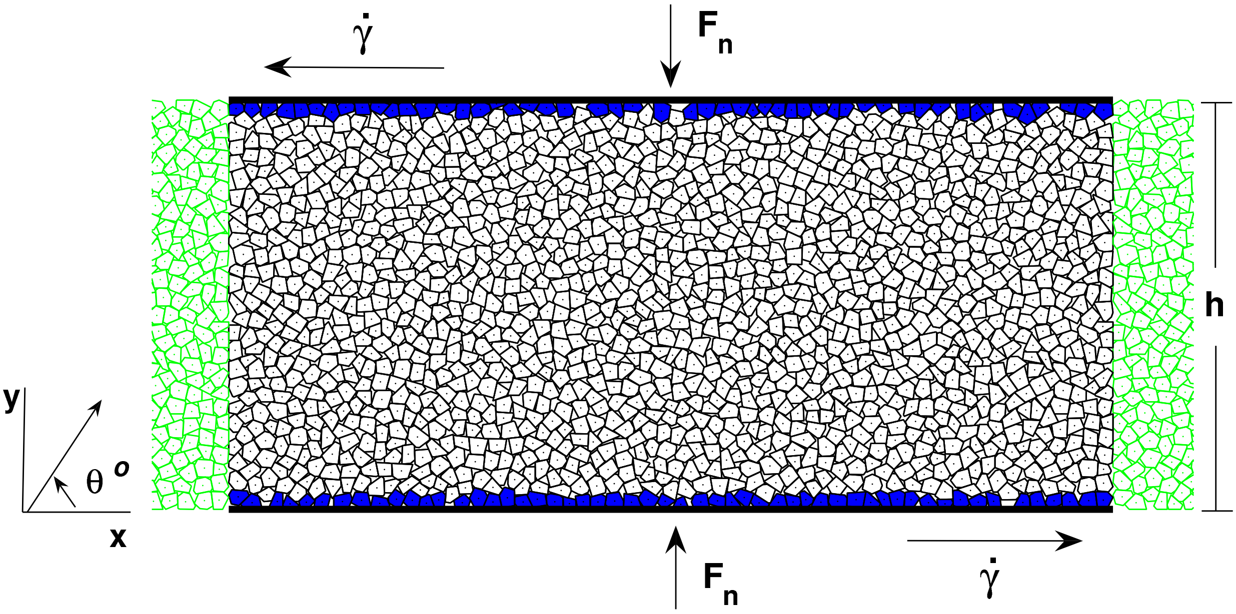

Figure 4.10: Sketch of the shear cell. A normal force is applied between top and bottom wall. A constant shear rate $\dot{\gamma}$ is used to shear the sample. Light particles (green in color) correspond to the image used to implement the periodic boundary conditions.

background damping force, which is introduced in order to model the friction between the particles and the bottom (or top) of the shear cell used on the two-dimensional experiments performed by Veje et. al [121], and Howell et al. [122]. In order to evaluate the influence of ν_b on the mechanical behavior of the medium, we performed simulations with no and different values of it. We found that the damping ν_b in the range used here has neither effect on the evolution of the internal variables nor the global mechanical response of the medium.

The horizontal and vertical directions are indicated as x and y, respectively. In order to study the evolution of the packing we use the strain variable γ, which is defined as follows $\gamma = D_x/h_o$, where D_x is the horizontal displacement of the boundary particles and h_o is the initial height of the sample. The void ratio e of the sample is related to the volumetric deformation, $e = V_T/V_S - 1$, where V_T is the total volume of the sample and V_S the volume occupied by all the particles.

4.3.2 Global mechanical behavior - effect of initial configuration

4.3.2.1 Statistically different samples

Samples corresponding to different seeds for the random number generation of the Voronoi tesellation are used to evaluate the global mechanical response of the granular packing. This is done in order to assess whether different initial configurations of

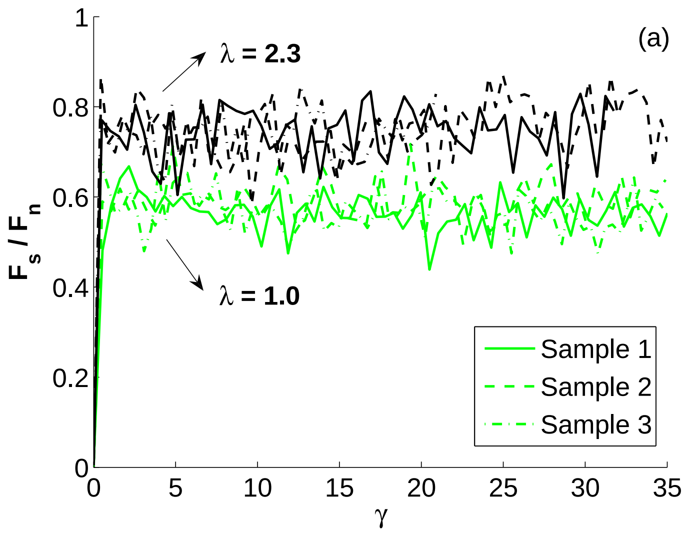

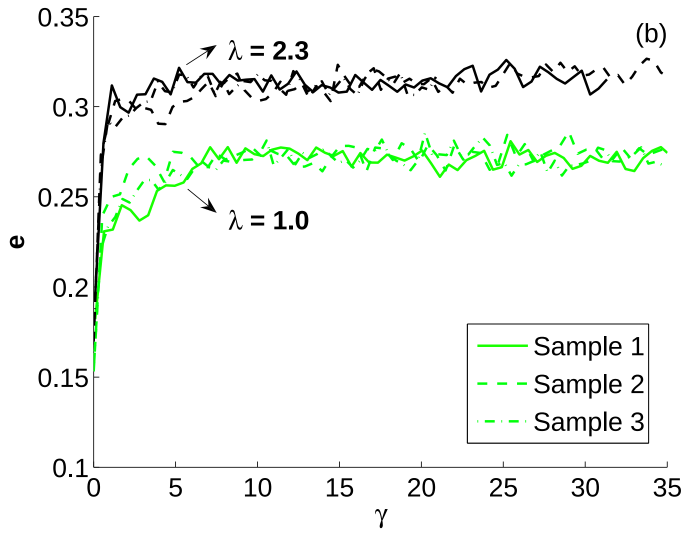

Figure 4.11: Evolution of (a) shear force and (b) void ratio for different samples with the same mechanical parameters. Isotropic (λ = 1.0) and elongated particles (λ = 2.3) are represented by light and dark lines, respectively.

particles reach the same steady state. Our results correspond to a shear rate $\dot{\gamma} = 0.35$ s^{-1}, and to elongated polygons initially oriented perpendicular to shear direction. In Figure 4.11 the evolution of the resultant shear force and the void ratio is presented for the different configurations. In Figure 4.11(a), the shear force F_s is normalized by the normal force F_n applied to the system. Initially, the ratio F_s/F_n has a strong increment

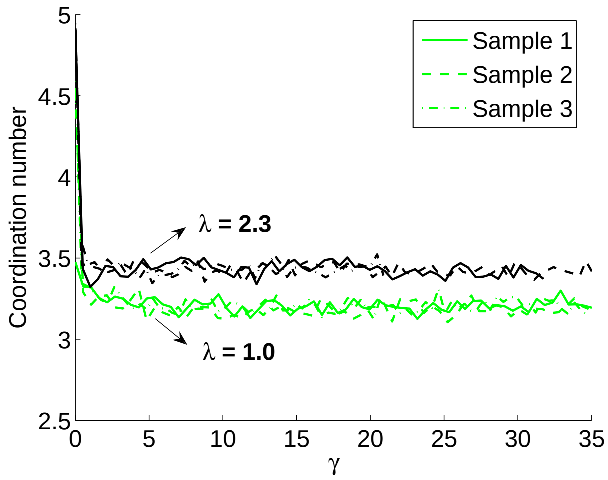

Figure 4.12: Evolution of the coordination number for different samples with the same mechanical parameters. Isotropic particles λ = 1.0 (light lines) and elongated ones λ = 2.3 (dark lines).

related to the breaking of the interlocking of the particles. After this stage, a saturation towards a nearly constant value of the F_s/F_n ratio necessary to shear the granular media is observed. This behavior is identical for all the samples. For small values of strain, the evolution of the void ratio (Figure 4.11b) also presents a high initial increase saturating later at a constant value. This saturation occurs slower than for F_s/F_n. Samples with elongated particles saturate at a higher value of F_s/F_n and also higher void ratio, as a consequence of the stronger interlocking due to the particle shape. One can therefore conclude that elongated grains are more sensitive to volumetric changes and develop a higher shear strength. This result had been in fact previously observed [76, 103]. We consider this saturation of the F_s/F_n value and void ratio e as the steady state of the sheared material.

The evolution of the coordination number for isotropic and elongated particles is depicted in Figure 4.12. Note that, despite reaching a higher void ratio, samples with elongated particles saturate at larger value of coordination number compared to isotropic particles. This can be understood in terms of a geometrical effect, a consequence of the flat shape and/or larger relative plane surface in the λ = 2.3 case, which allows for a higher number of contacts per particle.

4.3.2.2 Different initial particle orientations

We study in this section the influence of the anisotropy on the macroscopic behavior of granular media due to the initial orientation of elongated particles. Three different initial configurations are obtained for the samples used in this analysis:

1. On average the grains are oriented parallel to the shear direction (this will be called

"horizontal" sample - H).

2. On average the grains are oriented perpendicular to the shear direction (we will call this the "vertical" sample - V).

3. Grains (H or V) are randomly rotated before isotropic compression (which we call the "random" samples - HR or VR).

Configurations number 1 and 2 correspond to samples with different initial orientation of the particles. Configuration number 3 is equal to configurations 1 and 2, but with an additional induced random rotation to the particles before the compression (between 0 and $2\pi\ rad$). In all three cases the samples wind up having a slight deviation from the

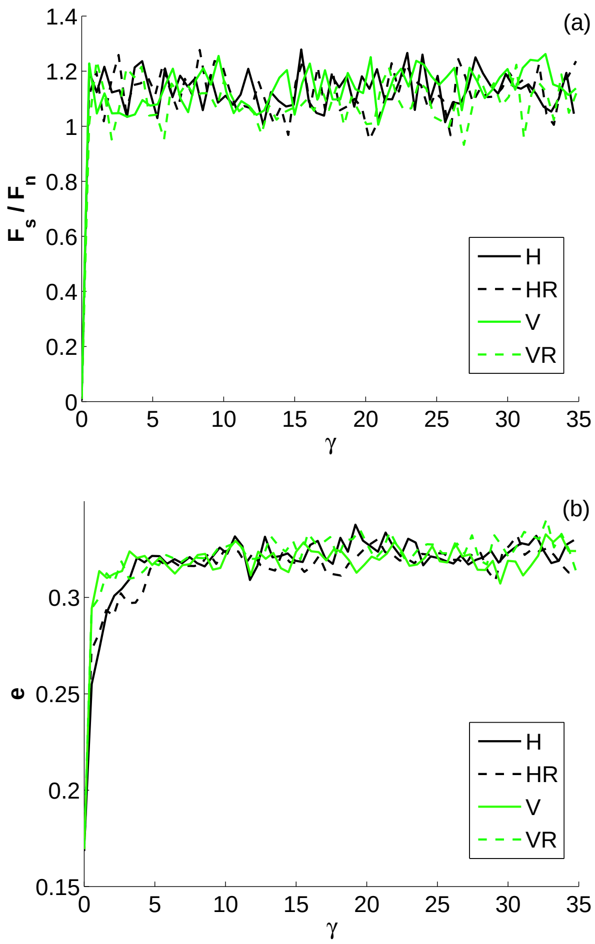

Figure 4.13: Evolution of (a) shear force and (b) void ratio for samples with different initial particle orientation, $\lambda = 2.3$. Samples labelled H and V have particles oriented in horizontal and vertical direction, respectively. R corresponds to an initial random rotation of the particles.

originally induced anisotropy due to the shape of the shear cell (rectangular), the rigid walls used for the compression, and the particle interactions during the construction process.

In Figure 4.13, the evolution of F_s/F_n and the void ratio e for samples with particles initially oriented in horizontal and vertical direction, and an additional random rotation is presented. Results correspond to a shear rate $\dot{\gamma} = 1.4\,\mathrm{s}^{-1}$. We notice that F_s/F_n and the void ratio e evolve toward the same saturation value when they reach the steady state independently of the initial anisotropy due to contact and particle orientations. This independence of the initial anisotropy will be explored by studying the evolution of the internal variables in Sec. 4.3.3.

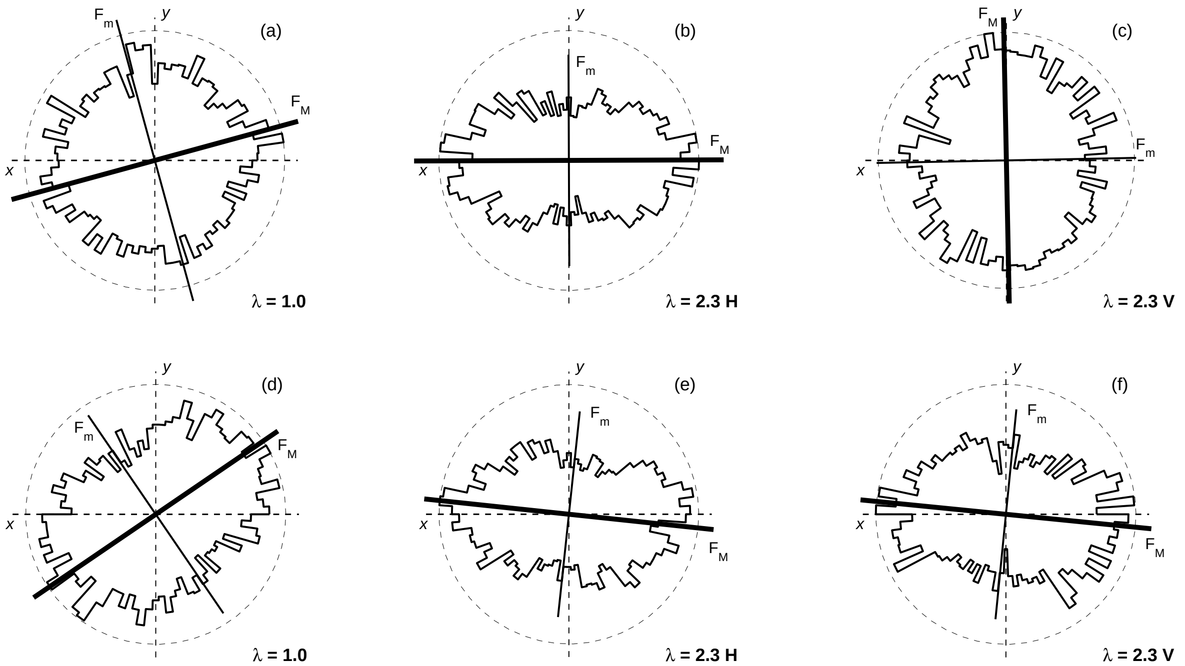

Figure 4.14: Polar distribution of branch vectors in the initial configuration (a,b,c) and the steady state (d,e,f), for isotropic particles λ = 1.0 (a,d), and elongated particles (λ = 2.3) initially oriented in horizontal direction (b,e) and in vertical direction (c,f). The principal directions of the mean fabric tensor (F_M and F_m), and the reference axes x and y are plotted with solid and dashed lines, respectively. The radius of the dashed circle corresponds to the maximum value of the distribution. The values here represented correspond to the steady state ($\gamma = 30$), when these magnitudes remain approximately constant.

4.3.3 Evolution of internal variables

The evolution of the local stress, the fabric and the inertia tensors of the isotropic and anisotropic samples is studied in this section.

In Figure 4.14(a-c), we show the orientational distribution of the branch vectors and the principal directions of the mean fabric tensor (F_M and F_m) for the initial configuration of the samples. Observe that, in the case of isotropic polygons (Fig. 4.14(a)), the distribution presents no preferred direction within the statistical fluctuations. For elongated polygons (Fig. 4.14(b-c)), however, one can observe that the major principal component of the fabric tensor $\mathbf{F}$ is oriented towards the direction in which the polygons were initially stretched.

The anisotropic distribution of the contact orientations is more pronounced in case (b) than in case (c); this is most probably due to the shape of the shear cell (which indeed is

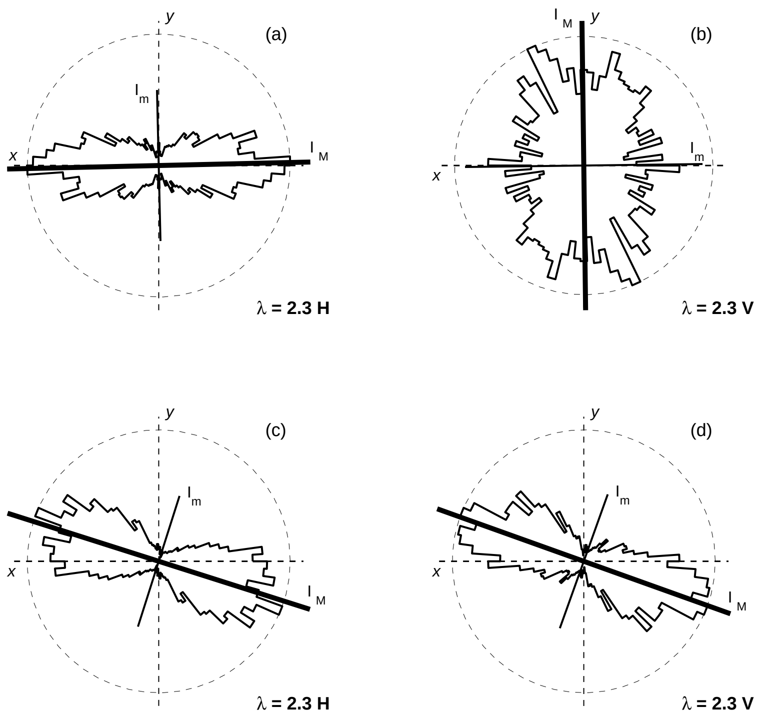

Figure 4.15: Polar distribution of particle orientations θ^p, initial configuration (a,b) and in the steady state (c,d) for elongated particles (λ = 2.3) initially oriented in horizontal direction (a,c) and in vertical direction (b,d). The principal directions of the global inertia tensor (I_M and I_m), and the reference axes x and y are plotted with solid and dashed lines, respectively. The radius of the dashed circle corresponds to the maximum value of the distribution. The values here represented correspond to the steady state ($\gamma = 30$), when these magnitudes remain approximately constant.

wider than higher) and the compression process using rigid walls. The angular distribution of the contacts in the steady state ($\gamma = 30$) is depicted in Figure 4.14(d-f). We notice that the distribution of contact orientations for elongated particles (Fig. 4.14(e-f)) is very similar independent of their initial orientation, while for isotropic particles (Fig. 4.14(d)) it is clearly different. The major principal direction of the fabric tensor follows this same trend.

In Figure 4.15, the polar distribution of θ^p for elongated particles, and the principal directions of the mean inertia tensor (I_M and I_m) in the beginning and in the stationary state are presented. We observe that, similar to the case of contact orientations, they evolve towards the same global orientation independently of the initial particle directions.

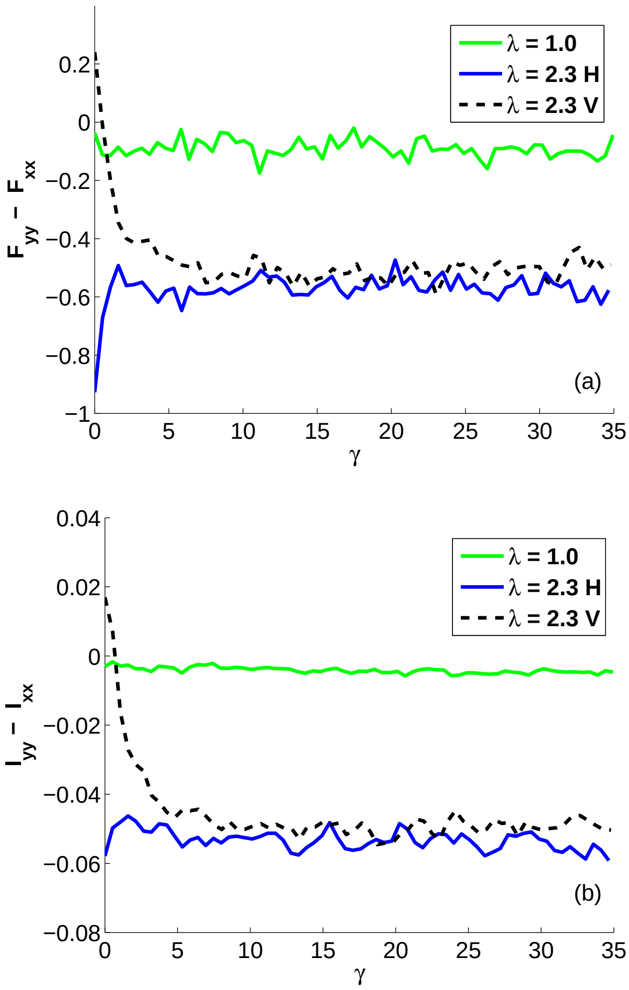

Figure 4.16: Evolution of the deviatoric component of the fabric (a) and the inertia tensor (b) for isotropic particles λ = 1.0, and elongated particles (λ = 2.3) initially oriented in horizontal direction (H) and in vertical direction (V).

In order to study the evolution of the fabric and inertia tensors we monitor their deviatoric component $F_{yy} - F_{xx}$, and the quotient F_{xx} / F_{yy} during the simulation. One can observe in Figure 4.16, where the evolution of the deviatoric component of F_{ij} and I_{ij} is shown, that the deviatoric reaches a stationary value for both types of particles, and that the induced anisotropy is much higher for elongated particles than for isotropic ones. The same result is observed for the quotient of the principal components of the tensors (Figure 4.17). This stationary value of the deviatoric component and the quotient is directly related to the steady state at the macro-mechanical level, and seems to be a micro-mechanical requirement for the global steady state. This assumption is supported by simulations of biaxial tests reported by Nouguier-Lehon et al. [76], where samples with

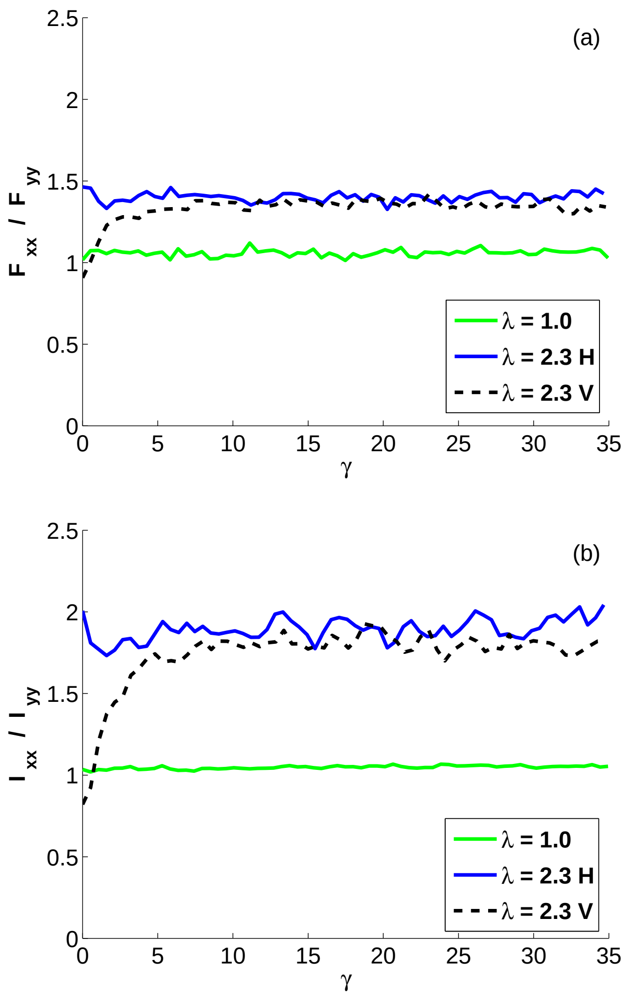

Figure 4.17: Evolution of the quotient of the principal components of the fabric (a) and the inertia (b) tensors for isotropic particles $\lambda = 1.0$, and elongated particles ($\lambda = 2.3$) initially oriented in horizontal direction (H) and in vertical direction (V).

elongated particles do not reach neither a stationary value for the components of the fabric and the orientation tensors nor the so-called critical state at the macro-mechanical level, but samples that reach the stationary state for the components of the tensors do so at the global level.

Furthermore, for samples with elongated polygons the deviatoric part of the F_{ij} and I_{ij} tensors, and the ratio of their principal components reach approximately the same stationary value independent of the initial particle orientations. This means that the initial inherent anisotropy (fabric and particle orientation) is completely erased and reoriented in direction of the induced shear during the experiment. The evolution of the major principal direction of the fabric θ_F, the inertia θ_I and the stress tensors θ_σ are shown in Figure 4.18. In the case of the inertia tensor, the major principal direction θ_I is reoriented for all samples towards an angle close to $160°$. For the stress tensor, θ_σ ($\approx 45°$) is the

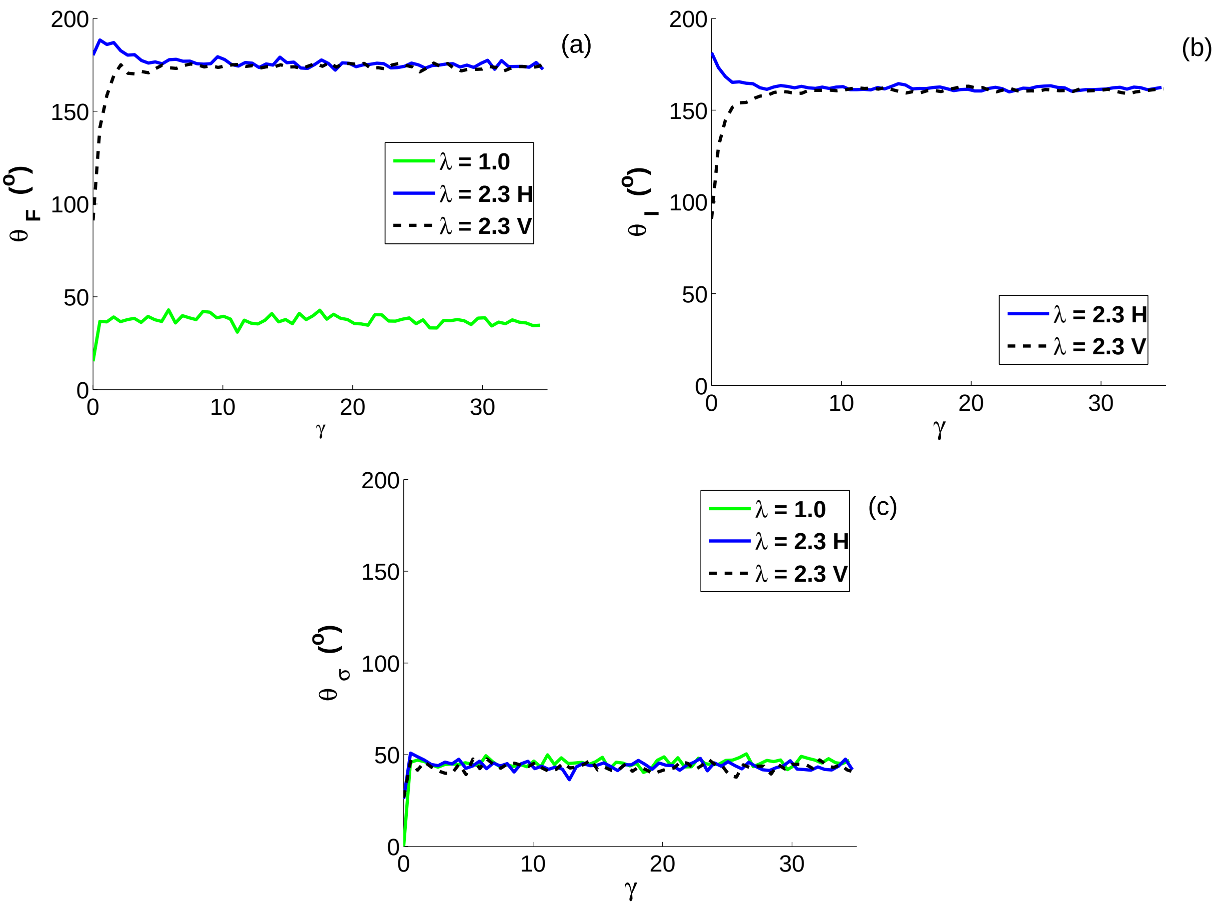

Figure 4.18: Evolution of the major principal direction of the fabric (a), the inertia (b), and the stress (c) tensors for isotropic particles λ = 1.0, and elongated particles (λ = 2.3) initially oriented in horizontal direction (H) and in vertical direction (V).

same for both particles independent of the particle shape. This orientation of the stress comes from the direction of the force chains carrying the largest stresses (Fig. 4.19(c-d)). On the other hand, the major principal direction of the fabric tensor θ_F is completely different for isotropic and elongated polygons. In the case of elongated polygons, the fabric orientation is close to the inertia tensor. For isotropic particles, the difference θ_F-θ_σ is about $5°$. The directions of fabric and stress are therefore practically aligned in our simulations, similarly to what Thornton and Zhnag [123] found in simple shear test simulations. Lätzel et al. [124], however, did not find any alignment of the direction of the tensors in simulations of a Couette shear-cell. This different result reinforces the importance of the boundary conditions (geometry of the tests) in the internal structure of the system.

To clarify further the result of different orientation of the fabric for isotropic and ani-

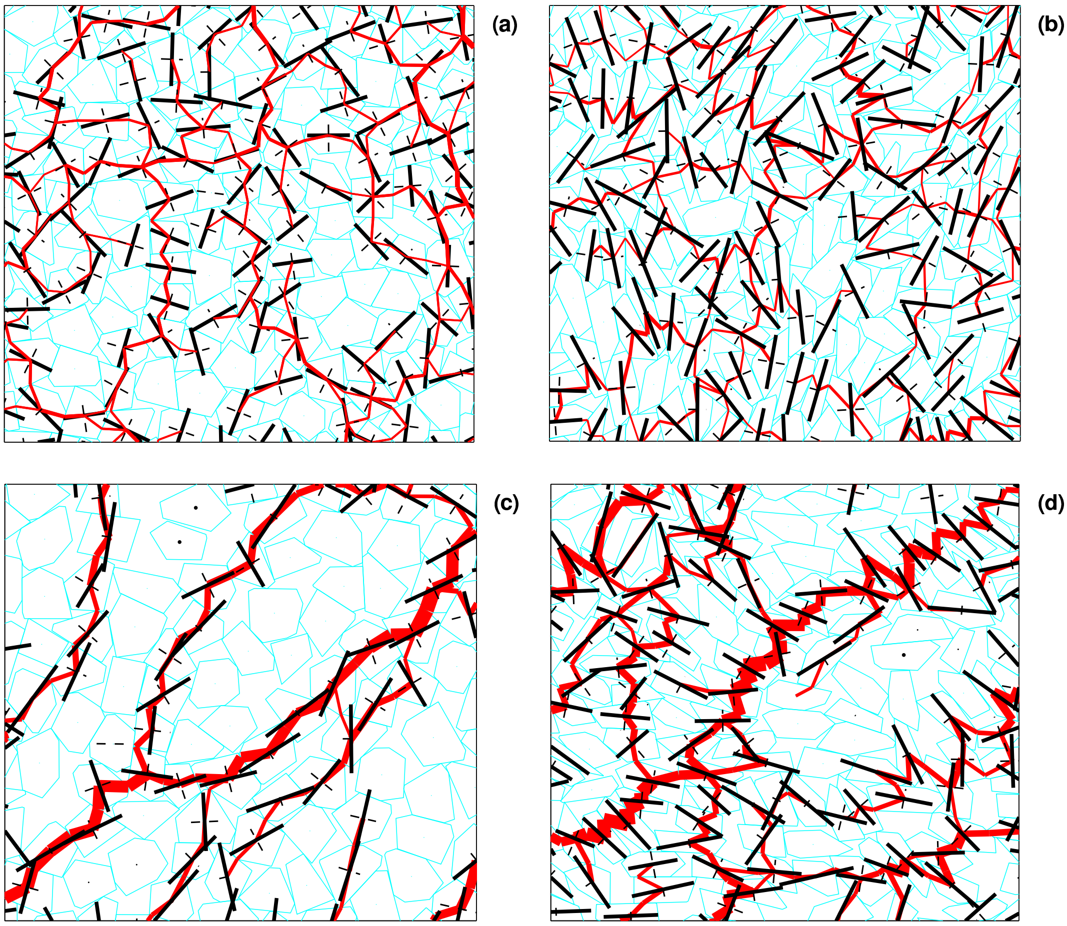

Figure 4.19: Force chains (light lines, thickness proportional to magnitude) and principal axes of the fabric tensor (black lines), for initial configuration (a,b) and the steady state (c,d), for isotropic λ = 1.0 (a,c) and elongated particles λ = 2.3 (b,d).

sotropic particles, the contact forces larger than the mean value and the principal axes of the fabric tensor of the corresponding particles are plotted in Figure 4.19. This is done for both types of polygons, and for the initial configuration and a snapshot in the steady state. In Figure 4.19(a), where the initial configuration of isotropic particles is shown, one can observe that the major principal axis of the fabric tensor of each particle F^p_M is oriented independently of the orientation of the force chains. In the system with elongated particles, however, F^p_M is slightly oriented in the largest dimension of the particles (major principal axis of the tensor of inertia of each particle i^p_M).

In the stationary state, we notice that in the system with isotropic particles F^p_M approximately follows the direction of the force chains that carry the larger forces. In the one with elongated particles, on the contrary, F^p_M is oriented in the direction of the largest dimension of the particles i^p_M. The orientation of the elongated particles within the main force chains is associated to the stability of the packing. That is to say; forces are transmitted in direction of the minor principal axis of the inertia tensor of each particle i^p_m, and therefore the contact points lie on flat surfaces which give a more stable configuration to the system. We conclude then that the orientation of the contacts in the steady state, in the case of non-spherical particles is governed by the particle orientation, and for isotropic particles by the direction of the major principal stress. This is also observed in Figure 4.18, where in the steady state for isotropic particles θ_F is almost the same as θ_σ, and for elongated particles θ_F is nearly θ_I.

Although the results presented in this section correspond to dense samples and one value of confining pressure, they are valid for different initial density states and stress levels as presented in Chapter 3, Sec. 3.3.1. In that chapter, we find in our simulations that the granular packings converge to the same critical state line independent of initial density state and stress level. These results validate in our MD simulations the existence of the so-called critical state in soil mechanics irrespective of any initial condition and particle shape characteristics.

4.3.4 Shear localization and particle rotation

In order to study strain localization and particle rotation, the shear cell is divided into horizontal layers, i.e parallel to the shear direction. For a clearer presentation of the results, we normalize the vertical dimensions with the height of the system h. The origin corresponds to the bottom and 1 to the top of the sample. We use in our analysis the rotation that particles accumulate during every unit increment ($\Delta\gamma_{unit}$) of the strain variable γ in the steady state (in our experiment we take $\gamma_{initial}$ = 10 and γ_{final} = 35, i.e. in total 25 $\Delta\gamma_{unit}$). Then, we average this accumulated particle rotation for each layer of the system, and for all the considered strain increments.

In Figure 4.20, the average accumulated rotation in the steady state for each layer and a shear rate $\dot{\gamma} = 1.4$ s^{-1} for isotropic and elongated particles is shown. We observe a clear localization of rotations, having a peak close to the center and decreasing toward the boundaries. This distribution resembles the movement of two rigid bodies against each other on a shear band. We calculated the variance of the data in order to quantify

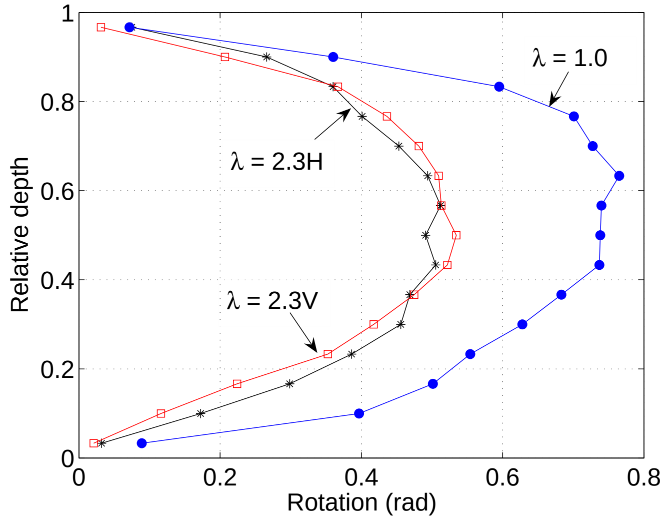

Figure 4.20: Average accumulated rotation of the particles during the steady state within horizontal layers as a function of relative depth. Isotropic particles λ = 1.0 (full dots), elongated particles λ = 2.3 V (open squares) and λ = 2.3 H (asterisks).

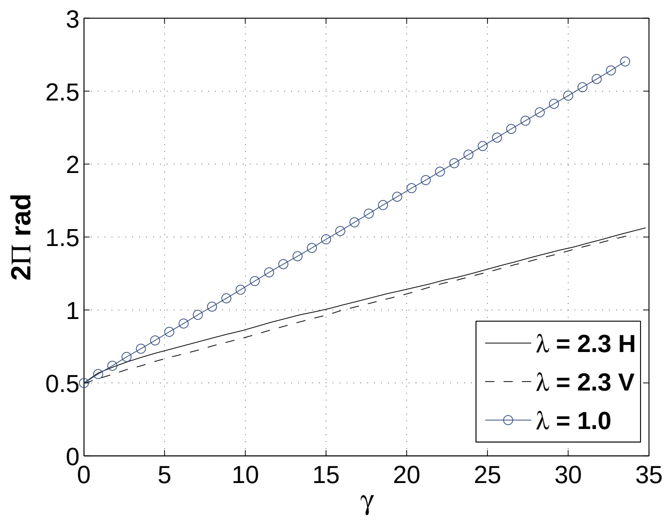

Figure 4.21: Mean accumulated rotation since the beginning of the simulation for isotropic particles λ = 1.0 (light line), and elongated particles (λ = 2.3) initially oriented in horizontal direction (H, black line), and in vertical direction (V, black-dashed line).

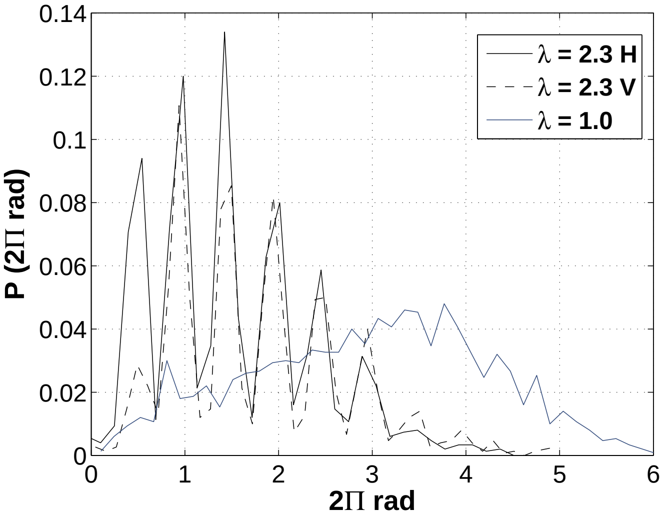

Figure 4.22: Probability distribution function of accumulated rotation since the beginning of the simulation until γ = 35, for isotropic particles (λ = 1.0, light line), and elongated particles (λ = 2.3) initially oriented in horizontal direction (black line), and in vertical direction (black-dashed line).

the localization of rotation. We obtained for the case of anisotropic particles 0.024 and 0.0303 (samples 2.3H and 2.3V, respectively), and 0.052 for isotropic ones. We were also interested in the width of the shear zone, which we define here as the width of the distribution with particle rotation larger than 80 % of the maximum rotation. We found in this analysis two important differences between the two types of particles considered:

- The accumulation of rotation is stronger for isotropic than for elongated particles. In this particular case the rotation of elongated polygons is only the 65 % of the isotropic ones. This is also stressed by the variance of the data.
- The width of the localization zone is smaller for elongated particles (around 0.45 times the system height h for elongated and 0.55 times h for isotropic particles).

These differences in accumulated rotation and relative width between isotropic and elongated particles can be explained by the frustration of movement and rotation that elongated particles experience due to the stronger interlocking among them. In this way, the localization zone (rotation zone) for elongated polygons becomes thinner than for isotropic ones. In Figure 4.21 the mean accumulated rotation since the beginning of the simulation for isotropic and elongated particles is depicted. Notice that the mean rotation is almost twice for isotropic than for elongated particles at the end of the simulation. We also calculate the probability distribution function of particle rotation, which is shown in Figure 4.22 for both isotropic and elongated particles and γ = 35. For isotropic particles a more uniform distribution is observed, and the maximum value is close to four complete rotations (a complete rotation $2\pi\ rad$). For elongated particles the probability distribution function presents several peaks every half of rotation ($\pi\ rad$). This fact indicates the strong frustration of rotation that such particles undergo during shearing, and that the typical mode of accumulating rotation is then every half complete rotation.

4.3.5 Influence of anisotropic particle shape on the critical state parameters and particle rotation

In this section, we study the influence of anisotropic shape on the parameters that the granular packings attain at the critical state. We consider dense samples with elongated particles initially oriented in the vertical direction and with the aspect ratios $\lambda = 1.0$, 1.5, 2.3, 3.0 and 4.0. The confining pressure p_0 is kept constant at 16 kN/m, and the shear rate $\dot{\gamma} = 1.4\ \mathrm{s}^{-1}$. The material parameters of the simulations are the same of the previous sections.

In Figure 4.23 we present the average values of the macro and micro-mechanical parameters for the different aspect ratio at the critical state. We consider the ratio between the shear and normal force F_s/F_n, the void ratio e, the coordination number Z, the deviatoric component $F_{yy} - F_{xx}$ of the fabric tensor $\mathbf{F}$, the deviatoric component $I_{yy} - I_{xx}$ of the inertia tensor $\mathbf{I}$, and the mean accumulated rotation of the particles $\langle\Theta\rangle$. The data correspond to the average of the variables once the critical state has been reached. The standard deviation is also presented. Furthermore, the evolution of the deviatoric components $F_{yy} - F_{xx}$ and $I_{yy} - I_{xx}$ with shear strain γ is shown in Fig. 4.24. From Figures 4.23 and 4.24 we conclude the following:

- The larger the anisotropy of particle shape λ, the larger the strength of the material at the critical state (Fig. 4.23a).
- The larger the anisotropy of particle shape λ, the larger the void ratio at the critical state and, therefore, the larger the volumetric deformation (Fig. 4.23b).
- For $\lambda \leq 2.3$ the larger the anisotropy of particle shape λ, the larger the coordination number Z of the particles. For $\lambda > 2.3$ the Z value saturates and remains constant (Fig. 4.23c).
- The larger the anisotropy of particle shape λ, the larger the fabric anisotropy at the critical state (Fig. 4.23d).
- The larger the anisotropy of particle shape λ, the larger the anisotropy related to particle orientation at the critical state (Fig. 4.23e).
- The larger the anisotropy of particle shape λ, the smaller the accumulated mean particle rotation angle $\langle\Theta\rangle$ (Fig. 4.23f).
- The larger the anisotropy of particle shape λ, the longer the time to reach micro-mechanical equilibrium in fabric and particle orientation (Fig. 4.24).

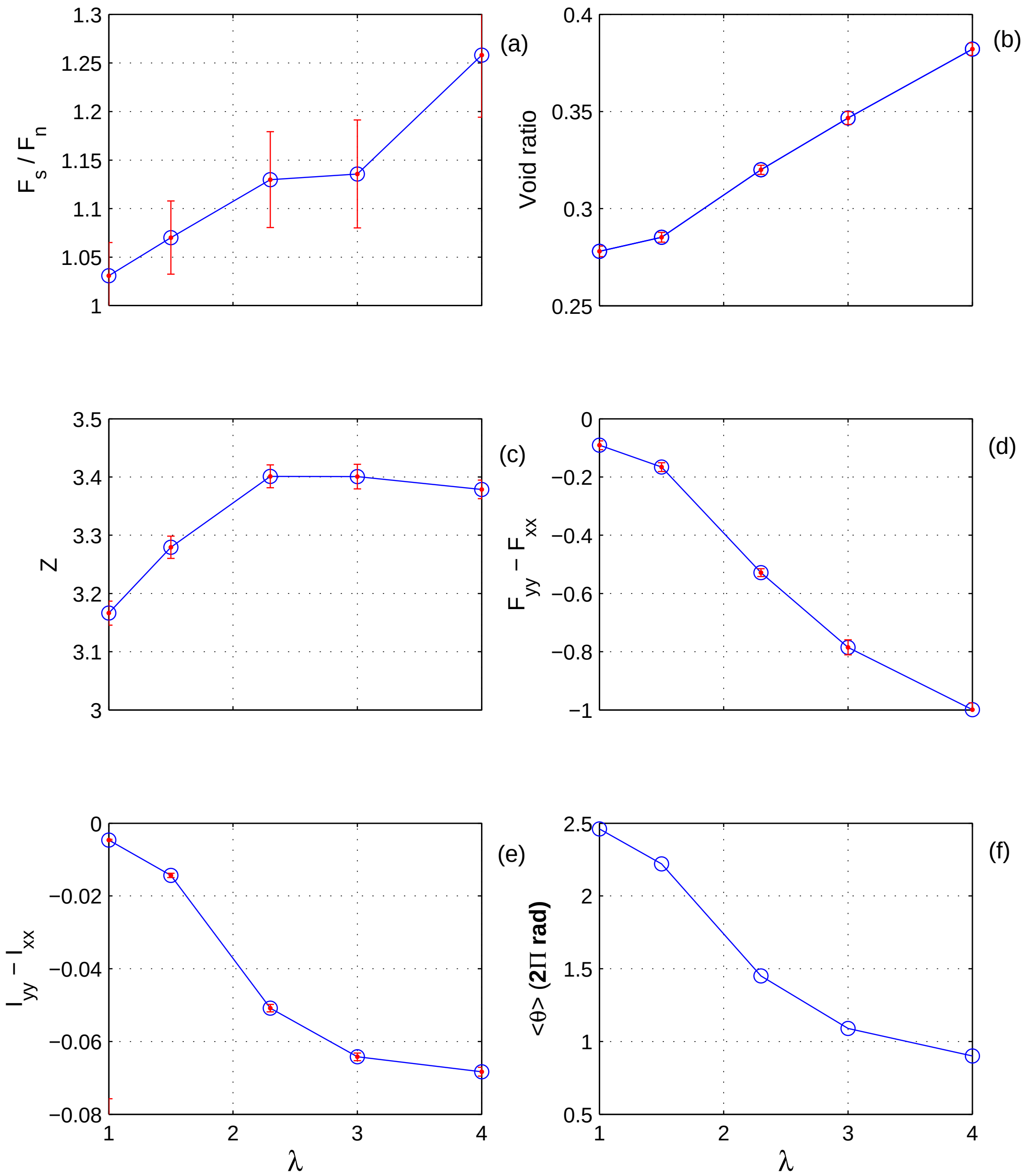

Figure 4.23: Effect of particle shape on the critical state values attained by the granular packings on shear cell tests, (a) ratio shear - normal force F_s/F_n, (b) Void ratio, (c) coordination number Z, (d) deviatoric fabric $F_{yy}-F_{xx}$, (e) deviatoric inertia $I_{yy}-I_{xx}$ and, (f) mean accumulated rotation $\langle\Theta\rangle$ of the particles since the beginning of the simulation till a shear strain $\gamma = 30$. The following aspect ratio λ are used: 1.0, 1.5, 2.3, 3.0 and 4.0. The shear rate $\dot{\gamma} = 1.4$ s^{-1}. The error bars correspond to 1 standard deviation of the analyzed data.

The above statements concerning the influence of anisotropic particle shape on the macro-mechanical behavior of granular packings, namely larger mobilized shear strength and more sensitivity to volumetric changes (dilatancy) with the increment of the aspect ratio λ, are explained in terms of the bigger interlocking among particles and the strong frustration of rotation that such particles undergo during shearing. Particle rotation is further hindered by the larger coordination number that anisotropic particles develop due to the larger relative flat surface. The last contribution to the macro-mechanical observations is the larger structural anisotropy (fabric) attained by the anisotropic systems at the critical state. This fabric anisotropy is directly related to the orientation of

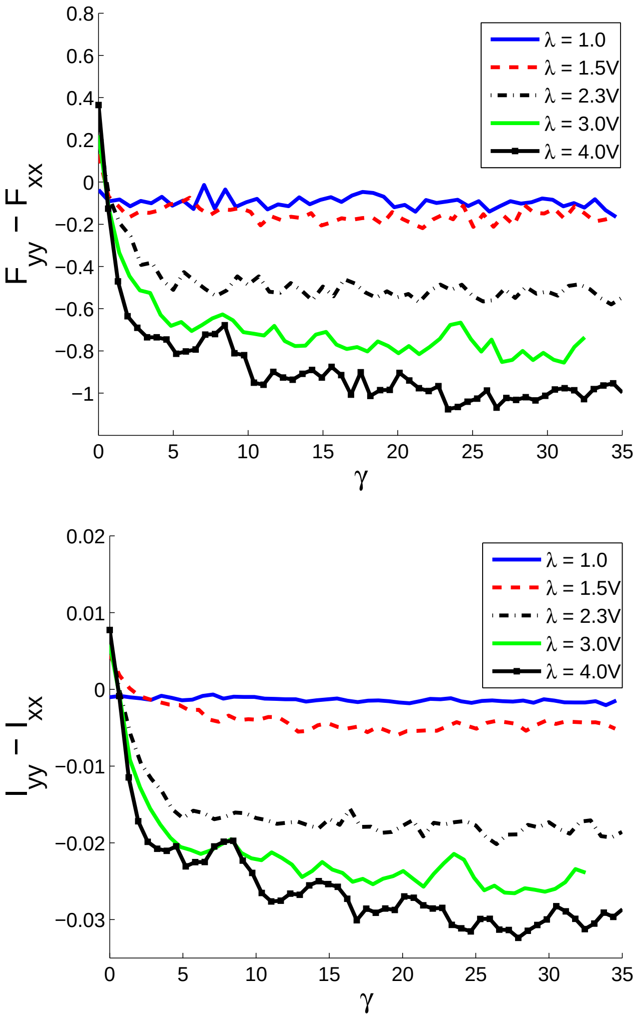

Figure 4.24: Evolution of the deviatoric component of the (a) fabric tensor **F** and (b) inertia tensor **I** for isotropic particles ($\lambda = 1.0$), and elongated particles ($\lambda > 1.0$). Samples with anisotropic particles are initially oriented in vertical direction (V).

anisotropic particles as presented in the previous sections.

4.4 Concluding remarks

In this chapter, we investigate the influence of particle shape on the final configuration of granular packings after isotropic compression, and specially on the mechanical behavior of sheared granular media. Our results show the significant influence of particle anisotropy on both the macro and micro-mechanical behavior of the granular samples.

Concerning the density and coordination number of the packing after the isotropic compression, we found that the value of void ratio e increases with the anisotropy of particle shape λ. The difference between the limit values of the void ratio e_{mix} and e_{max} also increases with λ. This volumetric behavior is well fitted by a linear expression, similar to previous experimental results [19]. The coordination number also increases with λ, but it saturates to a constant value for $\lambda > 3$. For anisotropic particles the direction along which they are initially stretched, has no influence in the final density state and coordination number. Regarding the anisotropy of the fabric and orientation of non-spherical particles, we found that the parameter controlling the final mean orientation of the particles as well as the fabric of the assembly is the direction along the anisotropic particles are initially distorted. These observations are independent of the final density state of the sample. A good correlation between particle orientation and the direction in which contacts are generated is observed.

During biaxial compression, we observed that contrary to isotropic particles, the anisotropic samples continued dilating and do not reach a stationary value of void ratio e and therefore do not attain the critical state. We explain this macro-mechanical evidence, by looking at the micro-mechanical evolution of the systems. For instance, the coordination number Z which is found to be the first signal when the isotropic systems approach the stationary state, in the case of anisotropic particles it does not converge to a stationary value. Following the evolution of anisotropic particles orientations, we find that these particles are reoriented during the shear process without attaining a steady state. Thus, the contact network for anisotropic particles does not reach a stationary state either. These micro-mechanical facts, concerning the non-stationary state of the fabric and particle orientation, do not permit the systems to reach the critical state.

Since anisotropic samples do not attain a stationary state, we analyze the mechanical properties related to the peak strength of dense samples. We find that anisotropic samples with a stable configuration relative to the direction of loading, i.e., particles oriented perpendicular to it, developed a higher shear strength ϕ_{peak} than isotropic samples irrespective of the induced fabric anisotropy. Anisotropic samples with unstable structure deform towards a more stable configuration and develop similar strength to the one of isotropic samples. In general, anisotropic samples before reaching the peak undergo smaller fabric changes than isotropic samples due to the stronger interlocking and preferential orientation of particles. The peak strength of the samples is related to the dilatancy rate and to the breakage of interlocking between the particles to reduce the coordination number. A very good relationship between peak strength, dilatancy rate and coordination number is observed.

In the shear cell tests, we found that for samples with isotropic and elongated particles the shear force and volumetric strain saturate at constant values reaching a steady state. These values in the case of elongated particles are higher than for isotropic particles due to the stronger interlocking between anisotropic particles. Furthermore, samples with anisotropic particles reach the same saturation value in the steady state independently of the initial orientation of the particles. This is related to the removal and reorientation of the initial inherent anisotropy (fabric and particle orientations) in the direction of the induced shear. The previous conclusion was confirmed by studying the evolution of the fabric and the inertia tensors.

The deviatoric part and the quotient of the principal components of the fabric tensor **F** and the inertia inertia **I**, for both types of particles, reach a stationary value independent of their initial one. This is directly related to the steady state at the macro-mechanical level. The principal directions of **F** and **I** present the following behavior: in the initial state of the samples, isotropic polygons exhibit no preferred direction of contacts, however, in the case of elongated polygons the major principal component of **F** is oriented along the direction of the major principal component of **I**. In the steady state, and for isotropic particles the major principal component F_M is reoriented in the direction of the major component of the stress tensor σ, but for elongated particles F_M evolve following the induced orientation that particles undergo during shearing. The direction of the major component of σ is the same for both particle shapes. Independently of the initial orientation, samples with elongated particles reach the same contact θ_F and particle θ_I global orientation in the steady state. One can then conclude that a stationary value of the principal components and principal directions of the fabric and inertia tensors is a micro-mechanical requirement for the existence of the global steady state of the medium. We also concluded that for isotropic particles the contact orientation in the global stationary state is governed by the direction of the major principal component of the stress tensor, and for elongated particles mainly by the major principal component of the inertia tensor (particle orientation).

At the particle level, these results are clearly understood by studying the inertia tensor and the fabric tensor of the particles within the force chains carrying the larger forces. We find that the orientation of elongated particles is associated to the stability of the packing, i.e. forces are transmitted through contacts parallel to the shortest dimension of the particles i_m^p.

Concerning strain localization and particle rotation we observe that the width of the shear zone and the accumulated rotation is larger for isotropic particles than for elongated particles. This result can be explained by the frustration of rotation that elongated particles experience due to the stronger interlocking among them, and it is clearly observed in the probability distribution function of the angle that particles have rotated during shear. The typical mode of accumulating rotation for elongated particles is every $\pi\ rad$.

Based on the results of our MD simulations presented in Chapters 3 and 4, the existence and uniqueness of the critical state in soil mechanics is validated, and it is found to be independent of any stress-density initial condition and of any particle shape characteristics. Finally, by varying the aspect ratio λ of the particles, we can state the following conclusions regarding the micro and macro-mechanical parameter that granular packings attain at the critical state. The larger the anisotropy of the particles λ:

- The larger the strength of the material at the critical state.
- The larger the void ratio at the critical state and, therefore, the larger the volumetric deformation.
- The larger the coordination number Z of the particles. For $\lambda > 2.3$ the Z value saturates and remains constant.
- The larger the fabric anisotropy at the critical state.
- The larger the anisotropy related to particle orientation at the critical state.
- The smaller the accumulated mean particle rotation angle $\langle\Theta\rangle$.
- The longer the time to reach micro-mechanical equilibrium in fabric and particle orientation.

Chapter 5

Avalanches in periodic shear cells

Natural earthquakes are one of the most catastrophic events in nature [50, 125] with deep social implications, in terms of human casualties and economic loss [125]. Considerable efforts have been made to understand the earthquake dynamics and the underlaying mechanisms prior to the occurrence of the events [126–129]. In particular, the study of earthquake faults-both experimentally [130–132] and through particle based numerical models [37, 42, 43, 81]-have received special attention.

In most of the existing numerical models of earthquake fault the gouge is represented by discs [42, 81] or spheres [29]. The dynamics of such material within the fault is thought to control the stick-slip instability that characterizes earthquake process. An understanding of its properties is, therefore, vital to understand earthquake dynamics [49]. For instance, the existence of the gouge within the fault has been proposed to explain the low dissipation on shear zones and this explained the heat flow paradox [133]. In this case, the reduction of the macroscopic friction and consequently, the heat generation is attributed to the deformational patterns such as rolling of particles [42, 81]. In laboratory experiments by Maron [130], the influence of particle characteristics has also been studied. They found that frictional strength and stability of the granular shear zone is influenced by particle shape, size distribution and their evolution through particle crushing. Modeling of fault gouges, therefore, must include different grain characteristics.

In this chapter, we use our model of polygonal particles [39, 48] to mimic the relative movement of two tectonic plates with transform boundaries, i.e. the boundaries are parallel to the direction along which the tectonic plates move [50, 51]. Although similar to the work performed by Tillemans et al. [37], our model considers *anisotropic* particle shape. The response of the system is characterized by discrete events or avalanches whose size covers many orders of magnitude, similar to the so-called crackling noise of physical systems [52]. We find that the magnitude of the avalanches is independent of particle shape and in good agreement with the Gutenberg-Richter law describing the distribution of magnitudes for natural earthquakes [53]. We also obtain a power law behavior for the waiting times of aftershocks sequences similar to the Omori's law [54] that states that the rate of events after the main shock decrease with the inverse of time. We obtain an exponent for the time decay that is dependent on the initial sample configuration and therefore on the particle shape. From this result, we will conclude that by studying the avalanche sequences it is possible to identify at the macro-mechanical level the presence of anisotropic particles within the gouge. Further, we argue that the existence of this anisotropic gouge in fault zones might also explain the variation of the decay of the aftershock sequences observed in nature. For a given stiffness value and mobilized frictional strength, we also computed the conditional probability for an avalanche to occur, and found that it decreases logarithmically with the stiffness. This logarithmic decay depends on particle shape. Concerning frictional strength, anisotropic samples are able to mobilize higher strength than the isotropic samples. For a given value of mobilized strength anisotropic samples also exhibit lower probability of failure. Finally, we propose some microstructure features that could be related and can potentially explain the occurrence of avalanches.

This chapter is organized as follows. In Section 5.1, we present the basic fundamentals of plate tectonics. The details of the movement of tectonic plates in our simulations are described in Sec. 5.2. In Sec. 5.3 we characterize and study the system response. In Secs. 5.4 and 5.5 we address the influence of particle anisotropy on the frequency distribution of avalanches and on the width of the time interval where aftershocks occur. The weakening and stability of the system is investigated in Sec. 5.6, and in Sec. 5.7 the main conclusions and perspectives for avalanche precursors are discussed.

5.1 Plate tectonics

The relative motion of tectonic plates is directly related to the occurrence of natural earthquakes [50, 51, 134]. The tectonic plate theory [135] was scientifically accepted during late 1960's, and could explain many geological processes, such as volcanic activity, mountain-building, among others [51]. The outer shell of the earth-the lithosphere-is broke up into the tectonic plates. The lithosphere lies above the asthenosphere. Although the asthenosphere is rigid, it can flow on geological time scales because of the high temperature of the layer. The forces driving the tectonic motion are then due to: (i) sinking of tectonic plates into subduction zones due to the higher density of the lithosphere compared to the asthenosphere, and (ii) convection currents moving the lithosphere [50, 51, 134].

The relative motion of the tectonic plates produces stress accumulation at their boundaries, in such a way that it is released afterwards in strain generating displacements on the surface. From the distribution of the tectonic plates and the records of earthquakes epicenters between 1963-1998 [137], we observe that the location of the epicenters clearly define the boundary of the tectonic plates (see Fig. 5.1).

Depending on the relative motion of the tectonic plates, there are three possible boundaries: (i) extensional or divergent, (ii) compressional or convergent (subduction zone) and (iii) transform boundaries. They are sketched in Fig. 5.2. In the transform boundaries, tectonic plates move in the opposite directions shearing the material within the boundary. Because of the simplicity of the transform boundary, we are able to mimic its behavior in our MD simulations. One of the most well known examples of this type of boundary is the San Andres Fault in California where the Pacific plate and the North American plate are moving in opposite directions. In this particular case, the relative motion of the plates is about 40 mm/year, and thus the strain accumulation rate is around $3 \cdot 10^{-7}$ per year [139].

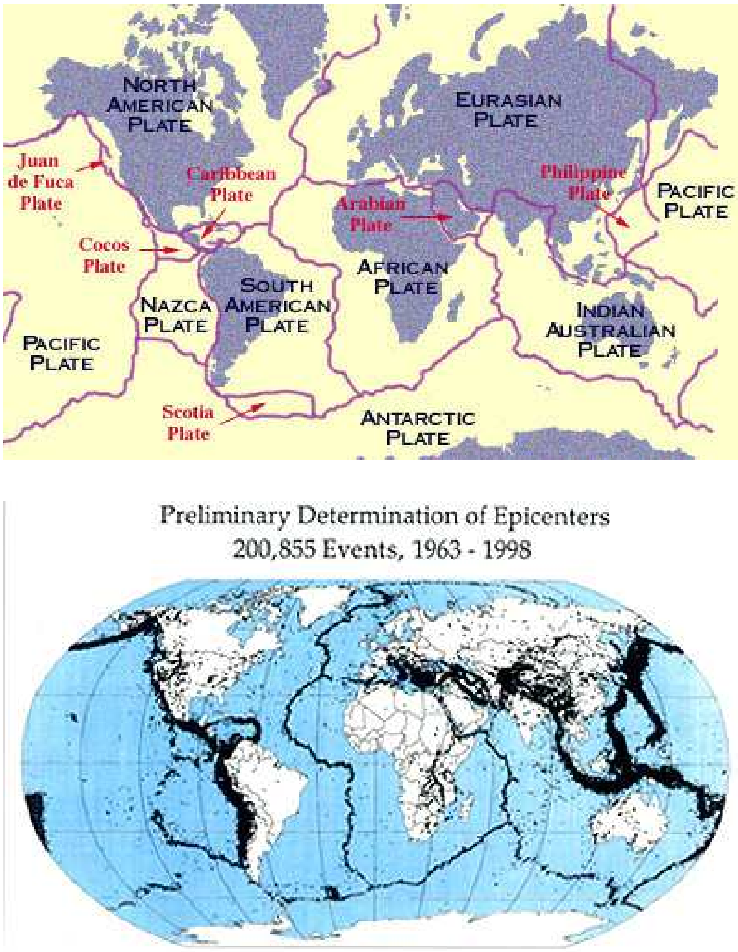

Figure 5.1: Earth's tectonic plates according to plate tectonics theory [51] (picture taken from NASA's observatorium [136]) and preliminary earthquake epicenters from 1963-1998, NASA records [137].

5.2 Generation of samples and numerical experiment

In this chapter we use samples with isotropic and anisotropic particles to study the influence of particle shape on the mechanical behavior of packing sheared by a very low shear rate. The random generation of the particles is done by means of a Voronoi tessellation as explained in Sec. 2.4. The polygons are nearly isotropic and are obtained from a regular square lattice. By distorting the square lattice in the horizontal and vertical directions, we end up with anisotropic or elongated particles. The ratio between the stretching and contracting factors gives us the average aspect ratio λ of the polygons, that is used to characterize the anisotropic shape of the particles.

In Figure 5.3 the different initial configurations are shown. The isotropic configuration is depicted in Fig. 5.3a, and the anisotropic ones in Fig. 5.3b for particles stretched in the

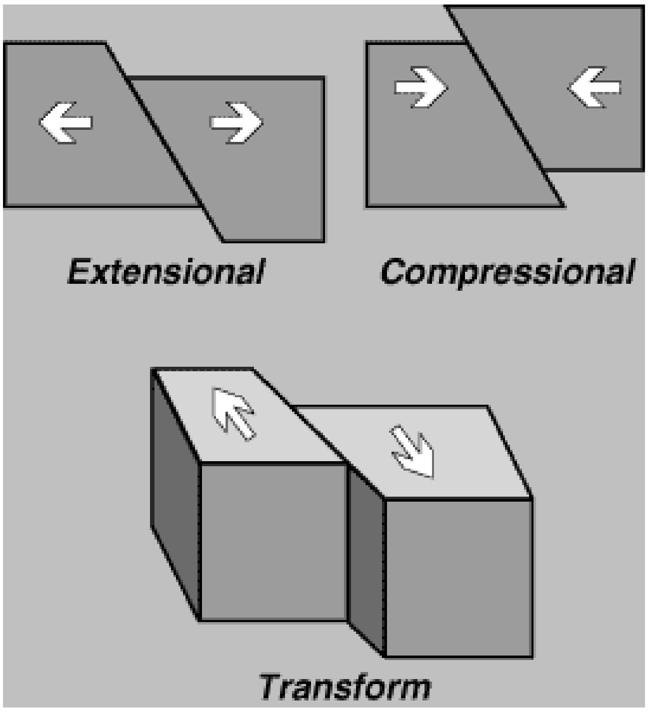

Figure 5.2: Types of plate boundaries: extensional or spreading, compression or collisional and transform boundaries. Picture taken from Nevada seismological laboratory [138].

same direction of shearing (horizontal direction, sample H) and in Fig. 5.3c for particles stretched perpendicular to shear direction (vertical direction, sample V). The shape of the anisotropic particles is characterized by λ the aspect ratio between the length of the longest and the shortest axis of the particles.

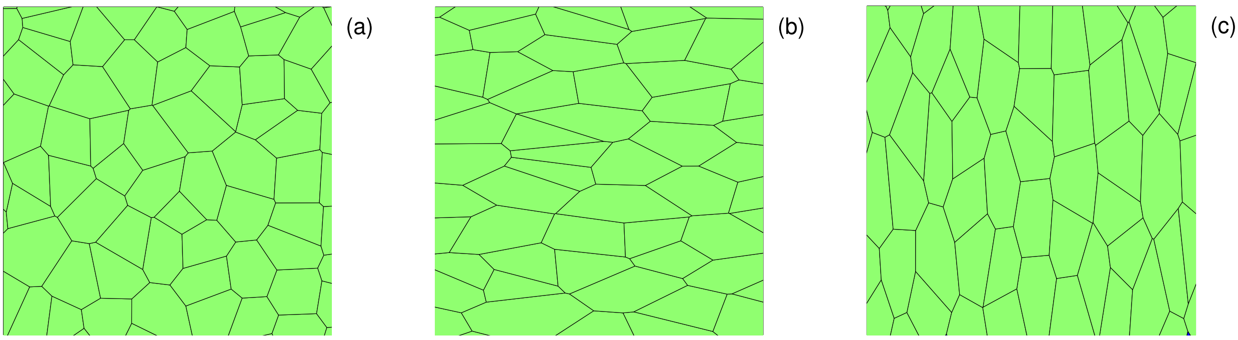

Figure 5.3: Samples for the numerical simulations: isotropic polygons (λ = 1.0) (a), and elongated polygons (λ = 2.3) stretched in horizontal direction H (b) and in vertical direction V (c).

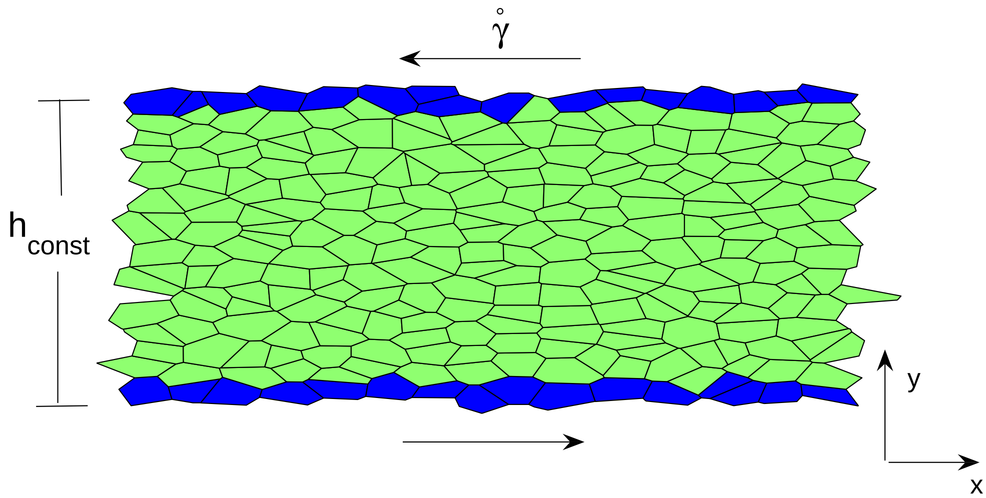

Figure 5.4: Sketch of the shear cell. The system is not allowed to dilate (h_{const} fixed). The sample is sheared using a constant shear rate $\dot{\gamma}$. Dark particles (blue in color) induce shear to the sample.

We use samples of two different sizes, with 256 (16×16) and 1024 (32×32) particles. Periodic boundary conditions are imposed in horizontal direction. The top and bottom have fixed boundary conditions. The volumetric strain of the media is suppressed (position of walls fixed, no dilation). The top and bottom layers of the particles are moved in opposite directions so as to impose a constant shear rate $\dot{\gamma}$. The particles in these layers are not allowed to rotate or move against each other. In Fig. 5.4 a setup of the shear cell is presented for the anisotropic sample $\lambda = 2.3H$. The strain variable γ is defined as:

$$\gamma = D_x/h_{const}, \tag{5.1}$$

where D_x is the horizontal displacement of the boundary particles and h_{const} is the height of the sample. The horizontal and vertical directions are indicated as x and y, respectively. In our simple model, polygons represent rocks between two tectonic plates i.e. the gouge. The top and bottom boundary particles represent the tectonic plates. We start from a perfectly packed configuration in order to represent the initial state of the material that is supposed to be intact prior the shear process.

As described in the previous section, the value of the strain rate is of the order of 10^{-7} per year ($\approx 10^{-14}$ s^{-1}). For our numerical simulation, this value of shearing is computationally too expensive. For instance, for $\Delta t = 1s$, 10^{12} iterations are needed to induce a shear strain of 1%. Using a system of 16x16 particles, 10^{12} iterations would require roughly 1000 years of CPU time in a standard P-IV PC. To overcome this, we choose a suitable shear rate at which the motion of the system is intermittent, i.e. in some stages the system is locked and deform steadily accruing elastic strain and in others stages the stored energy at the contacts is suddenly released. We monitor the evolution of the system using its kinetic energy as shown in Fig. 5.5. Another important issue is to obtain events spanning several orders of magnitude to study their distribution. We test shear rates in the range $10^1 - 10^{-7}$ s^{-1}. The value of shear rate found suitable for the above purpose is of the order of 10^{-5} s^{-1}.

To perform the MD simulations using the selected shear rate, we adjust the parameters of the model in order to obtain a time step Δt requiring a reasonable CPU time. We use the following parameter values: normal stiffness $k_n = 400$ N/m, $\epsilon_n = 0.9875$, $\mu = 0.5$, $k_t/k_n = 1/3$, $\nu_t/\nu_n = k_t/k_n$, and $\epsilon_t/\epsilon_n = 1.0053$. We select a time step Δt of 0.005 s. We use three different interparticle friction coefficients $\mu = 0.0, 0.5, 5.0$ and shear rate $\dot{\gamma} = 1.25 \cdot 10^{-5}$ s^{-1}.

5.3 System response: monitoring avalanches

The motion of the particles in the interior of the sample is not continuous, but has a "stick-slip character". During slip a sudden rearrangement of the medium arises as a consequence of the large relative displacements of the particles. We monitor this rearrangement of the system through its kinetic energy E_k. As shown in Fig. 5.5, the system can be in two different states. In the "stationary state", E_k is approximately equal and

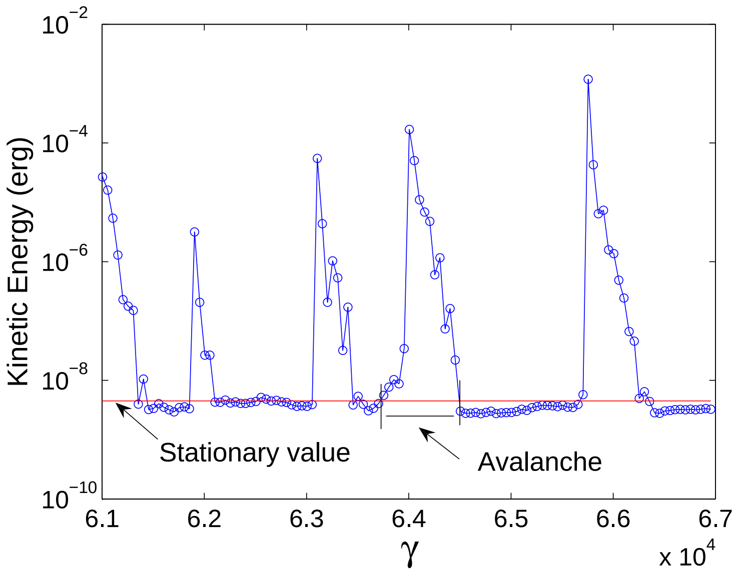

Figure 5.5: The average kinetic energy in logarithmic scale versus the shear strain γ. The stationary value E_k^0 of the kinetic energy is obtained from the velocity profile of the particles at the steady state. The released energy of the avalanches are calculated using Eq. 5.2.

less than a low value E_k^0, shown by the horizontal line in Fig. 5.5. This value E_k^0 is associated with the accumulation of elastic strain under the imposed shear. The low energy state E_k^0 is punctuated by a series of events where kinetic energy rises several orders of magnitude above E_k^0. These are the avalanches. An avalanche begins when E_k rises above E_k^0, and all subsequent values of E_k greater than E_k^0 are considered to be part of the same avalanche.

The total released energy E_r of one avalanche is the sum over the total number N of consecutive values of E_k above the stationary state, namely

$$E_r = \sum_{j=1}^{N} E_k^j. \tag{5.2}$$

In this 'stationary state' the system is deforming steadily and accumulating energy at the particles contacts. This state can be characterized by the value E_k^0 obtained from the average velocity profile of the particles at this stage.

In the case of infinitely rigid particles, subtracting the 'stationary value' E_k^0 from the kinetic energy of the system, one would obtain a zero value of E_k between successive avalanches. Contrary to this previous scenario, our system is composed of soft elastic particles. Therefore, the energy introduced into the system through shearing is not only stored as elastic energy at the contacts but also transformed into translational and rotational movement of the elastic particles. If we subtract the 'stationary value' of kinetic energy from the E_k signal, we automatically obtain a non-zero value between the events. This non-zero value is a numerical artifact stemming from the calculation of the tangential contact forces, the soft elastic nature of the polygons, and the periodic boundary conditions that might trap some of the energy released during the avalanches. As presented in Chapter 6, this numerical noise related to the numerical convergence of the integration method would disappear using a more efficient algorithm and/or reducing the time step of the simulations [59], and also improving the boundary conditions as discussed in Section 5.7. This numerical noise, however, does not affect the results of this chapter.

The force needed to sustain the constant motion of the top and bottom layers can be measured in the simulation. In the following, F_s is the shear (horizontal) force applied to each wall, and F_n is the normal force. Figure 5.6 shows the occurrence of one avalanches and the associated strain accumulation for a system with 32×32 particles. We can see that the abrupt increment of kinetic energy of the system (Fig. 5.6a), matches with the fall-off of the strength of the material F_s/F_n (Fig. 5.6b).

Figures 5.6c and 5.6d illustrate two different representations of the same sample snapshot, immediately before the avalanche. Figure 5.6c shows the sample configuration and the rotation that the particles undergo for a shear band located at the center of the sample. The colors of the particles are given by their accumulated rotation: the lighter the color the bigger the accumulated rotation. Figure 5.6d shows the elastic strain at the contacts, which are represented by dark dots (red in color) with a diameter proportional to its strain value. Here, one can see that there is a strong localization of elastic strain along the shear band. This strain localization weakens the system and drives it to failure,

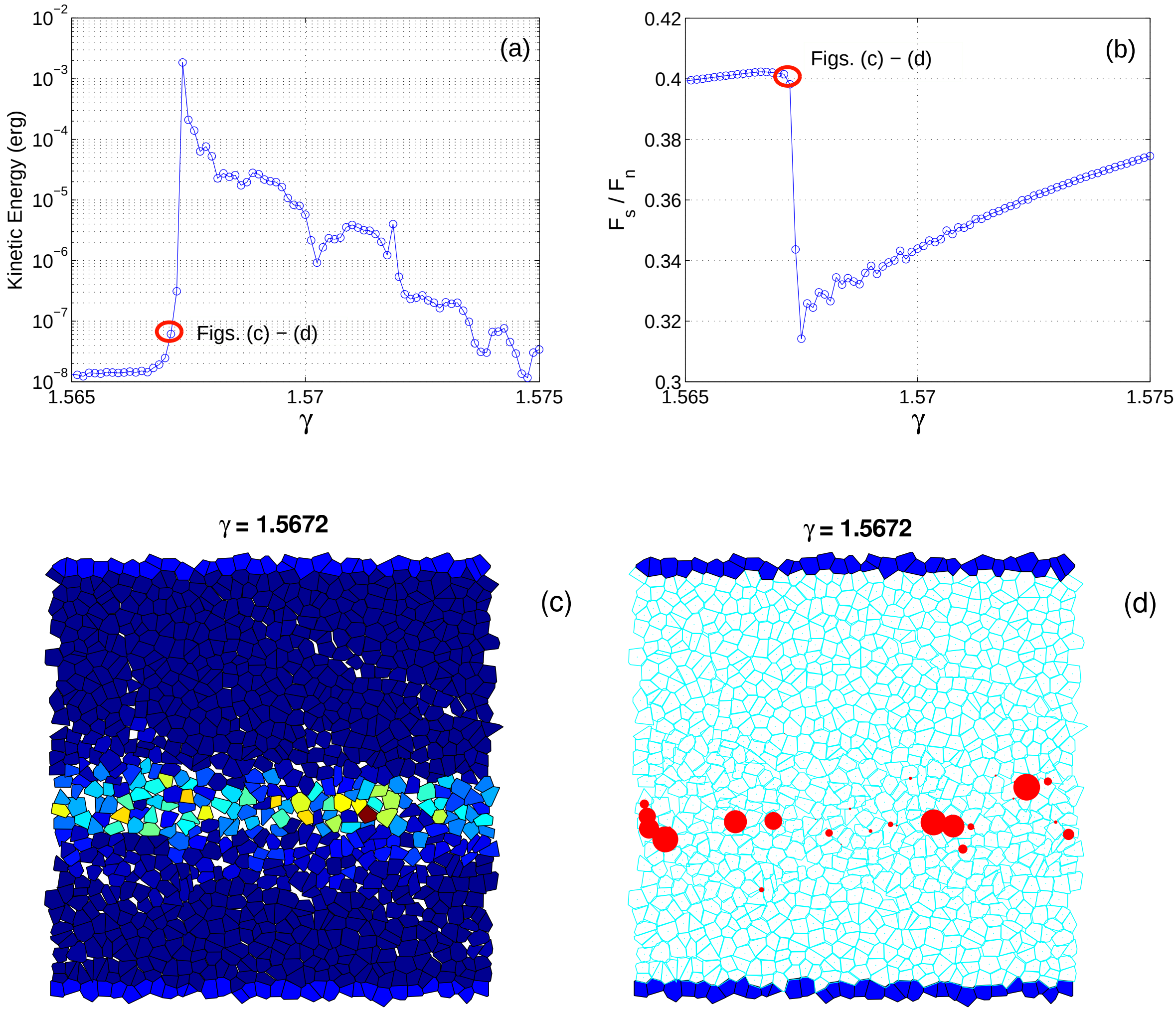

Figure 5.6: Accumulation of elastic strain and overcome of the strength of the material F_s/F_n prior to the occurrence of an avalanche. In (a) the kinetic energy of the system and (b) the ratio F_s/F_n showing the developed strength are presented, with circles indicating the strain value at which the snapshot in (c) and (d) are taken. (c) The configuration and accumulated particle rotation just before the avalanche. (d) The elastic strain at the contacts before the avalanche, where the diameter of the dark dots (red in color) is proportional to the value of the elastic strain. System size: 32×32 particles.

since it promotes the occurrence of the Coulomb limit condition related to the number of sliding contacts. In other words, the weakening of the system is due to both the strain localization and the increase of the ratio of sliding contacts.

During the avalanche the system suffers a complete rearrangement in which the old sliding contacts are removed from the sliding condition and new contacts are generated. This rearrangement marks the beginning of a new stage of elastic strain accumulation that drives the system to the next avalanche.

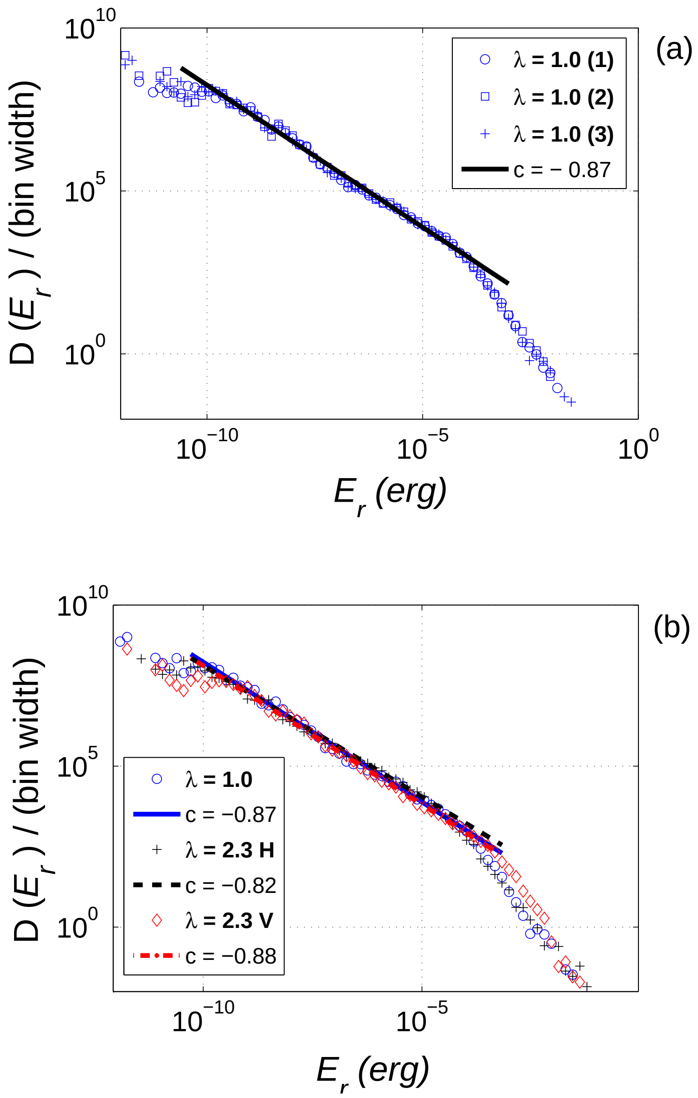

Figure 5.7: Log-log plot of the number of avalanches versus their released energy E_r for **(a)** different configurations of isotropic particles and **(b)** for different λ values. Here $\mu = 0.5$ and the system has 16×16 particles. Logarithmic binning is used.

5.4 The Gutenberg-Richter law in anisotropic granular media

The distribution of earthquake magnitude is described by the Gutenberg-Richter law [53]. This law states that the number n of earthquakes of magnitude greater than M is proportional to $n \sim 10^{-bM}$. Typically, the value of b is equal to 1 at most places, but may vary between 0.8 and 1.5 [140]. As we will see, the exponent b will be an invariant property describing the occurrence of avalanches associated with sudden rearrangements of

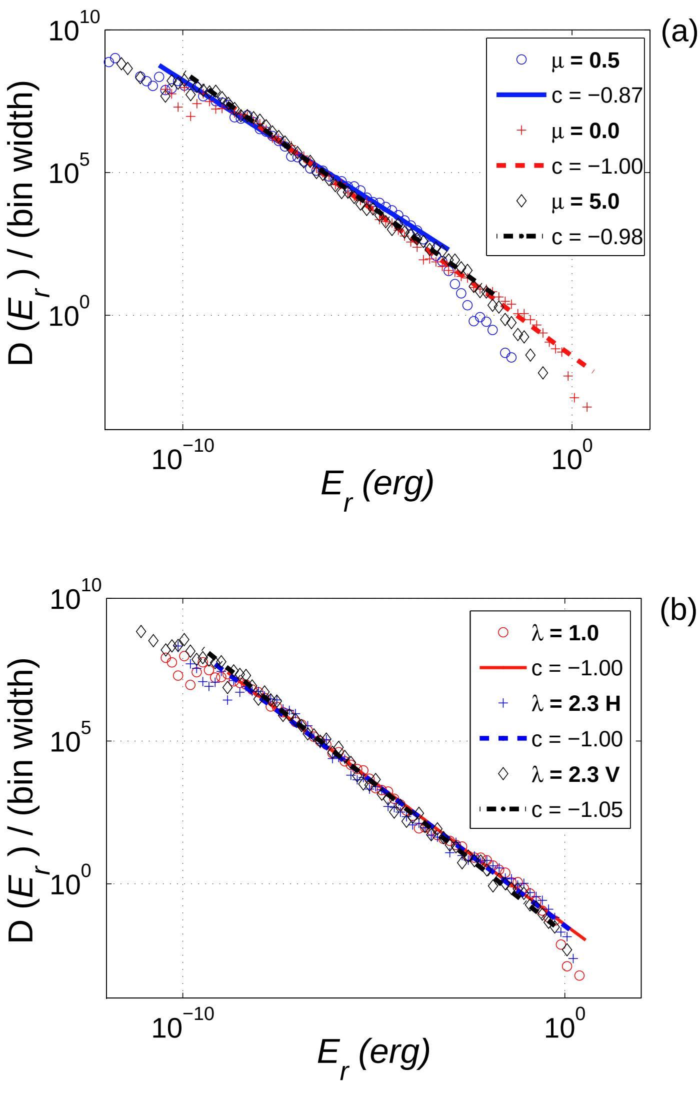

Figure 5.8: The distribution $D(E_r)$ of the released energy E_r when **(a)** varying interparticle friction coefficient μ with fixed $\lambda = 1$ and **(b)** when varying λ with fixed $\mu = 0$. The system has 16×16 particles and logarithmic binning is used.

granular media under very slow shear.

To this end, we study the possible influence of the formation and evolution of the shear band on the distribution $D(E_r)$ of the released energy E_r during an earthquake. Since the magnitude of an earthquake is defined as the logarithm of the released energy, apart proper constants one finds $n \sim E_r^{-c}$ being the exponent c approximately equal to 0.67 [134].

In Figure 5.7a we show the distribution $D(E_r)$ for three different initial configurations of isotropic samples, corresponding to different seeds for the Voronoi Tessellation. All the distributions collapse and show a power law behavior over almost six orders of magnitude with an exponent of $c = 0.87$ for the fitted straight line. Although the exponent c slightly deviates from the expected value of 0.67, the power law behavior is in good agreement with the Gutenberg-Richter law.

In Fig. 5.7b, the distributions for both isotropic and anisotropic particles are shown. Similarly, for all samples, the data sets are well fitted by a power law with an exponent c ranging from 0.82 to 0.89, indicating a weak influence of the particle shape on the distribution of the released energy. The power law holds over six orders of magnitude.

Similar exponents ($0.80 < c < 0.95$) are obtained for other system sizes in both isotropic and anisotropic cases and for the case when one considers the distribution for individual particles. From such results, one concludes that independent of the anisotropy there is a scale invariance of the system response according to the Gutenberg-Richter law.

We also study the influence of the friction coefficient μ. In Fig. 5.8a the distributions for the isotropic samples with different friction coefficients are plotted. The effect of friction in both cases is to slightly increase the exponent c, which holds for nearly seven orders of magnitude. The distributions for isotropic and anisotropic samples with $\mu = 0$ are presented in Fig. 5.8b where no influence of particle shape is observed.

5.5 Waiting times

Earthquakes usually occur as part of a sequence of events, in which the largest event is called the mainshock and the events prior and after the mainshock are foreshocks and aftershocks respectively [134]. The empirical Omori's law states that the number of aftershocks $n(t)$ reduces with the inverse of the time following,

$$n(t) = \frac{c}{(1+t)^p} \tag{5.3}$$

where c is an empirical constant and p is usually close to 1 but can vary between $0.7 - 1.5$ [134]. Before performing the calculation of waiting times of aftershocks in the system evolution, we have to define what we consider as a mainshock. We first select a time interval t, and calculate the magnitude M_i ($i = 1, .., N_t$) of the total number of events N_t within that interval. Then, we take the first event of the series as a mainshock and compare its magnitude M_1 with the next events. All the consecutive events with magnitude M_i having one order of magnitude smaller than the one of the mainshock are considered aftershocks and their waiting times are calculated. A new event is considered mainshock only when it is larger than $1/10$ of the magnitude of the current mainshock. When this happens the sequence of the previous mainshock is considered to be finished and a new sequence is calculated.

In Figure 5.9 the distribution of waiting times for isotropic and anisotropic systems with a size 16×16 particles are shown. All the numerical results can be fitted using the expression in Eq. (5.3). Thus, the temporal distribution of aftershocks in our model is also in agreement with the observations in nature. We obtain the following values for the exponent p: 1.57 for the isotropic sample $\lambda = 1.0$, 1.61 for the anisotropic sample $\lambda = 2.3$ V, and 0.83 for the anisotropic sample $\lambda = 2.3$ H. The decay for $\lambda = 1.0$ and $\lambda = 2.3$ V is faster than the decay in the sample $\lambda = 2.3$ H. This difference in the p value is directly related to the initial configuration of the samples.

Using this influence of the initial configuration of anisotropic samples on the stability of the system, we will next explain how to detect at the macro-mechanical level the presence of anisotropic particles within the gouge.

The anisotropic sample $\lambda = 2.3$ H with particles oriented parallel to the shear direction exhibits a more stable configuration. In this sample, the induced torque on the particles is minimized and the main deformation modes, sliding and rolling of the particles, are highly constraint for the fixed boundary conditions and no dilation in vertical direction. The hindrance of the deformation modes produces a larger temporal stability and also a larger mechanical stability. The larger temporal stability makes the occurrence of the events less frequent in time, i.e. slower decay of the waiting times. The larger mecha-

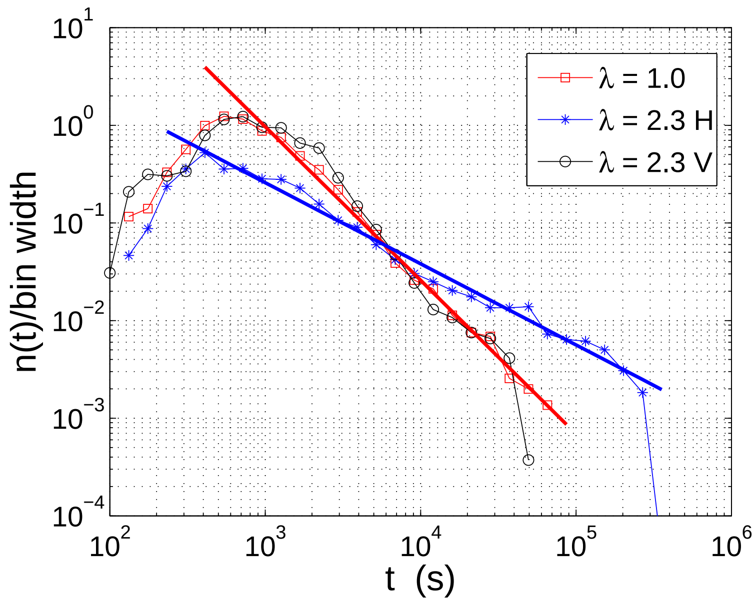

Figure 5.9: Distribution $n(t)$ of waiting times for the sequence of aftershocks in the numerical simulation. Isotropic sample $\lambda = 1.0$ and anisotropic samples $\lambda = 2.3$ are presented.

nical stability results in a smaller probability of failure for a given value of stiffness as presented in Sec. 5.6. On the contrary, the configuration of anisotropic samples $\lambda = 2.3$ V, with particles oriented perpendicular to the shear direction, maximizes the induced torque on the particles and results in a less stable configuration. This configuration yields smaller temporal and mechanical stability. The smaller temporal stability is observed in the decay of the waiting times, that is slightly faster than the one of the isotropic sample. The smaller mechanical stability of sample $\lambda = 2.3$ V is manifested in the larger probability of failure for a given value of stiffness compared to the other samples, see Sec. 5.6. Therefore, by looking at the decay rate of the aftershock sequences one might be able to explain the variation of the decay p in realistic earthquake sequences, and attribute its variation to the existence of anisotropic gouge in the fault zone.

It is important to say that for a more realistic representation of the earthquake process the crushing of particles should be taken into account. The absence of particle crushing will be discussed in Section 5.7.

5.6 Weakening and stability of the system

In this section we study the relationship between the occurrence of avalanches and the weakening of the system. The weakening process results from the release of energy due to previous accumulation of strain at the contact level and contacts reaching the sliding condition. In Figure 5.10 we show the relative number of sliding contacts n_s, the stored energy at the contacts E_{stored} and the total kinetic energy E_k for a system size of 16 x 16 particles. The relative number of sliding contacts is given by N_s/N_c, the ratio of sliding contacts to the total number of contacts. The stored elastic energy at the contacts E_{stored} is calculated as $1/2\ (k_n\delta^2 + k_t\xi^2)$. Here, k_n and k_t are the stiffnesses of the elastic springs in normal and tangential direction, and δ and ξ the corresponding elongation respectively. One can see in Fig. 5.10 that between the events, the relative number of sliding contacts increase with the shear strain, making the system weaker and indicating that the system is constantly accruing elastic energy at the contacts E_{stored}. The weakening of the system persists until failure, where the kinetic energy increases by several orders of magnitude. At this stage, the structure of the system is rearranged, the stored energy at the contacts is released (drops of E_{stored}), and the contacts are removed from the sliding condition. All the events in the kinetic energy are associated with both drops in the ratio n_s and drops in the stored energy.

At the macromechanical level the weakening of the system is observed by looking at the evolution of the shear stress with the shear strain (Fig. 5.11). After each stress drop the system experienced a rearrangement that removes the contacts from the sliding condition. This new configuration produces a temporal stability, in which the strength builds up. At this stage the system sticks and the accumulation of strain takes place. The stiffness of the system i.e. slope of the stress-strain curve $\Delta\tau/\Delta\gamma$ (Fig. 5.11) decreases with the strain accumulation and the increment of n_s. In this softening regime the system approaches failure and when the strength of the material is overcome, the system slips. One can observe clearly that the stick-slip behavior is associated with the permanent

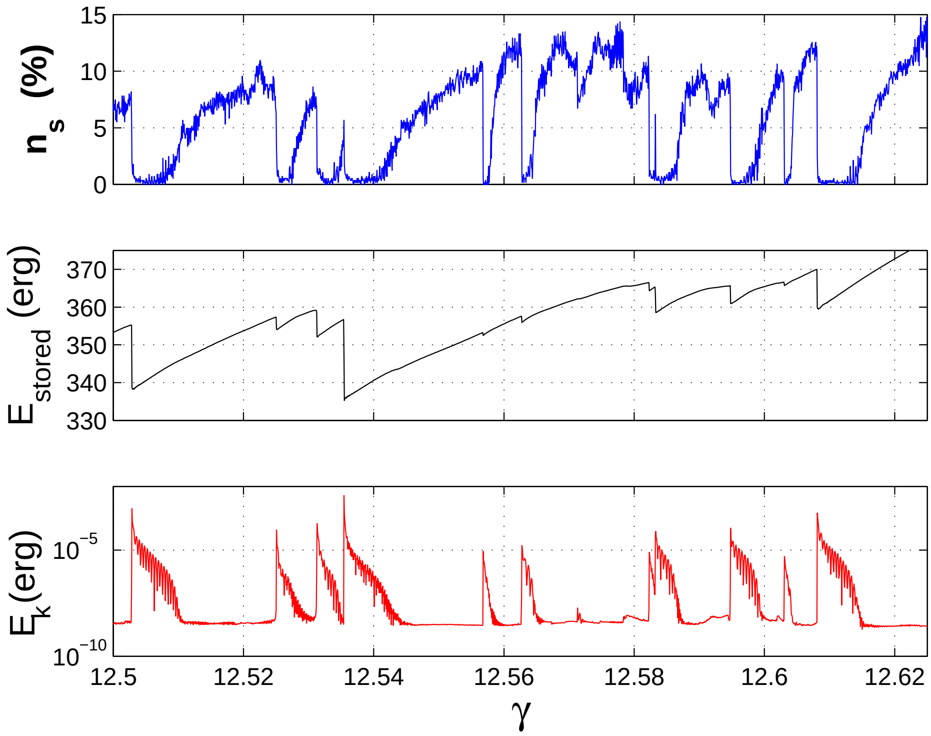

Figure 5.10: Evolution of the relative number n_s of sliding contacts, the energy stored at the contacts and the total kinetic energy E_k as a function of the shear strain γ, for an isotropic sample ($\lambda = 1$).

rearrangement of the media.

We want to define the conditional probability $P(A_E|\Delta\tau/\Delta\gamma)$ for the occurrence of an avalanche event A_E given a value of stiffness $\Delta\tau/\Delta\gamma$. Since we only have access to $P(\Delta\tau/\Delta\gamma|A_E)$ from the analysis of the data, we use the Bayes theorem from probability theory [141]. This theorem relates the conditional probability distribution $P(A|B)$ or $P(B|A)$ of two stochastic events or random variables A and B to their marginal probability distributions $P(A)$ and $P(B)$. Thus, we get

$$P(A_E|\Delta\tau/\Delta\gamma) = \frac{P(\Delta\tau/\Delta\gamma|A_E)P(A_E)}{P(\Delta\tau/\Delta\gamma)} \tag{5.4}$$

For the case of the occurrence of one avalanche A_E for given a stiffness value $\Delta\tau/\Delta\gamma$, we select a time interval $t = 5 \cdot 10^6$ to analyze the evolution of the stress-strain behavior of the system. First, we discretize the time interval in time increments of $dt = d\gamma/\dot{\gamma}$. Since the shear rate $\dot{\gamma} = 1.25 \cdot 10^{-5}$ s^{-1} and $d\gamma = 0.0016$, the time increment $dt = 128$ s is also constant in our simulation. We select the same dt for both isotropic and anisotropic systems. The conditional probability $P(\Delta\tau/\Delta\gamma|A_E)$ of having a stiffness value $\Delta\tau/\Delta\gamma$ at the occurrence of an avalanche A_E is obtained by identifying the time t before

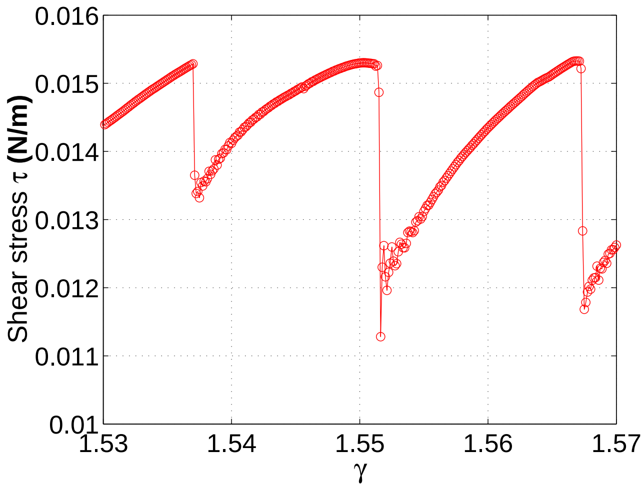

Figure 5.11: Shear force vs shear strain. The stick-slip character of the system response is observed.

an avalanche and calculating the stiffness value $\Delta\tau/\Delta\gamma$ for the time interval $t - dt$ to t. This process is performed for all the events A_E within the time interval. The probability $P(A_E)$ is calculated as the total number of avalanches divided by the total number of time increments dt. Finally, $P(\Delta\tau/\Delta\gamma)$ is the probability distribution of $\Delta\tau/\Delta\gamma$. Having $P(\Delta\tau/\Delta\gamma|A_E)$, $P(A_E)$ and $P(\Delta\tau/\Delta\gamma)$ we use Eq. (5.4) to obtain the conditional probability $P(A_E|\Delta\tau/\Delta\gamma)$ for the occurrence of an avalanche A_E when the system has a given stiffness value $\Delta\tau/\Delta\gamma$. In Figure 5.12, the conditional probabilities $P(A_E|\Delta\tau/\Delta\gamma)$ and $P(\Delta\tau/\Delta\gamma|A_E)$ for the isotropic system $\lambda = 1.0$ and the anisotropic system $\lambda = 2.3$ are shown. We make the following observations:

- For all the samples, the conditional probability $P(A_E|\Delta\tau/\Delta\gamma)$ decreases logarithmically with the stiffness value $\Delta\tau/\Delta\gamma$. The stiffer the system, the smaller is the probability of failure (see Fig 5.12a), yielding $P(A_E|\Delta\tau/\Delta\gamma) \sim q\log(\Delta\tau/\Delta\gamma)$.

- Anisotropic samples compared to the isotropic ones explore a different range of stiffness at failure due to the larger rotational frustration that the elongated particles undergo, see Fig. 5.12a and 5.12b. This is specially observed for sample $\lambda = 2.3$ H, with particles oriented along the shear direction, that explores weaker states due to a more stable structure consequence of its initial configuration.

- The coefficients of the tail of the distributions are $q = -42.1$ for $\lambda = 1.0$, $q = -28.6$ for $\lambda = 2.3$ V and $q = -30.78$ for $\lambda = 2.3$ H (see Fig. 5.12a). Thus, anisotropic samples exhibit a different behavior compared to the isotropic samples. In particular, sample $\lambda = 2.3$ H presents a larger stability having a smaller $P(A_E|\Delta\tau/\Delta\gamma)$ than the other samples. On the contrary, sample $\lambda = 2.3$ V shows a higher $P(A_E|\Delta\tau/\Delta\gamma)$ due to the unstable configuration of particles oriented perpendicular to the shear.

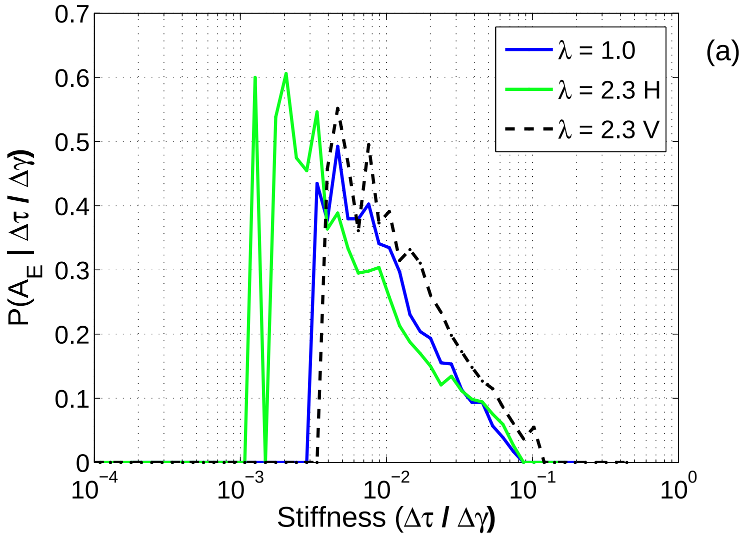

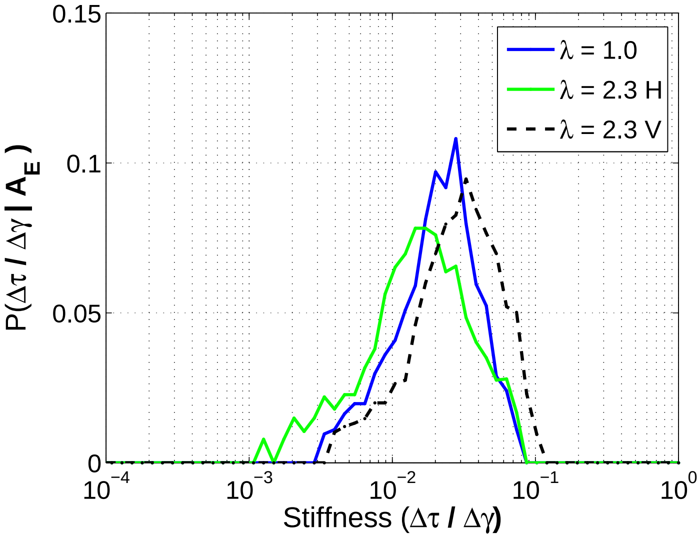

Figure 5.12: Conditional probability distributions (a) $P(A_E|\Delta\tau/\Delta\gamma)$ of the occurrence of an avalanche A_E given a stiffness $\Delta\tau/\Delta\gamma$ and (b) $P(\Delta\tau/\Delta\gamma|A_E)$ of having a stiffness $\Delta\tau/\Delta\gamma$ at the occurrence of an avalanche. System size 16×16. Isotropic $\lambda = 1.0$ and anisotropic samples $\lambda = 2.3$ are presented. Labels H and V correspond to horizontal and vertical samples.

Next, we calculate the conditional probability $P(A_E|F_s/F_n)$ of occurrence of an avalanche A_E given a value of force ratio F_s/F_n, where F_s is the shear force and F_n is the normal force at the boundaries. The same procedure as explained before is followed. Having $P(F_s/F_n|A_E)$, $P(A_E)$ and $P(F_s/F_n)$ and using Eq. (5.4) we obtain the conditional probability $P(A_E|F_s/F_n)$. In Figure 5.13, the conditional probabilities $P(A_E|F_s/F_n)$ and $P(F_s/F_n|A_E)$ for the isotropic system $\lambda = 1.0$ and the anisotropic system $\lambda = 2.3$ are

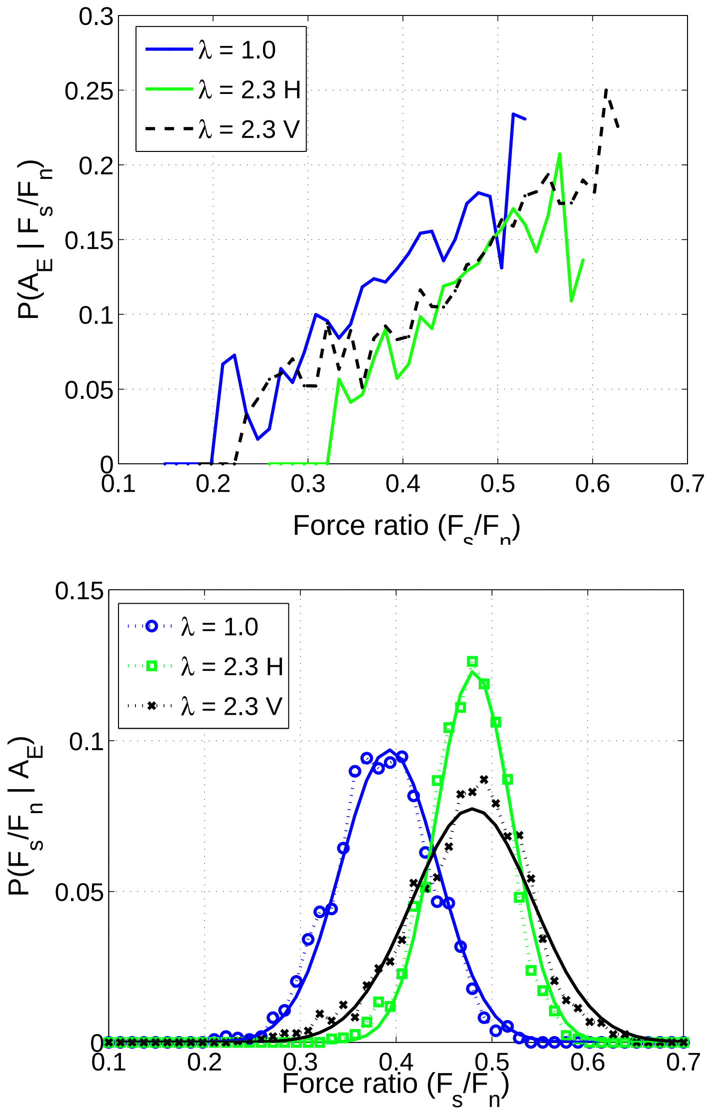

Figure 5.13: Conditional probability distributions (a) $P(A_E|F_s/F_n)$ of the occurrence of an avalanche A_E given a frictional strength F_s/F_n and (b) $P(F_s/F_n|A_E)$ of having a frictional strength F_s/F_n at the occurrence of an avalanche. System size 16×16. Isotropic $\lambda = 1.0$ and anisotropic samples $\lambda = 2.3$ are presented. Labels H and V correspond to horizontal and vertical samples. The $P(F_s/F_n|A_E)$ follows a normal distribution, except for sample $\lambda = 2.3$ V. Solid lines represent the normal distribution of the data.

shown. We make the following comments:

- The conditional probability $P(A_E|F_s/F_n)$ increases approximately linearly with F_s/F_n. Higher the mobilized strength F_s/F_n higher is the probability of failure (see Fig. 5.13).

- In general, the anisotropic samples $\lambda = 2.3$ are able to mobilize higher frictional strength than the isotropic sample $\lambda = 1.0$, see Fig. 5.13.

- For the same force ratio F_s/F_n the anisotropic samples $\lambda = 2.3$ presents a lower probability $P(A_E|F_s/F_n)$ than isotropic samples $\lambda = 1.0$, see Fig. 5.13. This is certainly due to the influence of particle shape anisotropy on the global strength of the material, as presented already in Chapter 4.

- The probability distribution $P(F_s/F_n|A_E)$ of having a force ratio F_s/F_n at the occurrence of an avalanche A_E follows a normal distribution, except for the sample $\lambda = 2.3$ H. The mean of $P(F_s/F_n|A_E)$ for the anisotropic samples ≈ 0.48 is larger than the mean of the isotropic sample 0.39. The influence of the initial configuration on the $P(F_s/F_n|A_E)$ of the anisotropic samples is observed in the standart deviation of the data. Sample $\lambda = 2.3$ H has a standard deviation equal to 0.04 and sample $\lambda = 2.3$ V equal to 0.063. The standard deviation of the isotropic sample is 0.05.

From these results, the influence of particle shape and the initial configuration of the sample on the conditional probabilities $P(A_E|\Delta\tau/\Delta\gamma)$ and $P(A_E|F_s/F_n)$ is confirmed. Regarding stability in terms of stiffness at failure, anisotropic samples can explore a wider range of stiffnesses than isotropic samples. The initial configuration also plays an important role in terms of stability. The anisotropic sample $\lambda = 2.3$ H due to its more stable configuration with respect to shearing presents lower probability of failure than the isotropic sample $\lambda = 1.0$ and the anisotropic one $\lambda = 2.3$ V.

Concerning frictional strength, the probability of an avalanche to occur increases with the force ratio F_s/F_n. Samples with anisotropic particles $\lambda = 2.3$ mobilized higher force ratio F_s/F_n than the isotropic sample $\lambda = 1.0$. Anisotropic samples also exhibit lower probability of failure for the same value of F_s/F_n than the isotropic one. The distribution of force ratio F_s/F_n at the occurrence of an avalanche is also highly dependent on the particle shape. All these features highlight the importance of particle shape on the mechanical behavior of granular systems.

In Figure 5.14 the sliding contact ratio n_s and the stiffness at failure of the system are presented. The stiffness is also compared to the released energy during the avalanches. Although no clear correlation between the parameters can be observed, the maximum value of stiffness that the system can present is bounded by the value of n_s. Larger n_s implies smaller stiffness (Fig. 5.14a). In Fig. 5.14b a poor correlation between stiffness and the magnitude of the events can be observed. From these observations, it is clear that the accumulation of strain at the contacts is not the only important agent in the weakening process and for the stability of the system. Therefore, additional ingredients have to be taken into account for a more exhaustive analysis as discussed in Section 5.7.

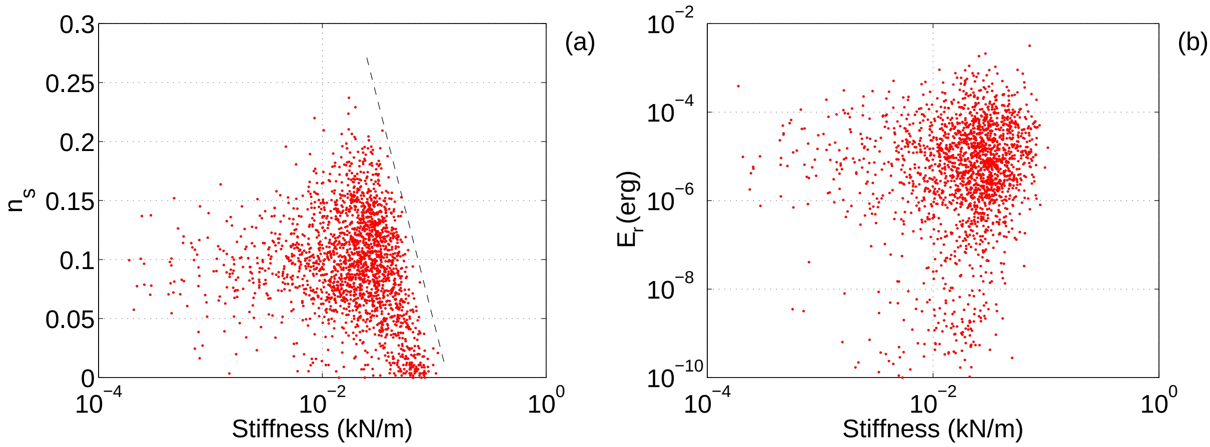

Figure 5.14: Relationship between (a) sliding contact ratio n_s vs. stiffness at failure, (b) released energy during the avalanche E_r vs stiffness at failure. Data correspond to an isotropic sample with size 16×16 particles.

5.7 Concluding remarks

In this chapter we used shear cells with periodic boundary conditions to mimic the behavior of tectonic faults with transform boundaries. The influence of particle shape anisotropy as constituent of the gouge within the fault is studied and found to play an important role in some mechanical features.

We found that the dynamics of the granular system is characterized by discrete avalanches spanning several order of magnitude similar to crackling noise [52, 129]. The granular packing driven by external forces accumulates elastic energy until the strength of the material is overcome, then the energy is suddenly released generating an avalanche. After the avalanche, the structure of the system is reorganized and a new stage of accumulation of energy starts. We calculated the probability distribution of the energy released in avalanches, and found it to be in good agreement with the Gutenberg-Richter law for samples with different particle anisotropy and different system sizes. Consequently the exponent of the released energy distribution can be seen as an invariant property of such systems.

We also studied the temporal distribution of event sequences after a mainshock. We found that the number of aftershocks decrease with the inverse of time in agreement with the empirical relation given by the Omori's law [54]. We could fit the sequences of waiting times of the aftershocks with the empirical expression and obtained exponents in good agreement with the range expected in real observations $0.7 < p < 1.5$. The anisotropic sample $\lambda = 2.3$ H compared to both the isotropic sample $\lambda = 1.0$ and the anisotropic sample $\lambda = 2.3$ V exhibits a larger temporal stability making the temporal occurrence of the avalanches longer on time. This is due to the larger frustration of rotation that the anisotropic samples $\lambda = 2.3$ suffer due to its initial configuration. This larger temporal stability at the macro-mechanical level is therefore an indication of the existence of anisotropic material within the shear zone. This could potentially explain the variation of the decay p observed in realistic earthquake sequences.

The dynamics of the system was also related to the stick-slip process [40, 142]. The system sticks between consecutive events, accrues elastic energy, and become weaker because of the increment of the sliding contacts n_s when the strength is overcome and then the system slips. We characterized the weakening of the system with the stiffness $\Delta\tau/\Delta\gamma$. We calculated the conditional probability $P(A_E|\Delta\tau/\Delta\gamma)$ of occurrence of an avalanche event A_E given a stiffness value $\Delta\tau/\Delta\gamma$. We found that $P(A_E|\Delta\tau/\Delta\gamma)$ decreases logarithmically with the stiffness and that the decay rate depends on particle shape. The frictional strength of the samples was characterized by the force ratio F_s/F_n. We also calculated the conditional probability $P(A_E|F_s/F_n)$ of occurrence of an avalanche event A_E given a force ratio F_s/F_n.

The results concerning the conditional probabilities $P(A_E|\Delta\tau/\Delta\gamma)$ and $P(A_E|F_s/F_n)$ stressed the influence of particle shape and the initial configuration of the sample on the mechanical behavior of the system. Regarding stability in terms of stiffness at failure, anisotropic samples can explore a wider range of stiffnesses than the isotropic sample. This is due to the larger kinematic constraint that anisotropic particles undergo during shear. The initial configuration plays a role in terms of stability since anisotropic sample $\lambda = 2.3$ H due to its more stable configuration with respect to shearing presents lower probability of failure than the isotropic sample $\lambda = 1.0$ and the anisotropic sample $\lambda = 2.3$ V.

Concerning frictional strength, the probability of an avalanche to occur increases with the force ratio F_s/F_n. Samples with anisotropic particles $\lambda = 2.3$ mobilized higher force ratio F_s/F_n than the isotropic sample $\lambda = 1.0$. Anisotropic samples also exhibit lower probability of failure for the same value of F_s/F_n than the isotropic one. The distribution of force ratio F_s/F_n at the occurrence of an avalanche is also highly dependent on the particle shape. All these features highlight the importance of particle shape on the mechanical behavior of granular systems.

In previous works concerning the avalanches in granular piles [28, 143], some avalanche precursors related to the onset of fluidized regions of sliding contacts were found. These fluidized regions were located in the weak network of contacts. This weak network comprises contacts transmitting forces smaller than the average force and therefore has a minimal contribution to the stress state [27, 144]. The interplay prior to a granular avalanche between the fluidize regions and the strong contact network, carrying the forces larger than the average, is investigated in Ref. [143]. It is concluded that, while the strong contact network (skeleton of the granular structure [46, 143, 144]) is responsible for the strength and stability of the packing, the weak contact network plays an important role in the destabilization proccess. Although the previous results correspond to the transition from static equilibrium to a dynamic flow, an analysis comprising a proper characterization of the geometrical properties of the contact network and force chains [47], its evolution, and the interplay of the destabilization agents as the sliding contacts and the building and collapse of force chains will help to get a better understanding of the stick-slip fluctuations in sheared granular media and thus the existence of precursors of avalanches in fault gouges. Precursors are expected to be related to sharp changes in the micro-structure of the granular packing [145].

Although the results from our numerical model show good agreement with the processes observed in nature, we are aware of the challenges to have a more realistic simulation of fault zones [146]. The following features should be considered in future work:

- Development of transparent (or absorbing) boundary condition since the acoustic emission after an avalanche are trapped due to the periodic boundary conditions. In nature the seismic waves generated during earthquakes are free to travel through the globe.
- Grain fragmentation should be implemented, since natural earthquakes result from the combined effect of frictional instabilities and rock fragmentation.
- Generalization of the model to a three dimensional system, using polyhedra to represent the rock.

Chapter 6

Numerical Improvement of the Discrete Element Method

One of the standard approaches to model the dynamics of granular media is to use the Discrete Element Method (DEM) [2, 3, 48, 58, 106, 147, 148]. However, some problems may arise due to the need to perform numerical simulations within reasonable computational time, without compromising the overall convergence of the numerical scheme. In particular, this is true for very slow shearing when simulating earthquake faults as presented in Chapter 5 and in Ref. [42, 81]. In such cases, large integration steps have to be adopted to capture the dynamics of the real system. Usually, one assumes an upper limit for the admissible length of the integration step based on empirical reasoning [56].

In this chapter we present a detailed analysis of the bounds on the integration step in DEM for simulating collisions and shearing of granular assemblies. We show that in the numerical scheme, the upper limit for the integration step, usually taken either from the characteristic period of oscillation of the system t_s [56, 58] or from the average time t_c of one contact [149], is in fact not sufficiently small to guarantee numerical convergence of the system during relaxation. This upper limit strongly depends on (i) the accuracy of the approach used to calculate frictional forces between particles, (ii) on the corresponding duration of the contact, and (iii) on the number of degrees of freedom of the particles. Further, we address the specific case of slow shearing, for which the above limit is too small to allow for reasonable computation time. To overcome this shortcoming, we propose an alternative approach that corrects the frictional contact forces when large integration steps are taken. In this way, we enable the use of considerably larger integration steps, assuring at the same time the convergence of the integration scheme.

In Section 6.1 we present the relevant details of the DEM concerning our present analysis. Sections 6.2 and 6.3 describe the dependence of the system response on the integration step and the improved algorithm, respectively. Discussions and conclusions are given in Sec. 6.4.

6.1 The model

In this section we briefly describe the main features of the DEM, as they were already thoroughly introduced in Chapter 2. We consider a two-dimensional system of particles, each one having two linear and one rotational degree of freedom. The evolution of the system, particle position $\vec{r}_i$ and particle orientation $\vec{\theta}_i$, is given by the integration of

Newton's equations of motion, Eqs. 2.1a and 2.1b.

All the dynamics is deduced from the contact forces acting on the particles. The contact forces $\vec{f}^c$ are decomposed into their elastic and viscous contributions, $\vec{f}^e$ and $\vec{f}^v$ respectively, yielding $\vec{f}^c = \vec{f}^e + \vec{f}^v$. The viscous force $\vec{f}^v$ is important to take into account dissipation at the contact and to maintain the numerical stability of the method. This force is calculated as $\vec{f}^v = -m_r \nu \vec{v}^c$, where m_r is the reduced mass of the two particles in contact, ν is the damping coefficient and $\vec{v}^c$ is the relative velocity at the contact.

The elastic part of the contact force $\vec{f}^e$ is given by the sum of the normal and the tangential components, with respect to the contact plane between the particles, namely $\vec{f}^e = f_n^e \hat{n}^c + f_t^e \hat{t}^c$. The normal component reads $f_n^e = -k_n A/l_c$, with k_n the normal stiffness, A the overlap area between the particles and l_c the characteristic length of the contact. The tangential component is implemented using an extension of the Cundall-Strack spring [2]. Here, the tangential force is proportional to the elastic elongation ξ of an imaginary spring at the contact. This tangential force reads $f_t^e = -k_t \xi$, where k_t is the tangential stiffness. The elastic elongation ξ is updated according to Eq. (2.5),

$$\xi(t + \Delta t) = \xi(t) + \vec{v}_t^c \Delta t, \tag{2.5}$$

where Δt is the time step of the DEM simulation, and $\vec{v}_t^c$ is the tangential component of the relative velocity $\vec{v}^c$ at the contact point. The tangential elastic elongation ξ may increase during the time that the elastic condition $|f_t^e| < \mu f_n^e$ is satisfied. The sliding condition is enforced keeping constant the elastic displacement ξ when the Coulomb limit condition $|f_t^e| = \mu f_n^e$ is reached. Hereafter, the tangential force is carefully studied since its calculation includes the integration step of the numerical simulation and therefore depends on it.

In DEM, one of the numerical integration schemes used to calculate the evolution of the system is the Gear's predictor-corrector scheme as presented in Chapter 2. In our simulations we integrate equations of the form $\ddot{\vec{r}} = f(\vec{r}, \dot{\vec{r}})$, using a fifth order predictor-corrector algorithm that has a numerical error proportional to $(\Delta t)^6$ for each integration step [56]. However, as will be seen in Sec. 6.2, $(\Delta t)^6$ is not the numerical error of the full integration scheme, since the Equation (2.5) used to calculate the frictional force has an error of order $(\Delta t)^2$.

For a certain value of normal contact stiffness k_n, almost any value for the normal damping coefficient ν_n might be selected. Their relation defines the restitution coefficient ϵ obtained experimentally for various materials [91]. The normal and tangential restitution coefficients ϵ_n and ϵ_t are given by the ratio between the relative velocities after and before a collision, see Eq. (2.9). Therefore, a suitable closed set of parameters for this model are the ratios k_t/k_n and ϵ_t/ϵ_n (or ν_t/ν_n), together with the normal stiffness k_n and the interparticle friction μ.

The entire algorithm relies on a proper choice of the integration step Δt, which should neither be too large to avoid divergence of the integration nor too small avoiding unreasonably long computational time. The determination of the optimal integration step varies from case to case and there are two main criteria to estimate an upper bound for admissible integration steps.

The first criterion is to use the characteristic period of oscillation t_s [56], defined from Eq. (2.14). For a fifth order predictor-corrector integration scheme, it is usually accepted that a safe integration step should be below a threshold of $\Delta t < t_s/10$ [56].

The second criterion is to extract the threshold from local contact events [58, 149, 150], namely from the characteristic duration of a contact t_c given by Eq. (2.15),

$$t_c = \frac{\pi}{\sqrt{\omega_0^2 - \eta^2}}, \tag{2.15}$$

where ω_0 is the frequency of the elastic oscillator corresponding to the pair of particles in contact and η the effective viscosity. Typically, $t_c \simeq t_s/2$ and therefore one considers an admissible integration step as $\Delta t < t_c/5$ [87, 150]. In the next section we will study in detail the integration scheme for different values of the model parameters. For a more detailed description of the model see Chapter 2.

6.2 The choice of the integration step

We simulate the relative motion of two plates shearing against each other as performed in Chapter 5. We consider a system of 256 particles as illustrated in Fig. 6.1, where both top and bottom boundaries move in opposite directions with a constant shear rate $\dot{\gamma}$. Here, the top and bottom layer of the sample have fixed boundary conditions, while

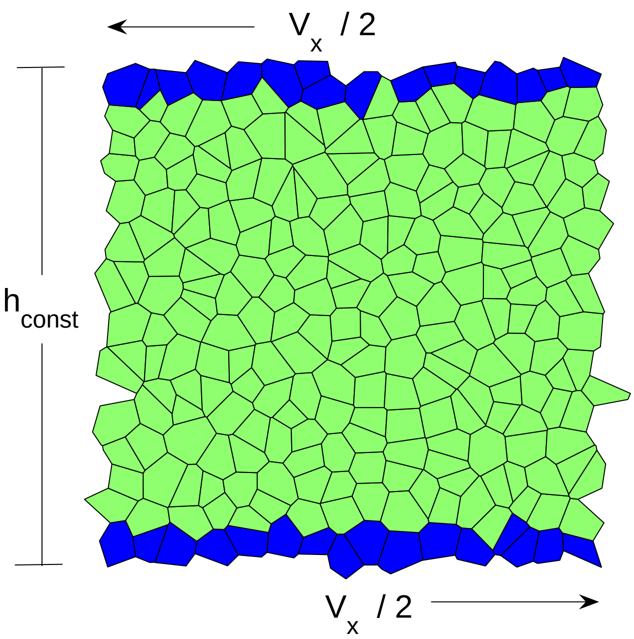

Figure 6.1: Sketch of the system of 256 particles under shearing of top and bottom boundaries (dark particles, blue in color). Horizontally, periodic boundary conditions are considered and a constant low shear rate is chosen (see text).

horizontally we consider periodic boundary conditions. The volumetric strain is suppressed, i.e., the vertical position of the walls is fixed and there is no dilation. Moreover, the particles of the fixed boundary are not allowed to rotate or move against each other. We select a shear rate $\dot{\gamma} = 1.25 \cdot 10^{-5}\mathrm{s}^{-1}$, and use the following parameter values $k_n = 400\,\mathrm{N/m}$, $\epsilon_n = 0.9875$, and $\mu = 0.5$. The relation k_t/k_n is chosen such that $k_t < k_n$, similarly to previous studies [2, 34, 150], namely $k_t/k_n = 1/3$. Further, for simplicity we consider $\nu_t/\nu_n = k_t/k_n$, which when substituted in Eq. (2.9) yields $\epsilon_t/\epsilon_n = 1.0053$.

By integrating such a system of particles using the scheme described in Chapter 2, one can easily compute the kinetic energy E_k of a given particle i,

$$E_k(i) = \frac{1}{2}\left(m_i\dot{\vec{r}}_i^2 + I_i\vec{\omega}_i^2\right), \tag{6.1}$$

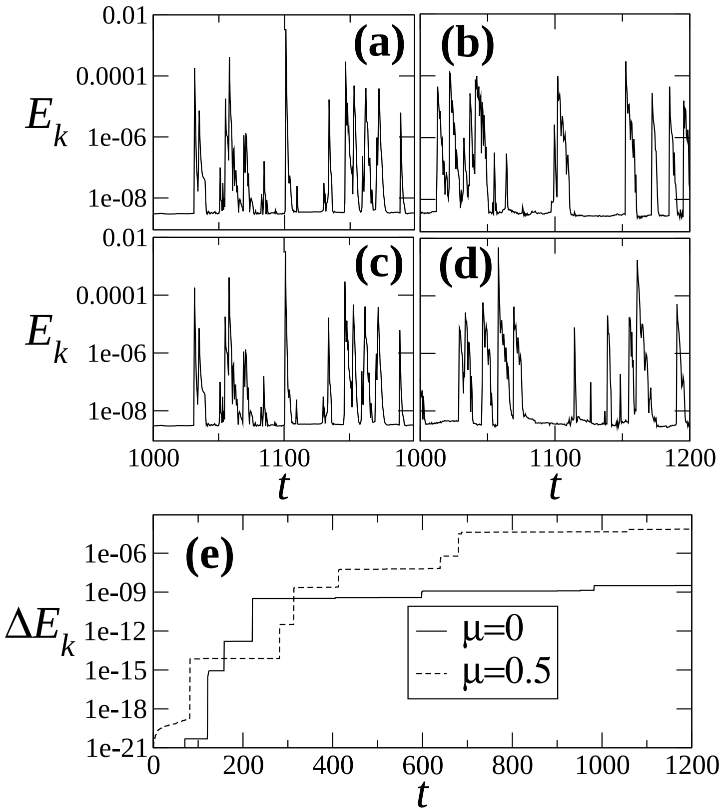

Figure 6.2: Dependence of the numerical scheme on the integration step Δt and the friction coefficient μ, by plotting the kinetic energy E_k as a function of time, for **(a)** $\Delta t = 10^{-3}$ s and $\mu = 0$ (no friction), **(b)** $\Delta t = 10^{-3}$ s and $\mu = 0.5$, **(c)** $\Delta t = 5 \times 10^{-3}$ s and $\mu = 0$, and **(d)** $\Delta t = 5 \times 10^{-3}$ s and $\mu = 0.5$. In **(e)** we show the difference between the values of E_k obtained with the two values of Δt. Here, $k_n = 400\,\mathrm{N/m}$ and the parametric relation in (2.15) are used (see text).

where velocity $\dot{\vec{r}}$ is computed from the predictor-corrector algorithm, I_i is the moment of inertia of the polygon and $\vec{\omega}_i$ is the angular velocity.

In Fig. 6.2 we show the evolution of the kinetic energy for two different $\Delta t = 0.001$ s and 0.005 s. As we can see, frictionless particles (Fig. 6.2a and 6.2c) have an E_k that does not change for different integration steps, while for $\mu = 0.5$ (Fig. 6.2b and 6.2d) the evolution of E_k strongly depends on Δt. In Fig. 6.2e we plot the cumulative difference ΔE_k between the values of E_k obtained for each integration step. Here, we can see that in the absence of friction ΔE_k is significantly lower than if friction is present.

The two time steps used in Fig. 6.2 can be written as $\Delta t = 13/500t_c$ and $13/2500t_c$. Thus, we conclude that the expected upper limit $\sim t_c/10$ is still too large to guarantee convergence of the integration scheme if friction is considered.

Next, we perform a careful analysis to obtain a proper integration step as function of the parameters of our model. For that, we consider the simple situation of two circular particles and study the kinetic energy of one of them under external forcing, as sketched in Fig. 6.3. We start with two touching discs, i and j, where one of them, say i, remains fixed, while the other is subject to a force $\vec{f}$ perpendicular to its surface (no external torque is induced) along the x-axis. As a result of this external force, the disc j undergoes translation and rotation. The resulting contact forces acting in opposite direction to the external force are obtained from the corresponding elastic springs computed as described in Chapter 2. This results in an oscillation of disc j till relaxation (dashed circle in Fig. 6.3) with a final center of mass displacement of ΔR and a rotation around

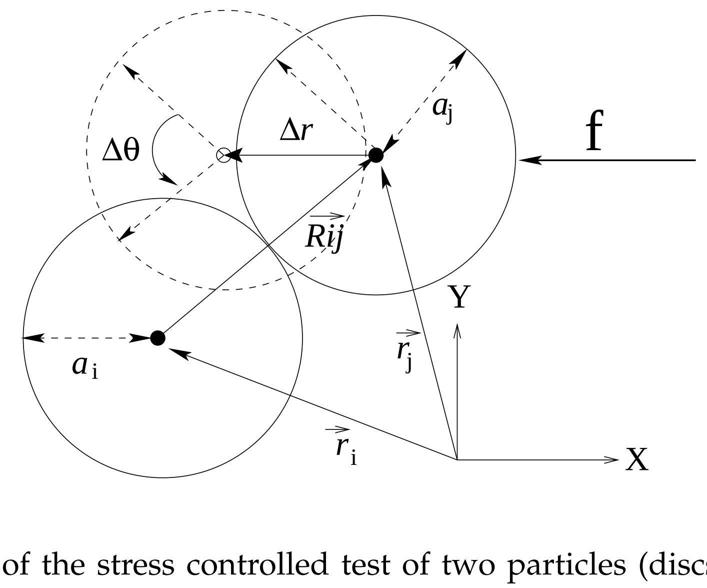

Figure 6.3: Sketch of the stress controlled test of two particles (discs). The particle located at $\vec{r}_i$ remains fixed, while the particle at $\vec{r}_j$ is initially touching particle i. The vector $\vec{R}_{ij}$ connecting the center of mass of particles i and j is initially oriented at 45^o with respect to the x-axis. After applying the constant force $\vec{f}$ to disc j, the system relaxes to a new position (dashed circumference). Between its initial and final position particle j undergoes a displacement Δr and a rotation $\Delta\theta$ (see text).

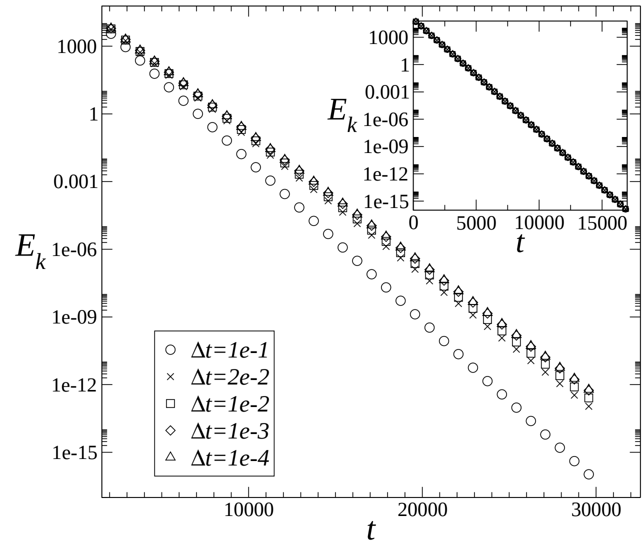

Figure 6.4: The relaxation of the system of two discs sketched in Fig. 6.3. Here we plot the kinetic energy E_k as a function of time t (in units of t_c) for different integration increments Δt and using a stiffness $k_n = 4\times10^8$ N/m and a friction coefficient $\mu = 500$. The large value for μ is chosen such that the system remains in the elastic regime. As we can see, the relaxation time t_R converges to a constant value when Δt is sufficiently small (see text). This discrepancy between the values of t_R when different integration steps are used does not occur in the absence of friction ($\mu = 0$), as illustrated in the inset. The slope of the straight lines is $-1/t_R$ (see Eq. (6.2)).

the center of mass of $\Delta\theta$. Since $\vec{f}$ is kept constant, the procedure is stress controlled.

In Fig. 6.4 we plot the kinetic energy as a function of time, from the beginning until relaxation, for the two particle system. Different integration steps, namely $\Delta t = 10^{-1}, 2\times 10^{-1}, 10^{-2}, 10^{-3}$ and 10^{-4} s in units of t_c are used. As we see, the kinetic energy decays exponentially,

$$E_k(t) = E_k^{(0)} \exp\left(-\frac{t}{t_R(\Delta t)}\right), \tag{6.2}$$

where t_R is a relaxation time whose value clearly depends on the integration step Δt. As illustrated in the inset of Fig. 6.4, this change in t_R is not observed when friction is absent ($\mu = 0$), since no tangential forces are considered ($f_e^t = 0$).

Next, we show that this dependence of t_R on Δt vanishes for

$$\Delta t \leq T_t(k_n, \mu)\ t_c, \tag{6.3}$$

where $T_t(k_n, \mu)$ is a specific function that is determined below. Notice that the only free parameters on which T_t may depend are the interparticle friction μ and the normal stiffness k_n, since we consider a fixed restitution coefficient in the normal direction, $\epsilon_n = 0.9875$ and fixed relations $k_t/k_n = 1/3$ and $\epsilon_t/\epsilon_n = 1.0053$.

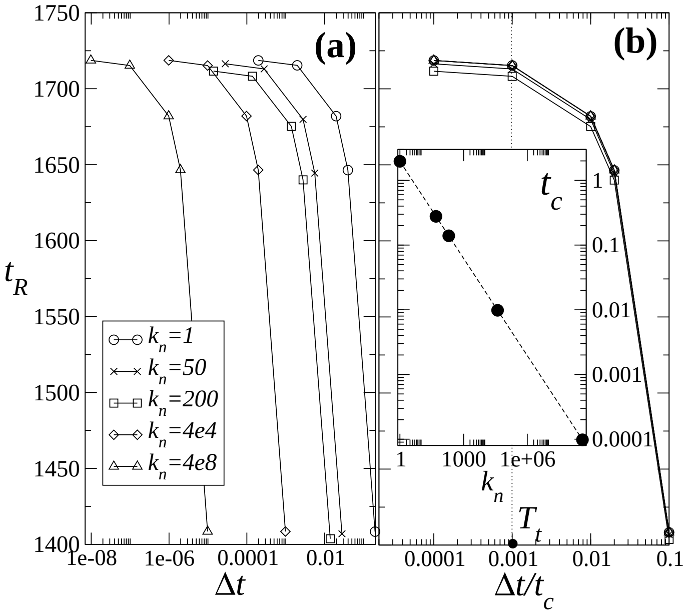

Figure 6.5: The relaxation time t_R (in units of t_c) as a function of **(a)** the integration step Δt and **(b)** the normalized integration step $\Delta t/t_c$, where the contact time t_c is defined in Eq. (2.15). Here, the friction coefficient is kept fixed at $\mu = 500$ and different stiffnesses k_n (in units of N/m) are considered. The quotient $\Delta t/t_c$ collapses all the curves for different k_n. We find $t_c \sim k_n^{-1/2}$ as illustrated in the inset (see Eq. (2.15)). As a final result one finds a constant $T_t = 10^{-3}$ (dashed vertical line). For other values of the friction coefficient μ we observe similar results.

Figure 6.5a shows the relaxation time t_R of the kinetic energy of the two-particle system for different values of stiffnesses, namely for $k_n = 1, 50, 200, 10^4$ and 10^8 N/m. For all k_n values, one can see that with decreasing Δt the relaxation time t_R increases until it converges to a maximum. The stabilization of t_R occurs when Δt is small compared to the natural period $1/\omega_0$ of the system. We define T_t as the largest value of Δt for which we have this maximal relaxation time.

As shown in Fig. 6.5b, all curves in 6.5a can be collapsed by using the normalized integration step $\Delta t/t_c$. From Eq. (2.15) we calculate the contact times corresponding to these k_n values as $t_c = 1.969, 0.278, 0.139, 9.8 \times 10^{-2}$ and 9.8×10^{-5} s, respectively. In fact, as shown in the inset of Fig. 6.5b the relaxation time scales with the stiffness as $t_c \sim k_n^{-1/2}$ (see Eq. (2.15)).

From Fig. 6.5 one can conclude that the relaxation time converges when the integration step obeys Eq. (6.3) with $T_t = 10^{-3}$ (dashed vertical line in Fig. 6.5b). We simulate the system also for $\mu = 0.005, 0.005, 0.05, 0.5, 5, 50$ and 500 and similar results are obtained.

In Fig. 6.5 both translation and rotation of the particles are considered. This is of crucial interest for instance to simulate rolling [42, 151]. Suppressing rotation can also be

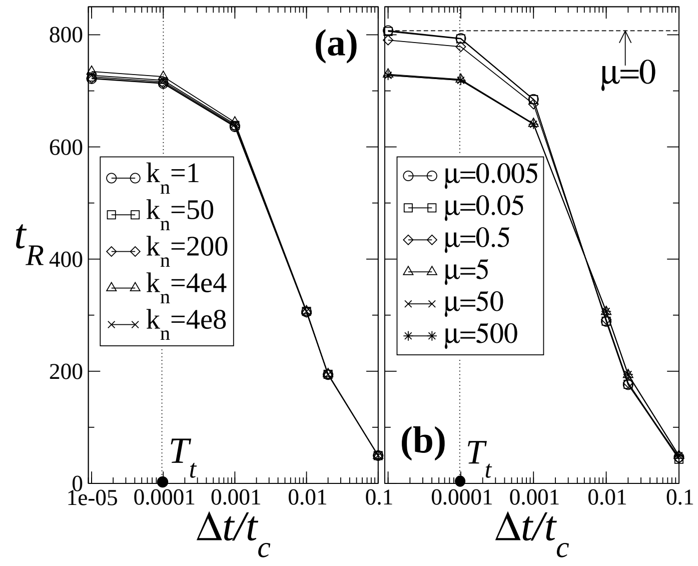

Figure 6.6: The relaxation time t_R (in units of t_c) of the kinetic energy as a function of the normalized integration step $\Delta t/t_c$, when rotation is suppressed. **(a)** $\mu = 500$ and different values of k_n and for **(b)** $k_n = 4 \times 10^8$ and different values of μ. The dashed horizontal line $\mu = 0$ in (b) indicates the relaxation time of the kinetic energy in the absence of friction (see text).

of interest, e.g., when simulating fault gouges. In such a case, by hindering the rotation of particles, one can mimic young faults where a strong interlocking between the constituent rocks is expected [42].

To study this scenario, we present in Fig. 6.6a the relaxation time for the same parameter values as in Fig. 6.5, now disabling rotation. Here, we obtain a constant $T_t = 10^{-4}$ also, independent of k_n, one order of magnitude smaller than the previous value in Fig. 6.5. In other words, when rotation is suppressed, one must consider integration steps typically one order of magnitude smaller than in the case when the discs are able to rotate. This can be explained as follows.

When suppressing rotation, one restricts the system to have a single degree of freedom. All energy stored in the rotational degree of freedom through the integration of the equations of motion is suppressed. This effectively acts like an increase of the friction coefficient, making the system more sensitive to the integration step, i.e., yielding a smaller bound T_t. By comparing Fig. 6.6a with Fig. 6.5a, one can see that the relaxation time t_R is smaller when rotation is suppressed.

From the bounds on the integration steps obtained above, one realizes that, in general, the correct integration step must be significantly smaller than the one usually assumed.

While Fig. 6.6a clearly shows that t_R does not depend on the stiffness k_n, from Fig. 6.6b one sees that the same is not true for the friction coefficient μ. Indeed, from Fig. 6.7 we see that there is a change of the relaxation time around $\mu = 1$. Here, the values correspond to a normalized integration step $\Delta t/t_c = 10^{-5}$ for which t_R has already converged.

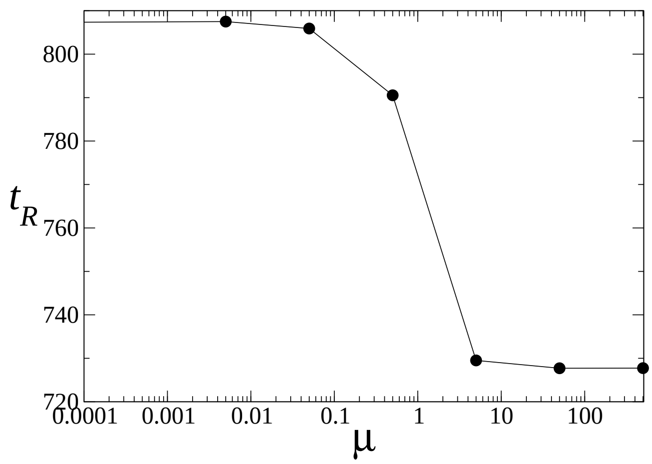

Figure 6.7: The relaxation time t_R (in units of t_c) as a function of the friction coefficient μ when rotation is suppressed. Here $k_n = 4 \times 10^8$ N/m which corresponds to a contact time $t_c = 9.8 \times 10^{-5}$ s. The normalized integration step is $\Delta t / t_c = 10^{-5}$.

This might be explained by considering the fact that for large values of μ the contact is essentially non-sliding, which induces a faster relaxation than for smaller μ values.

It is important to stress that all the results above were taken within the elastic regime, since the dependence on Δt does not occur when the Coulomb condition is fulfilled (inelastic regime). This fact indicates that the improvements in the algorithm should be implemented when computing the elastic component of the tangential contact force, in Eq. (2.5), as explained in the next section.

6.3 Improved approach to integrate the tangential contact force

In this section we will describe a technique to overcome the need of very small integration steps. As shown previously, when using Cundall's spring [106], the relaxation time of the two particles only converges when Δt is a small fraction T_t of the contact time t_c. This is due to the fact that the elastic elongation is assumed to be linear in Δt, i.e., the finite difference scheme in Eq. (2.5) is of very low order, $(\Delta t)^2$, compromising the convergence of the numerical scheme that is of order $(\Delta t)^6$. Therefore, the most plausible way to improve our algorithm is by choosing a different expression to compute the elastic tangential elongation ξ without using Eq. (2.5).

We will introduce an expression for ξ that contains only the quantities computed in the predictor step. In this way we guarantee that ξ has errors of the order of $(\Delta t)^6$, instead of $(\Delta t)^2$, as it is the case of Eq. (2.5). Let us illustrate our approach on the simple system of two discs considered in the previous section (see Fig. 6.3).

On one side, if rotation is not allowed, the elastic elongation ξ depends only on the relative position of the two particles. In this case we substitute Eq. (2.5) by the expression

$$\xi_j^{(tr)}(t+\Delta t) = \xi_j^{(tr)}(t) + \frac{a_i}{a_i + a_j}(\vec{R}_{ij}^p(t+\Delta t) - \vec{R}_{ij}^p(t)) \cdot \hat{t}^c, \tag{6.4}$$

where a_i and a_j are the radii of the discs i and j respectively, $\vec{R}_{ij}$ is the vector connecting both centers of mass and pointing in the direction $i \to j$ (see Fig. 6.3). Index p indicates quantities derived from the coordinates computed at the predictor step.

On the other side, if $\vec{R}_{ij}$ is kept constant and only rotation is allowed, particle j will have an elongation ξ that depends only on its rotation between time (t) and $(t+\Delta t)$:

$$\xi_j^{(rot)}(t+\Delta t) = \xi_j^{(rot)}(t) + (\theta_j^p(t+\Delta t) - \theta_j^p(t))a_j, \tag{6.5}$$

where $\theta^p(t)$ and $\theta^p(t+\Delta t)$ are the angles of some reference point on particle j at time (t) and $(t+\Delta t)$ respectively.

When both translation and rotation of particle j occur, the elongation is the superposition of both contributions, yielding $\xi_j = \xi_j^{(tr)} + \xi_j^{(rot)}$.

Figure 6.8 shows the relaxation time t_R as a function of the integration step for the three situations above, namely when only rotation is considered, when only translation is considered, and when both rotation and translation are allowed. As we see for all these cases, the relaxation time is independent on the integration step. This is due to the fact that all quantities in the expression for ξ above are computed at the predictor step which has an error of the order of $(\Delta t)^6$, i.e., the error $(\Delta t)^2$ introduced in Eq. (2.5) is now eliminated. Therefore, with the expressions in Eqs. (6.4) and (6.5) one can use significantly larger integration steps than with the original Cundall spring.

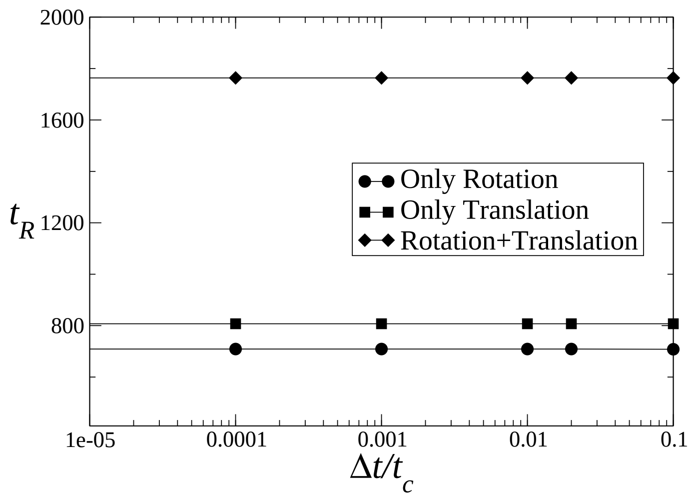

Figure 6.8: The relaxation time t_R (in units of t_c) using Eqs. (6.4) and (6.5) between two discs, as illustrated in Fig. 6.3. For the three cases considering only rotation, only translation or both, the relaxation time remains constant independent of the integration step.

When considering discs, one does not take into account the shape of the particles. Next, we consider the more realistic situation of irregular polygonal-shaped particles. Motion of rigid particles with polygonal shape is more complicated than that of simple discs, since the contact point no longer lies on the vector connecting the centers of mass. Further, for polygons, one must also be careful when decomposing the dynamics of each particle into translation and rotation around its center of mass. This implies recalculating each time the position of the center of mass (only from translation) and the relative position of the vertices (only from rotation).

Therefore, for the translational contribution $\xi^{(tr)}$ in Eqs. (6.4), we compute the overlap area between the two particles at time (t) and $(t + \Delta t)$. This overlap area is in general a polygon whose center of mass can be also computed, yielding $\vec{r}^p_c(t)$ and $\vec{r}^p_c(t + \Delta t)$, respectively. The increment for the translational contribution will be just the projection of $(\vec{r}^p_c(t) - \vec{r}^p_c(t+\Delta t))$ onto the contact plane $\hat{t}^c$. Similarly, the contribution from the particle rotation is computed by determining the branch vectors, $\vec{l}^{c,p}(t)$ and $\vec{l}^{c,p}(t + \Delta t)$, defined as the vectors connecting the center of the particle and the center of the overlap area at time (t) and $(t + \Delta t)$, respectively. Having the branch vectors at the time (t) and $(t + \Delta t)$, one can derive their average value $l_a = (\| \vec{l}^{c,p}(t + \Delta t) \| + \| \vec{l}^{c,p}(t) \|)/2$ and the angle defined by them, namely $\theta = \arccos \left(\vec{l}^{c,p}(t + \Delta t) \cdot \vec{l}^{c,p}(t) \,/\, \| \vec{l}^{c,p}(t + \Delta t) \| \, \| \vec{l}^{c,p}(t) \| \right)$. This yields an increment for Eq. (6.5) equal to $\theta\, l_a$.

Figure 6.9 compares how the relaxation time varies with the normalized time step when the original Cundall approach is used (squares) and when our improved approach is introduced (circles). Clearly, the dependence on the integration step observed for the usual integration scheme disappears when our improved approach is introduced. There-

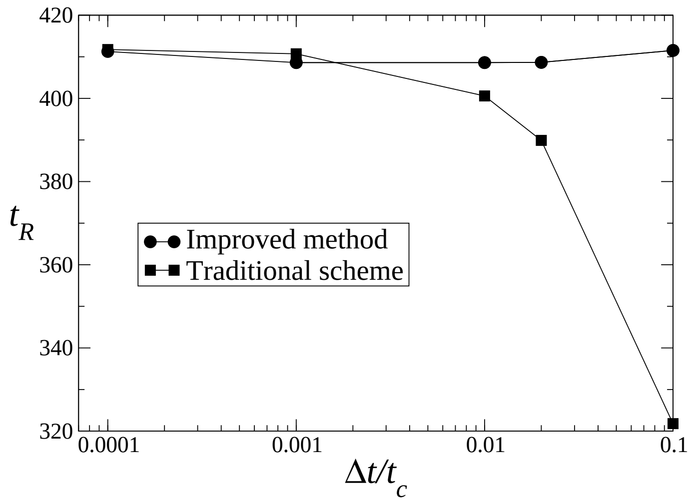

Figure 6.9: Stress control test between two polygonal particles. Comparison of the relaxation time t_R (in units of t_c) when using the standard integration scheme (squares) and the proposed improved scheme (circles). Here, rotation is neglected.

fore, all the conclusions taken above for discs remain valid for polygons.

6.4 Concluding remarks

In this chapter we introduced a technique to improve the accuracy of the numerical scheme used to compute the evolution of particle systems.

To that end, we have first shown that the range of admissible integration steps has an upper limit significantly smaller than the one typically used. The accuracy of the numerical scheme not only depends on the associated error when computing the particle positions (predictor-corrector scheme), but also on the accuracy when determining the frictional force, which is usually implemented by the Cundall spring. Since the Cundall spring is linear in the integration step, the overall accuracy of the numerical scheme cannot be higher than $(\Delta t)^2$. Therefore, when large integration steps are required, e.g., in slow shearing, the numerical scheme does not give accurate results.

To overcome this problem we introduced an alternative approach for computing the frictional forces that suits not only the simple situation of discs but the more realistic situation of polygonal particles. Our approach is particularly suited for situations where non-sliding contacts are relevant to the overall response. In general, for any other integration scheme, the substitution of the Cundall spring expression by the relations introduced in Eqs. (6.4) and (6.5), yields an error that is of the same order as the one associated with the predictor-corrector scheme.

Inspired by the above results, some questions arise to further improve our approach. First, the influence of the relations k_t/k_n and ϵ_t/ϵ_n should also be considered. Preliminary simulations have shown that the upper limit for the integration step increases with the value of k_t/k_n. Second, the test assumes a unique choice for the position of the contact point. However, in a system under shear the integration must be also performed before the appearance of new contacts. The initial contact point of a new contact will depend on the size of the integration step. This point should also be taken into account within our new approach, either by assuming some sort of interpolation or by using an event-driven scheme till the first contact point. Third, there is the problem of how to better define the contact point between two polygons. Since the contact point is taken as the geometrical center of their overlap area, the branch vectors also vary during rotation, which is not taken into account in our present approach. These points have to be addressed in the future.

Chapter 7

Conclusions

In this thesis we have carried out a micro-mechanical investigation of the mechanical behavior of granular soils using the Discrete Element Method (DEM). The granular soil is represented by a two dimensional model of polygonal particles. This model enables a more realistic representation of granular soils than the existing models of disks or spheres, since it reproduces the two principal scales in shape irregularity at the scale of particle diameter.

We focused on the following main problems: (i) the existence and uniqueness of the so-called critical state in soil mechanics, the influence of particle shape anisotropy on the global mechanical behavior of granular packing and in particular on the critical state, (ii) the evolution of isotropic and anisotropic granular packing under very slow shear conditions as appear in earthquake faults and, (iii) the dependency of the tangential contact force on the integration step of the numerical simulation.

The main results of this thesis are summarized as follows:

(i) We established the existence and uniqueness of the critical state attained under larger shear deformations by studying packings of isotropic particles under biaxial compression. The simulation results show that at large strains the granular packing reaches the critical state independent of their initial density and deforms not only at constant void ratio and shear stress but also at constant fabric anisotropy and mechanical coordination number. The coordination number was found to be the first variable to attain a critical value enabling the rest of the micro and macro-mechanical variables to converge towards the critical state. The uniqueness of the critical state was proven when critical states, i.e., critical void ratio and critical stress ratio associated with different initial stress conditions, collapsed onto one critical state line connecting the critical states. We also showed that for different contact friction coefficients the granular packing reaches the same critical state.

For interparticle friction coefficient equal to zero the packing yields a resistance to shear. From this result we conclude that the macroscopic frictional behavior of granular materials is not only a result of the interparticle friction but also of mesoscale arrangements such as force chains [45–47] and fabric evolution [44]. This emphasizes the idea of the nonlocal behavior of granular assemblies.

At the critical state the granular packing presents an unstable behavior that is characterized by strong fluctuations of stress in agreement with experiments involving glass spheres [40, 41, 79] and with biaxial tests performed on sand that show *dynamic instabilities* at large deformations [80]. The stress drops match with the drops of the fraction of sliding contacts. At this state the system develops force chains highly susceptible to collapse. These chain collapses are result of frictional instabilities that are also observed in earthquake dynamics [42, 43].

We found that particle shape anisotropy determines the inherent anisotropy, namely contact and particle orientations, and also its evolution towards the critical state. The influence of particle shape anisotropy on the mechanical response of granular packing was investigated by means of biaxial compression and periodic shear cells. The critical state is also established to be independent of any particle shape characteristics. A stationary value of the components of the stress tensor, the fabric tensor and the inertia tensor of the particles is stated as a micromechanical requirement for the existence of the critical state at the macro-mechanical level.

By performing biaxial compression of anisotropic samples we showed that the critical state at the global level is not reached since at the micro-mechanical level the coordination number, the fabric and the particle orientation do not converge to a critical value. In the periodic shear cell, in which large deformation can be imposed, the results show that at macro-mechanical level samples with anisotropic particles reach the same critical value for both shear force and void ratio independent of their initial orientation [48]. This global stationary state resembles the critical state and is reached since the micromechanical evolution of the stress, the fabric and particle orientation also attain a critical state. In the case of isotropic particles the orientation of the fabric is dependent on the principal direction of the stress tensor, while for anisotropic particles the fabric orientation is determined by the particle orientation.

Concerning particle rotation, the strong frustration of rotation that anisotropic particles experience due to the larger interlocking among them is manifested in all the experiments and showed to influence the mechanical properties of the granular packing.

The influence of particle shape anisotropy on the critical state parameters can be summarized as follows. The larger the anisotropy,

- the larger the mobilized strength.
- the larger the void ratio, and therefore higher sensibility to volumetric changes.
- the larger the coordination number, although it saturates to a constant value for $\lambda > 2.3$.
- the larger the fabric anisotropy.
- the larger the anisotropy related to particle orientation.
- the smaller the accumulated mean particle rotation.
- the longer the time to reach micro-mechanical equilibrium in fabric and particle orientation.

(ii) We showed that particle shape anisotropy influences the temporal and mechanical stability of granular packings but not the size distribution of the avalanches observed under slow shearing. To this end, we further studied the frictional instabilities observed at the critical state by simulating very slow shear processes as in the case of earthquake faults. We mimic fault zones with transform boundaries, i.e. the boundaries of the tectonic plates are parallel to the direction along which the tectonic plates move [50, 51]. The material inside the fault, *the gouge*, was represented by both isotropic and anisotropic particles.

Avalanches with sizes spanning several orders of magnitude characterized the dynamical response of the system. The probability distribution of the energy released in the avalanches follows a power law behavior over 6 orders of magnitude. This distribution is independent of the particle anisotropy and is in good agreement with the Gutenberg-Richter law [53] describing the distribution of earthquakes. The same behavior is found for different system sizes and at the particle level. Consequently this behavior is an invariant characteristic of the distribution of sizes of avalanches associated with very slow shear processes.

We studied the temporal stability of the granular packing through the sequence of events after a mainshock. The temporal stability of the system is found to depend on the initial configuration of the sample and therefore on the orientation of anisotropic particles. Hence, the differences in the decay observed in realistic earthquake sequences might be explained by the existence of anisotropic gouge within the fault zone. In our numerical simulations the number of aftershocks obeys Omori's law [54], i.e, it decreases with the inverse of time. In particular, we found that the exponents obtained by fitting the sequences are in agreement with the values expected in real observations $0.7 < p < 1.5$. Anisotropic samples with anisotropic particles oriented in the direction of shearing exhibit a smaller value of p and present a more stable configuration. This is a consequence of the larger hindering of the deformation modes such as rotation of the particles. Anisotropic particles oriented perpendicular to the shear direction are less stable since the induced torque is maximized.

We also highlighted the effect of anisotropic particle shape on the mechanical behavior by characterizing the mechanical stability of the system. It involved the calculation of the conditional probability of occurrence of an avalanche for a specific value of stiffness or mobilized strength. We showed that the probability of failure decreases logarithmically with the stiffness and that the exponent of the decay is dependent on the particle shape. Anisotropic systems explore a wider range of stiffness at failure. Regarding mobilized strength, anisotropic samples not only exhibit lower probability of failure for the same strength but also mobilize higher strength values. The distribution of mobilized strength at failure is also dependent on particle anisotropy.

(iii) Finally, we uncovered a numerical problem in the DEM related to the calculation of the tangential forces. The Cundall-Strack spring [2] is usually used to implement such tangential force. This approach is linear in the integration step yielding an error of $O(\Delta t^2)$. This numerical error affects the overall accuracy of the integration scheme. We proposed a new technique that improves the accuracy of the tangential force calculation. It uses quantities from a predictor-corrector integration scheme and therefore the overall error is of the same order as that of the integration scheme.

7.1 Overview

The results and conclusions presented in this thesis provide better comprehension of the role of particle shape on the macro and micro-mechanical response of granular materials. They also show a good agreement with the processes observed in experiments and nature. Despite the efforts towards a proper characterization of particle shape irregularity [24, 75, 152–154] and the understanding of its influence on the overall mechanical response [19, 21, 33, 70, 155], it must be stressed that particle irregularity is still widely disregarded in soil classification systems. Based on previous work and the results presented in this thesis concerning the critical state parameters, we conclude that characterization of particle shape is important and will recognized as an important part of both soil classification and engineering practice. Furthermore, our results on the occurrence of avalanches may have implications in a geophysical context. The large temporal and mechanical stability that we find for systems with anisotropic particles compared to isotropic ones may provide a possible explanation for the variation of the decay rate of aftershocks in earthquake faults. The presence of anisotropic gouge in the shear zone might be thought of as a control parameter on the temporal occurrence of earthquakes.

Many issues still remain to be resolved for a more deeper understanding of sheared granular materials:

First, in our simulations, we retained low stress levels, where dense samples still expand and exhibit a clear peak on the stress behavior [11]. This is due to the fact that our model does not consider fragmentation of the particles. For high stress levels the crushing of the particles is expected to be the primary mechanism of deformation. Experimentally, it was already shown that the initial density state and grain size distribution affects the fragmentation process of the particles [156]. Particle crushing increases with the stress level and affects the mechanical behavior of granular materials, e.g., suppression of dilatancy in dense media [11], reduction of the mobilized shear strength [11, 157], nonlinear behavior of the strength envelope [22] and thus the critical state line for the stress ratio is also not straight [158]. Furthermore, the effect of particle shape, e.g., sphericity and roundness is expected to be suppressed at higher stress levels [159]. In DEM the particle crushing can be implemented either by agglomerates composed of bounded particles that can disaggregate as the stress is increased [1, 72] or by imposing a failure criterion for particle breakage and replacing it by an equivalent set of smaller particles when the criterion is fullfilled [160]. A deeper study of the particle crushing is particularly important in a wide variety of engineering works such as embankments, foundations and pavements where large monotonic and cyclic loading are applied, as well as in geological proccess such as earthquake faults where natural earthquakes occur as a result of the combined effect of frictional instabilities and rock fragmentation.

Second, in order to fully characterize the shape irregularity it is necessary to consider the surface roughness, i.e., the small scale variations of particle surface. Since surface roughness exhibits a fractal character lacking of characteristic scale, it still remains poorly characterized [19]. Despite some previous results where the effect of roughness on the propagation wave parameters was investigated experimentally [161] and with micro-mechanical models[162] the influence of particle roughness at the macromechanical level remains an open issue.

Third, an additional step concerns the generalization of our particle model to a three dimensional system using polyhedra to represent the particles. This is essential for true quantitative characterization of the material. Such a task has already started [163, 164] and it uses a combination of DEM with methods and formulations of multibody systems. It is a very promising tool but is still expensive in terms of the computational time.

Fourth, concerning our numerical improvement of the DEM for the calculation of the tangential force some further improvements are needed. A straightforward implementation to define the initial point during particles collisions has to be undertaken either by interpolating before and after the collision or by using an event-driven scheme till the contact is established. For polygonal particles a proper definition of the contact plane between two polygons is still missing. Preliminary results have shown that a definition based on the shape of the overlap area instead of the intersection points between the particles guarantees the continuous change of the contact plane for any case of contact and therefore a continuous change of the contact forces [165].

Finally, on the occurrence of avalanches, answer to the following questions will help to understand the process that a granular system undergoes during slow shearing. Can the stick-slip fluctuations in granular media be characterized by such natural tendency of the system to build up force chains susceptible to collapse under large shear deformations? Is this succeptibility only related to the existence of the fluidized regions between the force chains? Is failure approached when these regions percolate? Is there any other micro-mechanical signature prior to the failure? To answer these question we require a systematic study of the geometrical properties of the contact network. Current geometrical characterization of force chains has been done for two dimensional packing of disks [47]. The extension of this method for complex shaped particles and the study of the interplay with the fluidized regions will throw light on the nature of the stick-slip fluctuation and the occurrence of avalanches on sheared granular materials.

Bibliography

[1] M. D. Bolton. The role of micro-mechanics in soil mechanics. In Japan Yamaguchi University, editor, *International Workshop on Soil Crushability*, 2000.

[2] P. A. Cundall and O. D. L. Strack. A discrete numerical model for granular assemblies. *Géotechnique*, 29(1):47–65, 1979.

[3] T. Pöschel and T. Schwager. *Computational Granular Dynamics*. Springer, Berlin, 2005.

[4] G. N. Smith and I. G. N. Smith. *Elements of Soil Mechanics*. Blackwell Science, Oxford, 1998.

[5] G. Gudehus. Attractors, percolation thresholds and phase limits of granular soils. In Behringer and Jenkins, editors, *Powders and Grains 1997*. Balkema, 1997.

[6] A.N. Schofield and C.P. Wroth. *Critical State Soil Mechanics*. McGraw Hill, 1968.

[7] R. Chambon, J. Desrues, W. Hammad, and R. Charlier. Cloe, a new rate type constitutive model for geomaterials. theoretical basis and implementation. *Int. J. Anal. Meth. Geomech.*, 18:253–278, 1994.

[8] F. Darve, E. Flavigny, and M. Meghachou. Yield surfaces and principle of superposition: revisit through incrementally non-linear constitutive relations. *International Journal of Plasticity*, 11(8):927, 1995.

[9] G. Gudehus. A comprehensive constitutive equation for granular materials. *Soils and Foundations*, 36(1):1–12, 1996.

[10] D. Kolymbas. An outline of hypoplasticity. *Arch. App. Mech.*, 61:143–154, 1991.

[11] D. M. Wood. *Soil behaviour and critical state soil mechanics*. ISBN: 0-521-33782-8, Cambridge, 1990.

[12] A. Casagrande. Characteristics of cohensionless soils affecting the stability of slopes and earth fills. *J. Boston Soc. Civil Engineers*, 23(1):13–32, 1936.

[13] A. W. Bishop and D. J. Henkel. *The measurement of soil properties in the triaxial test*. William Arnold, London, 1957.

[14] K. H. Roscoe, A. N. Schofield, and C. P. Wroth. On the yielding of soils. *Geotechnique*, 8:22–53, 1958.

[15] G. Castro. Liquefaction and cyclic mobility of saturated sands. *Journal of the Soil Mechanics and Foundations Division*, 101(6):551–569, 1975.

[16] R. Verdugo and K. Ishihara. The steady state of sandy soils. *Soils and foundations*, 36(2):81–91, 1996.

[17] R. J. Finno and A. L. Rechenmacher. Effects of consolidation history on critical state of sand. *J. Geotech. Geoenviron. Eng.*, 129(4):350, 2003.

[18] M. A. Mooney, R. J. Finno, and M.G. Viggiani. A unique critical state for sands? *J. Geotech. Geoenviron. Eng.*, 124(11):1100, 1998.

[19] G.-C. Cho, J. Dodds, and J. C. Santamarina. Particle shape effects on packing density, stiffness and strength: natural and crushed sands. *J. Geotech. Eng.*, 132(5):561–602, 2006.

[20] A. Mirghasemi, L. Rothenburg, and E. Matyas. Influence of particle shape on engineering properties of assemblies of two-dimensional polygon-shaped particles. *Geotechnique*, 52:209–217, 2002.

[21] J.C. Santamarina and G.C. Cho. Soil behaviour: The role of particle shape. In London Thomas Telford, editor, *Advances in Geotechnical Engineering: The Skempton Conference*, 2004.

[22] J. P. Bardet. *Experimental Soil Mechanics*. Prentice Hall, New Jersey, 1997.

[23] T. W. Lambe and R. V. Whitman. *Soil mechanics*. John Wiley & Sons Inc, 1969.

[24] W.C. Krumbein and L. L. Sloss. *Stratigraphy and Sedimentation*. Freeman and Company, San Francisco, CA, 1963.

[25] University of Nevada. Quartz sand grains excavated 4 meters below the ground surface, hwange national park, zimbabwe. http://www.unr.edu/cla/anthro/SandGrainsSEM2.gif.

[26] J. A. Aström, H. J. Herrmann, and J. Timonen. Granular packings and fault zones. *Phys. Rev. Lett.*, 84(4):638–641, 2000.

[27] F. Radjai, M. Jean, J. J. Moreau, and S. Roux. Force distribution in dense two-dimensional granular systems. *Phys. Rev. Lett.*, 77(2):274, 1996.

[28] L. Staron, J. P. Vilotte, and F. Radjai. Preavalanche instabilities in a granular pile. *Phys. Rev. Lett.*, 89(20):204302, 2002.

[29] S. Abe, S. Latham, and P. Mora. Dynamic rupture in a 3-d particle-based simulation of a rough planar fault. *Pure Appl. Geophys.*, 163(9):1881–1892, 2006.

[30] C. Thornton. Numerical simulations of deviatoric shear deformation of granular media. *Geotechnique*, 50:43–53, 2000.

[31] J. P. Bardet. Observations on the effects of particle rotations on the failure of idealized granular materials. *Mechanics of Materials*, 18:159–182, 1994.

[32] M. Oda, J. Konishi, and S. Nemat-Nasser. Experimental micromechanical evaluation of strength of granular materials: Effects of particle rolling. *Mechanics of Materials*, 1:269–283, 1982.

[33] H. M. Shodja and E. G. Nezami. A micromechanical study of rolling and sliding contacts in assemblies of oval granules. *Int. J. Numer. Anal. Meth. Geomech.*, 27:403–424, 2003.

[34] F. Alonso-Marroquin and H.J. Herrmann. Ratcheting of granular materials. *Phys. Rev. Lett.*, 92:054301, 2004. cond-mat/0403065.

[35] R. García-Rojo, F. Alonso-Marroquin, and H. Herrmann. Characterization of the material response in the granular ratcheting. *Phys.Rev.E.*, 72(041302), 2005.

[36] J. Desrues. *Localization de la deformation plastique dans les materieux granulaires*. University of Grenoble, France, 1984.

[37] H.-J. Tillemans and H. J. Herrmann. Simulating deformations of granular solids under shear. *Physica A*, 217:261–288, 1995.

[38] R. García-Rojo, S. McNamara, A. A. Peña, and H. Herrmann. Sliding and localization in a biaxial test of granular material. In R. García-Rojo, H.J. Herrmann, and S. McNamara, editors, *Powders and Grains 2005*, pages 705–708. Balkema, 2005.

[39] A. A. Peña, A. Lizcano, F. Alonso-Marroquín, and H. J. Herrmann. Biaxial test simulations using a packing of polygonal particles. *Int. J. Numer. Anal. Meth. Geomech.*, 32:143–160, 2007.

[40] S. Nasuno, A. Kudrolli, A. Bank, and J. P. Gollub. Time-resolved studies of stick-slip friction in sheared granular layers. *Phys. Rev. E*, 58(2):2161–2171, 1998.

[41] P. Evesque and F. Adjémian. Stress fluctuations and macroscopic stick-slip in granular materials. *Eur. Phys. J. E*, 9:223–259, 2002.

[42] F. Alonso-Marroqun, I. Vardoulakis, H. J. Herrmann, D. Weatherley, and P. Mora. Effect of rolling on dissipation in fault gouges. *Phys. Rev. E*, 74:031306, 2006.

[43] P. Mora and D. Place. Simulation of the frictional stick-slip instability. *PAGEOPH*, 143:61, 1994.

[44] F. Nicot and F. Darve. A multiscale approach to granular materials. *Mech. mater.*, 37(9):980–1006, 2005.

[45] M. E. Cates, J. P. Wittmer, J.-P. Bouchaud, and P. Claudin. Jamming, force chains, and fragile matter. *Phys. Rev. Lett.*, 81(9):1841–1844, 1998.

[46] T. S. Majmudar and R. P. Behringer. Contact force measurements and stress-induced anisotropy in granular materials. *Nature*, 435(23):1079–1082, 2005.

[47] J. F. Peters, M. Muthuswamy, J. Wibowo, and A. Tordesillas. Characterization of force chains in granular material. *Phys. Rev. E*, 72:041307, 2005.

[48] A. A. Peña, R. García-Rojo, and H. J. Herrmann. Influence of particle shape on sheared dense granular media. *Granular Matter*, 9:279–291, 2007.

[49] B. Wilson, T. Dewers, Z. Reches, and J. Brune. Particle size and energetics of gouge from earthquake rupture zone. *Nature*, 434:749–752, 2005.

[50] B. A. Bolt. *Earthquakes*. W. H. Freeman and Company, New York, 2005.

[51] D. L. Turcotte and G. Schubert. Cambridge University Press, Cambridge, 2002.

[52] J. P. sethna, K. A. Dahmen, and C. R. Myers. Crackling noise. *Nature*, 410:242–250, 2001.

[53] B. Gutenberg and C. F. Richter. *Seismicity of the Earth and Associated Phenomena*. Princeton Uni. Press, 1954.

[54] F. Omori. On the aftershocks of earthquakes. *J. Coll. Sci. Imper. Univ. Tokyo*, 7:111, 1895.

[55] S. Luding. *Die Physik trockener granularer Medien*. Logos Verlag, Berlin, 1998. Habilitation thesis (in german), ISBN 3-89722-064-4.

[56] M. P. Allen and D. J. Tildesley. *Computer Simulation of Liquids*. Oxford University Press, Oxford, 2003.

[57] S. Luding, E. Clément, A. Blumen, J. Rajchenbach, and J. Duran. Studies of columns of beads under external vibrations. *Phys. Rev. E*, 49(2):1634, 1994.

[58] P. A. Thompson and G. S. Grest. Granular flow: Friction and the dilatancy transition. *Phys. Rev. Lett.*, 67(13):1751, 1991.

[59] A. A. Peña, P.G. Lind, S. McNamara, and H. J. Herrmann. Numerical improvement of the discrete element method applied to shear of granular media. *Submitted to Acta Mechanica*, cond-mat arXiv:0709.3716v1, 2007.

[60] H. M. Jaeger, S. R. Nagel, and R. P. Behringer. Granular solids, liquids, and gases. *Reviews of Modern Physics*, 68(4):1259–1273, 1996.

[61] Indymedia UK. Yanacocha, perú, the worlds largest gold mine. http://www.indymedia.org.uk/ images/2007/04/368706.jpg.

[62] ActewAGL. Corin dam, earth and rockfill embankment dam with side channel spillway, completed in 1967. http://www.actewagl.com.au/water/images/corin.jpg.

[63] U.S. Geological Survey (USGS). Landslides. http://3dparks.wr.usgs.gov/ landslide/landslides.html.

[64] Water Encyclopedia. San andreas fault, california, u.s. http://www. waterencyclopedia.com/images/wsci03img0412.jpg.

[65] A. Casagrande and N. Carillo. Shear failure of anisotropic materials. In *Proc. Boston Soc. Civil Engrs 31.*, pages 74–78, 1944.

[66] M. Oda, S. Nemat-Nasser, and J. Konishi. Stress-induced anisotropy in granular masses. *Soils Found.*, 25(3):85–97, 1985.

[67] M. Oda and H. Nakayama. Introduction of inherent anisotropy of soils in the yield function. In M. Satake and J. T. Jenkins, editors, *Micromechanics of granular materials*, pages 81–90. Elsevier, 1988.

[68] X. S. Li and Y. F. Dafalias. Constitutive modeling of inherently anisotropic sand behavior. *J. Geotech. Geoenviron. Engng.*, 128(10):868–880, 2002.

[69] H. Ehrentraut and A. Chrzanowska. Induced anisotropy in rapid flows of non-spherical granular materials. In K. Hutter and N. P. Kirchner, editors, *Dynamic Response of Granular and Porous Materials under Large and Catastrophic Deformations*, pages 343–364, Berlin, 2003. Springer Verlag.

[70] E.T Bowman and K. Soga. The influence of particle shape on the stress-strain and creep response of fine silica sand. In R. García-Rojo, H.J. Herrmann, and S. McNamara, editors, *Powders and Grains 2005*, pages 1325–1328. Balkema, 2005.

[71] I. Herle and G. Gudehus. Determination of parameters of a hypoplastic constitutive model from properties of grain assemblies. *Mechanics of Cohesive-Frictional Materials*, 4:461–486, 1999.

[72] Y. P. Cheng, Y. Nakata, and M. D. Bolton. Discrete element simulation of crushable soil. *Geoteéchnique*, 53:633–641, 2003.

[73] Y. P. Cheng, M. D. Bolton, and Y. Nakata. Crushing and plastic deformation of soils simulated using dem. *Geoteéchnique*, 54:131–141, 2004.

[74] G. R. McDowell and M. D. Bolton. On the micromechanics of crushable aggregates. *Géotechnique*, 48(5):667–679, 1998.

[75] E. T. Bowman, K. Soga, and W. Drummond. Particle shape characterization using fourier descriptor analysis. *Géotechnique*, 51(6):545–554, 2001.

[76] C. Nouguier-Lehon, B. Cambou, and E. Vincens. Influence of particle shape and angularity on the behavior of granular materials: a numerical analysis. *Int. J. Numer. Anal. Meth. Geomech.*, 27:1207–1226, 2003.

[77] Wikimedia. Natural gravel on a beach in thirasia, greece. http:// commons.wikimedia.org/wiki/Image:GravelonabeachinThirasiaSantoriniGreece.jpg.

[78] Federal Higway administration U.S. Department of transportation. http://www.fhwa.dot.gov/pavement/pccp/pubs/04150/appendd.cfm.

[79] F. Adjemian amd P. Evesque and X. Jia. Ultrasonic experiment coupled with triaxial test for micro-seismicity detection in granular media. In R. García-Rojo, H.J. Herrmann, and S. McNamara, editors, *Powders and Grains 2005*, pages 281–285. Balkema, 2005.

[80] I. Vardoulakis and I. O. Georgopoulos. The stress - dilatancy hypothesis revisited: shear - banding related instabilities. *Soils & Foundations*, 45:61–76, 2005.

[81] P. Mora and D. Place. The weakness of earthquake faults. *Geophys. Res. Lett.*, 26(1):123–126, 1999.

[82] F. Alonso-Marroquin. *Micromechanical investigation of soil deformation: incremental response and granular ratcheting*. PhD thesis, University of Stuttgart, Stuttgart, Germany, 2004.

[83] Ferenc Kun and Hans J. Herrmann. Transition from damage to fragmentation in collision of solids. *Phys. Rev. E*, 59(3):2623–2632, 1999.

[84] H.-G. Matuttis and A. Schinner. Influence of the geometry on the pressure distribution of granular heaps. *Granular Matter*, 1(4):195–201, 1999.

[85] F. Kun and H. J. Herrmann. Fragmentation of colliding discs. *Int. J. of Mod. Phys. C*, 7(6):837–855, 1996.

[86] H. Hertz. Über die Berührung fester elastischer Körper. *J. für die reine u. angew. Math.*, 92:136, 1882.

[87] H.-G. Matuttis. Simulations of the pressure distribution under a two dimensional heap of polygonal particles. *Granular Matter*, 1(2):83–91, 1998.

[88] H.-G. Matuttis and S. Luding. The effect of particle shape and friction on the stresses in heaps of granular media. In D. E. Wolf and P. Grassberger, editors, *Friction, Arching and Contact Dynamics*, Singapore, 1997. World Scientific.

[89] F. Alonso-Marroquin, S. Luding, H.J. Herrmann, and I. Vardoulakis. Role of the anisotropy in the elastoplastic response of a polygonal packing. *Phys. Rev. E*, 51:051304, 2005.

[90] S. McNamara, R. Garcia-Rojo, and H.J.Herrmann. Microscopic origin of granular ratcheting. *submitted to Phys. Rev. E*, 2007.

[91] S. F. Foerster, M. Y. Louge, H. Chang, and K. Allia. Measurements of the collision properties of small spheres. *Phys. Fluids*, 6(3):1108–1115, 1994.

[92] E. Rougier, A. Munjiza, and N.W.M. John. Numerical comparison of some explicit used in dem, *Int. J. Numer. Meth. Eng*, 61:856, 2004.

[93] C. Moukarzel and H. J. Herrmann. A vectorizable random lattice. *Journal of Statistical Physics*, 68:911–923, 1992.

[94] K.B. Lauritsen, C. Moukarzel, and H.J. Herrmann. Statistical laws and mechanics of voronoi random lattices. *J. of Physique I*, 3:1941–1951, 1993.

[95] A. Okabe, B. Boots, and K. Sugihara. *Spatial Tesselations, Concepts and Applications of Voronoi Diagrams*. Wiley series in probability and mathematical statistics. John Wiley & Sons, Chichester, England, 1992.

[96] R. García-Rojo and H. Herrmann. Shakedown of granular materials. *Granular Matter*, 7(2-3):109–118, 2005. cond-mat 0404176.

[97] F. Alonso-Marroquin, , H.J. Herrmann, and I. Vardoulakis. Micromechanical aspects of soil plasticity: an investigation using a discrete model of polygonal particles. In P. A.i Vermeer, W. Ehlers, H. J. Herrmann, and E. Ramm, editors, *Modelling of cohesive-frictional Materials*, pages 45–69, 2004.

[98] L. Rothenburg and A. P. S. Selvadurai. A micromechanical definition of the cauchy stress tensor for particulate media. In A. P. S. Selvadurai, editor, *Mechanics of Structured Media*, pages 469–486. Elsevier, 1981.

[99] J. Desrues. Experimental characterization of failure, degradation and instability in geomaterials. In *Failure, degradation and instabilities*, 2004.

[100] J. Arthur, T. Dunstan, Q. Al-Ani, and A. Assadi. Plastic deformation and failure in granular media. *Géotechnique*, 27:53–74, 1977.

[101] I. Vardoulakis, M. Goldscheider, and G. Gudehus. Formation of shear bands in sand bodies as a bifurcation problem. *Int. J. Numer. Anal. Meth. Geomech.*, 2:99–128, 1978.

[102] Gaël Combe and Jean-Noël Roux. Strain versus stress in a model granular material: a devil's staircase. *Phys. Rev. Lett.*, 85(17):3628–3631, 2000. cond-mat/0004062.

[103] A. A. Peña, A. Lizcano, F. Alonso-Marroquín, and H. J. Herrmann. Investigation of the asymptotic states of granular materials using a discrete model of anisotropic particles. In R. García-Rojo, H.J. Herrmann, and S. McNamara, editors, *Powders and Grains 2005*, pages 697–700. Balkema, 2005.

[104] L. Zhang and C. Thornton. Characteristics of granular media at the critical state. In R. García-Rojo, H.J. Herrmann, and S. McNamara, editors, *Powders and Grains 2005*, pages 267–270. Balkema, 2005.

[105] I. Vardoulakis. Shear band inclination and shear modulus of sand in biaxial tests. *Int. J. Numer. Anal. Meth. Geomech.*, 4:103–119, 1980.

[106] P. A. Cundall. Numerical experiments on localization in frictional materials. *Ingenieur-Archiv*, 59:148–159, 1989.

[107] J. P. Bardet and J. Proubet. A numerical investigation of the structure of persistent shear bands in granular media. *Geotechnique*, 41(4):599–613, 1991.

[108] P. A. Vermeer. The orientation of shear bands in biaxial tests. *Géotechnique*, 40:223, 1990.

[109] K. H. Roscoe. The influence of the strains in soil mechanics. *Geotechnique*, 20(2):129–170, 1970.

[110] A. Skinner. A note on the influence of interparticle friction on the shearing strength of a random assembly of spherical particles. *Geotechnique*, 19(1):150–157, 1969.

[111] B. Cambou. From global to local variables in granular materials. In C. Thornton, editor, *Powders and Grains 93*, pages 73–86. Balkema, 1993.

[112] N. P. Kruyt and L. Rothenburg. Strength, dilatancy, energy and dissipation in quasi-static deformation of granular materials. In R. García-Rojo, H.J. Herrmann, and S. McNamara, editors, *Powders and Grains 2005*, pages 251–255. Balkema, 2005.

[113] M. Oda. Initial fabrics and their relations to mechanical properties of granular materials. *Soils Found.*, 12(1):17–36, 1972.

[114] L. Rothenburg and R. J. Bathurst. Analytical study of induced anisotropy in idealized granular materials. *Géotechnique*, 39(4):601–614, 1989.

[115] C. Nouguier-Lehon and E. Frossard. Influence of particle shape on rotations and rolling movements in granular media. In R. García-Rojo, H.J. Herrmann, and S. McNamara, editors, *Powders and Grains 2005*, pages 1339–1343. Balkema, 2005.

[116] M. Cubrinovski and K. Ishihara. Maximum and minimum void ratios characterictics of sands. *Soils and foundations*, 42(6):65–78, 2002.

[117] M. D. Bolton. The strength and dilatancy of sands. *Géotechnique*, 36(1):65–78, 1986.

[118] M. Oda, H. Kazama, and J. Konishi. Effect of induced anisotropy on the development of shear bands in granular materials. *Mechanics of materials*, 28:103–111, 1998.

[119] H. Ouadfel and L. Rothenburg. Stress-force-fabric' relationship for assemblies of ellipsoids. *Mechanics of Materials*, 33(4):201–221, 2001.

[120] L. Rothenburg and R. J. Bathurst. Micromechanical features of granular assemblies with planar elliptic particles. *Géotechnique*, 42(1):79–95, 1992.

[121] C. T. Veje, D. W. Howell, and R. P. Behringer. Kinematics of a 2D granular Couette experiment at the transition to shearing. *Phys. Rev. E*, 59:739, 1999.

[122] D. Howell, R. P. Behringer, and C. Veje. Stress fluctuations in a 2d granular Couette experiment: A continuous transition. *Phys. Rev. Lett.*, 82:5241, 1999.

[123] C. Thornton and L. Zhang. A dem comparison of different shear testing devices. In Kishino, editor, *Powders and Grains 2001*, pages 183–190. Balkema, 2001.

[124] M. Lätzel, S. Luding, and H. J. Herrmann. Macroscopic material properties from quasi-static, microscopic simulations of a two-dimensional shear-cell. *Granular Matter*, 2(3):123–135, 2000.

[125] FEMA Federal Emergency Managment Agency US. http://www.fema.gov.

[126] Nature debate: Earthquake prediction. http://www.nature.com/nature/debates/.

[127] F. Donzé, P. Mora, and S.-A. Magnier. Numerical simulation of faults and shear zones. *Geophys. j. Int.*, 116:46–52, 1994.

[128] P. Mora and D. Place. Stress correlation function evolution in lattice solid elasto-dynamic models of shear and fracture zones and earthquake prediction. *Pure appl. geophys.*, 159(10):2413–2427, 2002.

[129] L. R. Sykes, B. E. Shaw, and C. H. Scholz. Rethinking earthquake prediction. *Pure. appl. geophys.*, 155:207–232, 1999.

[130] K. Mair, K. M. Frye, and C. Marone. Influence of grain characteristics on the friction of granular shear zones. *J. Geophys. Res.*, 107:2219, 2002.

[131] C. Marone. Laboratory-derived friction laws and their application to seismic faulting. *Annual Review of Earth and Planetary Sciences*, 26:643–696, 1998.

[132] R. Summers and J. D. Byerlee. A note on the effect of fault gouge composition on the stability of frictional sliding. *Int. J. Rock Mech. Min. Sci.*, 14(3):155–160, 1977.

[133] P. Mora and D. Place. Numerical simulation of earthquake faults with gouge: toward a comprehensive explanation for the heat flow paradox. *J. Geophys. Res.*, 103:21067–21089, 1998.

[134] C. H. Scholz. *The mechanics of earthquakes and faulting*. Cambridge university press, 2002.

[135] W. J. Morgan. Rises, trenches, great faults, and crustal blocks. *J. Geophys. Res.*, 73:1959–1982, 1968.

[136] Nasa's Observatorium. http:// observe.arc.nasa.gov/nasa/earth/tectonics/ Tectonics2.html.

[137] Nasa Planetary Geodynamics Laboratory. http://denali.gsfc.nasa.gov/dtam/seismic/.

[138] Nevada sismological laboratory. http://www.seismo.unr.edu/ftp/pub/louie/class/.

[139] H. Kanamori and E. E. Brodsky. The physics of earthquakes. *Physics today*, 54:34–40, 2001.

[140] K. B. Chakrabarti and L. G. Benguigui. *Statistical physics of fracture and breakdown in disordered systems*. Clarendon, Oxford, 1997.

[141] A. Papoulis. *Probability, random variables, and stochastic processes*. McGraw-Hill, Boston, 2002.

[142] H. J.S. Feder and J. Feder. Self-organized criticality in a stick-slip process. *Phys. Rev. Lett.*, 66(20):2669–2672, 1991.

[143] L. Staron and F. Radjai. Friction versus texture at the approach of a granular avalanche. *Phys. Rev. E*, 72:041308, 2005.

[144] F. Radjai, D. E. Wolf, M. Jean, and J.-J. Moreau. Bimodal character of stress transmission in granular packings. *Phys. Rev. Lett.*, 80(1):61–64, 1998.

[145] L. Staron, F. Radjai, and J. P. Vilotte. Granular micro-structure and avalanche precursors. *J. Stat. Mech.*, P07014, 2006.

[146] F. Alonso-Marroquin, A.A Peña, H.J. Herrmann, and P. Mora. Simulation of shear bands using polygonal particles. In *Discrete Element Methods (DEM) Conference.*, 2007.

[147] M.P. Ciamarra, A. Coniglio, and M. Nicodemi. Shear instabilities in granular mixtures. *Phys. Rev. Lett.*, 94:188001, 2005.

[148] F. da Cruz, S. Eman, M. Prochnow, and J.N. Roux. Rheophysics of dense granular materials: Discrete simulation of plane shear flows. *Phys. Rev. E.*, page 021309, 2005.

[149] S. Luding, E. Clément, A. Blumen, J. Rajchenbach, and J. Duran. Anomalous energy dissipation in molecular dynamics simulations of grains: The "detachment effect". *Phys. Rev. E*, 50:4113, 1994.

[150] S. Luding. Collisions & contacts between two particles. In H. J. Herrmann, J.-P. Hovi, and S. Luding, editors, *Physics of dry granular media - NATO ASI Series E350*, page 285, Dordrecht, 1998. Kluwer Academic Publishers.

[151] S. Latham, S. Abe, and P. Mora. Macroscopic friction response of rotational and non-rotational lattice solid gouge models in 2d and 3d. In R. García-Rojo, H.J. Herrmann, and S. McNamara, editors, *Powders and Grains 2005*, pages 213–217. Balkema, 2005.

[152] P. J. Barrett. The shape of rock particles, a critical review. *Sedimentology*, 27:291–303, 1980.

[153] R. L. Folk. Student operator error in determination of roundness, sphericity, and grain size. *J. Sediment. Petrol.*, 25(4):297–301, 1955.

[154] T. Matsushima and H. Saomoto. Discrete element modeling for irregularly-shaped sand grains. In Mestat, editor, *Proc. NUMGE2002: Numerical Methods in Geotechnical Engineering*, pages 239–246, 2002.

[155] T. T. Ng. Behavior of ellipsoids of two sizes. *J. Geotech. Geoenviron. Engng, ASCE*, 130(10):1077–1083, 2004.

[156] Y. Nakata, M. Hyodo, A. Hyde, Y. Kato, and H. Murata. Microscopic particle crushing of sand subjected to high pressure one-dimensional compression. *Soils and foundations*, 41(1):69–82, 2001.

[157] S. Lobo-Guerrero and L. E. Vallejo. Discrete element method evaluation of granular crushing under direct shear test conditions. *J. Geotech. Eng.*, 131(10), 2005.

[158] Y. P. Cheng, M. D. Bolton, and Y. Nakata. Grain crushing and critical states observed in dem simulations. In R. García-Rojo, H.J. Herrmann, and S. McNamara, editors, *Powders and Grains 2005*, pages 1393–1397. Balkema, 2005.

[159] J. Feda. Notes on the effect of grain crushing on the granular soil behavior. *Engineering geology*, 63(1-2):93–98, 2002.

[160] J. A. Aström and H. J. Herrmann. Fragmentation of grains in a two-dimensional packing. *Eur. Phys. J. B*, (5):551–554, 1998.

[161] J. C. Santamarina and G. Cascante. effect of surface roughness on wave propagation parameters. *Geotechnique*, 48(1):129–137, 1998.

[162] S. Yimsri and K. Soga. Effect of surface roughness on small strain stiffness of soils - micromechanical approach. In *Pre-failure deformation characteristics of geomaterials IS-Torino*, pages 597–602, Lancellotta & Lo Presti, 1999.

[163] B. Muth and P. Eberhard. Investigation of large systems consisting of many spatial polyhedral bodies. In M.D. Lazurko D.H. van Campen and W.P.J.M. van der Oever, editors, *Proceedings of the ENOC-2005 Fifth EUROMECH Nonlinear Dynamics Conference*, pages 1644–1650, 2004.

[164] B. Muth, P. Eberhard, and S. Luding. Simulation of contacting spatial polyhedral particles. In *Proceedings of the XXI. ICTAM 2004*, pages 1–2, 2004.

[165] A. A. Peña, P.G. Lind, and H. J. Herrmann. Modeling slow deformation of polygonal particles using dem. *Submitted to Particuology*, cond-mat arXiv:0712.0919v1, 2007.

Curriculum Vitae

Name:	Andrés Alfonso Peña Olarte
Birth:	June 21st, 1977, Manizales, Colombia
Parents:	Samuel Peña and Esther Olarte, Tunja, Colombia
Feb 82 - Nov 94	School education. Colegio San luis Gonzaga, Manizales, Colombia.
Jan 95 - Jul 00	Degree in Civil Engineering, Universidad Nacional de Colombia, Manizales, Colombia.
May 00 - Jul 02	Junior engineer, Laboratory of Materials and Quality Control of Roller Compacted Concrete, Hydroelectric Project Miel I, Ingetec S.A. Norcasia, Colombia.
Aug 02 - Mar 04	Master Degree in Civil Engineering, Universidad de los Andes, Bogotá, Colombia.
	Scholarship of the Civil Engineering Department, Universidad de los Andes, Bogotá, Colombia.
Sep 04 - Nov 07	PhD. Researcher of Civil Engineering, Institute of Computer Physics, University of Stuttgart, Germany.
Dec 07 -	Geotechnical Project Engineer, Structural Design, Civil, Bilfinger Berger AG, Wiesbaden, Germany.

Mitteilungen des Instituts für Geotechnik

Nr. 01	Thamm, B. R.	(1974)	Anfangssetzungen und Anfangsporenwasserüberdrücke eines normalverdichteten wassergesättigten Tones.	5,11 €
Nr. 02	Gußmann, P.	(1975)	Einheitliche Berechnung von Grundbruch und Böschungsbruch.	2,56 €
Nr. 03	Feeser, V.	(1975)	Die Bedeutung des Kalziumkarbonats für die bodenphysikalischen Eigenschaften vom Löß.	Vergriffen
Nr. 04	Du Thin, K.	(1976)	Standsicherheit von Böschungen: Programm-Dokumentation.	Vergriffen
Nr. 05	Smoltczyk, U. / Pertschi, O. / Hilmer, K.	(1976)	Messungen an Schleusen in der UDSSR. Schleusennorm der UDSSR (SN 30365).	Vergriffen
Nr. 06	Hilmer, K.	(1976)	Erddruck auf Schleusenkammerwände.	9,20 €
Nr. 07	Laumans, Q.	(1977)	Verhalten einer ebenen, in Sand eingespannten Wand bei nichtlinearen Stoffeigenschaften des Bodens.	9,20 €
Nr. 08	Lächler, W.	(1977)	Beitrag zum Problem der Teilflächenpressung bei Beton am Beispiel der Pfahlkopfanschlüsse.	Vergriffen
Nr. 09	Spotka, H.	(1977)	Einfluß der Bodenverdichtung mittels Oberflächenrüttelgeräten auf den Erddruck einer Stützwand bei Sand.	Vergriffen
Nr. 10	Schad, H.	(1979)	Nichtlineare Stoffgleichungen für Böden und ihre Verwendung bei der numerischen Analyse von Grundbauaufgaben.	

			Vergriffen
Nr. 11	Ulrich, G.	(1980)	Verschiebungs- und kraftgesteuerte Plattendruckversuche auf konsolidierenden Böden.
	Gußmann, P.		Zum Modellgesetz der Konsolidation.
			10,23 €
Nr. 12	Salden, D.	(1980)	Der Einfluß der Sohlenform auf die Traglast von Fundamenten.
			12,78 €
Nr. 13	Seeger, H.	(1980)	Beitrag zur Ermittlung des horizontalen Bettungsmoduls von Böden durch Seitendruckversuche im Bohrloch.
			12,78 €
Nr. 14	Schmidt, H.H.	(1981)	Beitrag zur Ermittlung des Erddrucks auf Stützwände bei nachgiebigem Baugrund.
			12,78 €
Nr. 15	Smoltczyk, U. / Schweikert, O.	(1981)	Vorstudie über bauliche Alternativen für Durchgangsstraßen in Siedlungen.
			6,14 €
Nr. 16	Malcharek, K. / Smoltczyk, U.	(1981)	Vergleich nationaler Richtlinien für die Berechnung von Fundamenten.
			7,67 €
Nr. 17	Gruhle, H.D.	(1981)	Das Verhalten des Baugrundes unter Einwirkung vertikal gezogener Ankerplatten als räumliches Problem des Erdwiderstandes.
			Vergriffen
Nr. 18	Kobler, W.	(1982)	Untersuchungen über Böschungs- und Grundbruch bei begrenzten Lastflächen.
			12,78 €
Nr. 19	Lutz, W.	(1983)	Tragfähigkeit des geschlitzten Baugrunds neben Linienlasten.
			12,78 €
Nr. 20	Smoltczyk, U.	(1983)	Studienunterlagen Bodenmechanik und Grundbau; überarbeitete Ausgabe 1983.
			20,45 €

Nr. 21	Schweikert, O.	(1984)	Der Einfluß des Böschungswinkels auf die Berechnung des aktiven Erddrucks.
			10,23 €
Nr. 22	Vogt, N.	(1984)	Erdwiderstandsermittlung bei monotonen und wiederholten Wandbewegungen in Sand.
			Vergriffen
Nr. 23	Buchmaier, R.	(1985)	Zur Berechnung von Konsolidationsproblemen bei nichtlinearem Stoffverhalten.
			12,78 €
Nr. 24	Schad, H.	(1985)	Möglichkeiten der Böschungssicherung bei kleinen Baugruben.
	Smoltczyk, U. / Schad, H. / Zoller, P.		Sonderkonstruktionen der Böschungssicherung.
			17,90 €
Nr. 25	Gußmann, P.	(1986)	Die Methode der Kinematischen Elemente.
			10,23 €
Nr. 26	Steinmann, B.	(1985)	Zum Verhalten bindiger Böden bei monotoner einaxialer Beanspruchung.
			Vergriffen
Nr. 27	Lee, S.D.	(1987)	Untersuchungen zur Standsicherheit von Schlitzen im Sand neben Einzelfundamenten.
			Vergriffen
Nr. 28	Kolb, H.	(1988)	Ermittlung der Sohlreibung von Gründungskörpern unter horizontalem kinematischen Zwang.
			12,78 €
Nr. 29	Ochmann, H.	(1988)	Ebene Grenzzustände von Erdböschungen im stochastischen Sicherheitskonzept.
			12,78 €
Nr. 30	Breinlinger, F.	(1989)	Bodenmechanische Stoffgleichungen bei großen Deformationen sowie Be- und Entlastungsvorgängen.
			15,34 €
Nr. 31	Smoltczyk, U. / Breinlinger, F. / Schad, H. / Wittlinger, M.	(1989)	Beitrag zur Bemessung von Tunneln in offener Bauweise.
			12,78 €

Nr. 32	Gußmann, P. / Schanz, T. / Smoltczyk, U. / Willand, E.	(1990)	Beiträge zur Anwendung der KEM (Erddruck, Grundbuch, Standsicherheit von Böschungen) Vergriffen
Nr. 33	Gruhle, H.D.	(1990)	Der räumliche Erdwiderstand vor überwiegend horizontal belasteten Ankerplatten. Vergriffen
Nr. 34	Henne, J.	(1995)	Zur Bewehrung von verformten Bodenschichten durch Einsatz zugfester Geokunststoffe. 15,34 €
Nr. 35	Wittlinger, M.	(1994)	Ebene Verformungsuntersuchungen zur Weckung des Erdwiderstandes bindiger Böden. 15,34 €
Nr. 36	Schad, H.	(1992)	Zeit- und geschwindigkeitsabhängiges Materialverhalten in der Geotechnik – Experimentelle Erfassung und numerische Analyse. 15,34 €
Nr. 37	Belz, I.	(1992)	Zur Ermittlung dynamischer Bodenkennwerte in situ aus der Systemantwort des Erregers. 15,34 €
Nr. 38	Ma, J.	(1994)	Untersuchungen zur Standsicherheit der durch Stützscheiben stabilisierten Böschungen. 15,34 €
Nr. 39	Smoltczyk, U.	(1994)	Sonderheft: 25 Jahre Lehre und Forschung in der Geotechnik. 15,34 €
Nr. 40	Rilling, B.	(1994)	Untersuchungen zur Grenztragfähigkeit bindiger Schüttstoffe am Beispiel von Lößlehm. 17,90 €
Nr. 41	Vermeer, P.A.	(1996)	Deponiebau und Geotechnik. 17,90 €
Nr. 42	Vermeer, P.A.	(1997)	Baugruben in Locker- und Festgestein. 17,90 €
Nr. 43	Brinkmann, C.	(1998)	Untersuchungen zum Verhalten von Dichtungsübergängen im Staudammbau. 17,90 €

Nr. 44	Fiechter-Scharr, I.	(1998)	Beeinflussung von Erdbaustoffen durch Beimischen eines organophilen Bentonits. 17,90 €
Nr. 45	Schanz, T.	(1998)	Zur Modellierung des mechanischen Verhaltens von Reibungsmaterialien. 17,90 €
Nr. 46	Akinrogunde, A.E.	(1999)	Propagation of Cement Grout in Rock Discontinuities Under Injection Conditions. 17,90 €
Nr. 47	Vogt-Breyer, C.	(1999)	Experimentelle und numerische Untersuchungen zum Tragverhalten und zur Bemessung horizontaler Schraubanker. 17,90 €
Nr. 48	Vermeer, P.A.	(1999)	Neue Entwicklungen in der Geotechnik. 17,90 €
Nr. 49	Marcher, T.	(2002)	Resultate eines Versuchsprogramms an Beaucaire-Mergel. 17,90 €
Nr. 50	Marcher, T.	(2003)	Nichtlokale Modellierung der Entfestigung dichter Sande und steifer Tone. 17,90 €
Nr. 51	Ruse, N.M.	(2004)	Räumliche Betrachtung der Standsicherheit der Ortsbrust beim Tunnelvortrieb. 17,90 €
Nr. 52	Beutinger, P.H.	(2005)	Ein geotechnischer Beitrag zur Standsicherheit mobiler Baumaschinen. 17,90 €
Nr. 53	Wehnert, M.	(2006)	Ein Beitrag zur drainierten und undrainierten Analyse in der Geotechnik. 17,90 €
Nr. 54	Möller, S.C.	(2006)	Tunnel induced settlements and forces in linings 17,90 €
Nr. 55	Benz, T.	(2007)	Small-Strain Stiffness of Soils and its Numerical Consequences. 17,90 €

Nr. 56	Abed, A.	(2008)	Numerical Modeling of Expansive Soil Behavior.
			17,90 €
Nr. 57	Hintner, J.	(2008)	Analyse der Fundamentverschiebungen infolge vertikaler und geneigter Belastung.
			17,90 €
Nr. 58	Russelli, C.	(2008)	Probabilistic Methods applied to the Bearing Capacity Problem.
			17,90 €
Nr. 59	Peña Olarte, A. A.	(2008)	Influence of Particle Shape on the Global Mechanical Response of Granular Packings: Micromechanical Investigation of the Critical State in Soil Mechanics.
			17,90 €